Reduced and multiscale models for the human cardiovascular system

L. Formaggia[1] and A. Veneziani[2]
MOX, Mathematics Department ”F. Brioschi”
Politecnico di Milano
Piazza L. da Vinci 32, I-20133 MILAN, Italy

13th May 2003

---

[1] luca.formaggia@mate.polimi.it
[2] ales@mate.polimi.it

Abstract

This report collects the notes of two lectures given by L. Formaggia at the 7^{th} VKI Lecture Series on "Biological fluid dynamics" held at the *Von Karman Institute*, Belgium, on May 2003.

They give a summary of some aspects of the research activity carried out by the authors at Politecnico di Milano and at EPFL, Lausanne, under the direction of Prof. A. Quarteroni, aimed at providing mathematical models and numerical techniques for the simulation of the human cardiovascular system.

Therefore, the authors wish to acknowledge all the people that, at various and different level, have collaborated to the results described in the report. In alphabetical order, Jean-Frederic Gerbeau, Ciak-Liu Goh, Daniele Lamponi, Fabio Nobile, Alfio Quarteroni, Stefania Ragni, Simon Tweddle. They also acknowledge the collaboration with G. Dubini and F. Migliavacca of LABS, Structural Engineering Dep., Politecnico di Milano, with respect to the assessment of multiscale models on realistic geometries and S. Sherwin and J. Peiro of Imperial College London, with respect to the assessment of the one-dimensional model for blood flow in arteries.

This research would not have been possible without the support of various sponsoring agencies. In particular, the European Union, (through to the RTN Project "HaeMOdel"), the Consiglio Nazionale delle Ricerche, (through "Agenzia 2000"), the "Ministero Università e Ricerca Scientifica e Tecnologica", the "Politecnico di Milano" and the "Fond National Suisse".

This report is subdivided into two chapters, in correspondence with the two lectures. The first deals with the derivation of one dimensional models for blood flow in arteries. The second is more specifically devoted to the description and analysis of the "geometrical multiscale" technique.

Contents

Chapter 1

One dimensional models for blood flow in the human vascular system

1.1 Introduction

The numerous works which have appeared in recent years, for example [3, 16, 28, 30] and the references therein, testify a growing interest in the mathematical and numerical modelling of the human cardiovascular system. Within this context, a large research activity is currently devoted to complex threee dimensional simulations able to provide sufficient details of the flow field to extract local data such as wall shear stresses. However those computations are still quite expensive in terms of human resources needed to extract the goemetry and prepare the computational model and computing time.

Yet, bioengineers and medical researchers often do not need to know the flow in such detail and the application of simplified models have demonstrated to be able to provide useful information at a reasonable computational cost.

In this lecture the attention is focussed on one-dimensional models for blood flow in arteries. In these models the arterial circulation is considered as a network of compiant vessels, each described by a one dimensional system of two partial differential equations able to provide average values of velocity and pressure on each vessel axial section.

The presence of the rest of the circulatory system (capillary bed, heart, venous circulation etc.) may be accounted for by prescribing appropriate boundary conditions at the terminal vessels, often in terms of velocity or pressure history. A more sophisticated (and effective) approach is the coupling with lumped parameter models (which may vary in complexity from simple algebraic relations to system of ordinary differential equations [28, 34]) that describe the parts of the circulatory system not directly resolved by the one dimensional network. This technique may allow to quantify the 'feedback' effects coming from the rest of the circulatory system, much in the spirit of the "geometric multiscale" approach [11, 28] which is the subject of the second Lecture by the same authors.

A one dimensional model may be useful, for instance, to study the effect of local narrowing or stiffening of an artery on the flow and wave propagation patterns. Such a situation can occur due to a stent implantation or in the presence of a vascular prosthesis. Stents are expandable metallic wireframes that are expanded and permanently places inside stenosed arteries in order to recover the original lumen section.

Indeed, atherosclerosis is a very common pathology that cause a restriction of the arterial lumen called a stenosis, which may hinder, or even stop, the flow of blood. Stent implantation technique is much less invasive that a surgical operation, like a by-pass, and may be conducted under local anesthesia. It is then becoming a very common practice.

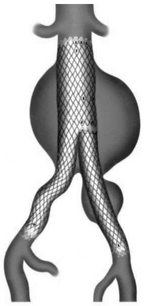

Figure 1.1: A endo-prosthesis used to exclude an aortic aneurism.

Nevertheless, besides other effects, the presence of a stent causes an abrupt variation in the elastic properties of the vessel wall, since the stent is usually far more rigid than the soft arterial tissue. This may cause wave reflections with a consequent alteration in the blood flow pattern [10, 5].

Indeed, the propagation of waves (the *pulse*) is a phenomenon generated by the interaction between the blood flow and the compliant vessel wall and is intrinsically related to the elastic properties of the arteries. The alteration in the pressure pattern is even more significant in the case of vascular prosthesis in the large arteries. For instance when an endo-prosthesis is used to treat aortic or femoral aneurisms. The superposition of the waves reflected by the prosthesis or the stent with those produced by the heart can generate anomalous pressure peaks.

In the simplest (and most used!) one dimensional models the vessel mechanics is overly simplified. In practice, it is reduced to an algebraic relationship between the mean axial pressure (more precisely the average *intra-mural pressure*) and the area of the lumen. However, one may account also for other mechanical properties such viscoelasticity or longitudinal pre-stress, as well as wall inertia. In the latter case, the relation between pressure and vessel area is governed by a differential equation. Yet, it is still possible, at a price of some simplifications, to recover again a system of two partial differential equations [11, 9]. By doing so, it may be easily recognised that the wall inertia introduces an additional dispersive term, while viscoelasticity contributes with a diffusive operator. The treatment of these additional terms is problematic due to the difficulties in imposing proper boundary conditions. However, for physiological situations inertia and viscoelastic effects are not very important.

The layout of this lecture note is as follows. In Sect. 1.2 we derive the basic 1D nonlinear hyperbolic model for a single cylindrical straight arterial element. We will also recall the main hypothesis and simplifications. In Sect. 1.3 we introduce the Taylor-Galerkin scheme that we use for the numerical approximation, and analyse how to impose the conditions (boundary and compatibility conditions) that need to be provided at the proximal and distal boundaries. We also give some example of numerical results.

In section 1.4 we present a domain decomposition strategy that might be applied to the case of abrupt variations for mechanical characteristics as well as to model arterial branching. Interface conditions, which satisfy an energy inequality, are proposed and the problem of bifurcation with specific angles is treated. The proposed interface conditions are fully non-linear and guarantee the stability of the coupled problem. We will present some numerical results and in particular a simulation of a network composed by 55 arteries.

Finally, in section 1.5 we present some numerical results for more complex vessel law by adding inertia, viscoelastic, longitudinal pre-stress terms to the basic algebraic law. We give a numerical framework where these additional terms are treated by an operator splitting approach.

1.2 Derivation of the basic model

Here we introduce the simplest non-linear 1D model for blood flow in compliant vessels. As an historical note we mention that this model was originally found by Euler in 1775. Indeed, the resulting system of two partial differential equation closely resemble the well known Euler equation of compressible gas-dynamics. Indeed, it seems that Euler first came across this type of hyperbolic systems when trying to model blood flow. However, he did not find a way to solve the equations, which were tackled many years later,

The model describes the flow motion in arteries and its interaction with the wall displacement. The basic equations are derived for a tract of artery free of bifurcations, which is idealised as a cylindrical compliant tube. In this work we will denote by $I = (t_0, t_1)$ the time interval of interest and for the sake of convenience we will take $t_0 = 0$. By Ω_t we indicate the spatial domain which is supposed to be a circular cylinder filled with blood, which is changing with time under the action of the pulsatile fluid.

We will mainly use Cartesian coordinates, yet when dealing with cylindrical geometries it is handy to introduce a cylindrical coordinate system. Therefore, in the following we indicate with $\mathbf{e}_r$, $\mathbf{e}_\theta$ and $\mathbf{e}_z$ the radial, circumferential and axial unit vectors, respectively, (r, θ, z) being the corresponding coordinates. We assume that the vessel extends from $z = 0$ to $z = L$ and the vessel length L is constant with time.

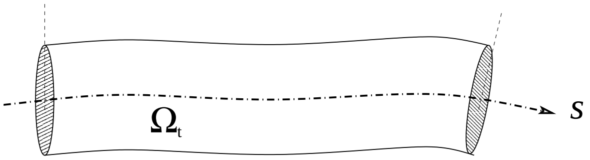

Figure 1.2: The domain Ω_t representing the portion of an artery.

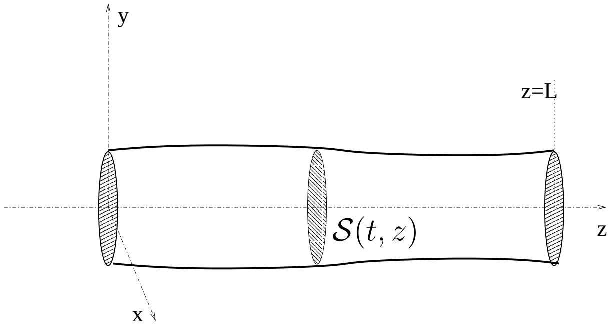

Figure 1.3: Simplified geometry. The vessel is assumed to by a straight cylinder with circular cross section.

The basic model is deduced by making the following simplifying assumptions.

A.1. *Axial symmetry*. All quantities are independent from the angular coordinate θ. As a consequence, every axial section $z =$const remains circular during the wall motion. The tube radius R is a function of z and t.

A.2. *Radial displacements*. The wall displaces along the radial direction solely, thus at each point on the tube surface we may write $\boldsymbol{\eta} = \eta \mathbf{e}_r$, where $\eta = R - R_0$ is the displacement with respect to the reference radius R_0. This hypothesis may be dispensed with, yet the greater complexity of the structural model that has to be used in this case is barely justified since in practice axial displacements are very small.

A.3. *Fixed cylinder axis*. This simply means that the vessel will expand and contract around its axis, which is fixed in time. This hypothesis is indeed consistent with that of axial symmetry. However, it precludes the possibility of accounting for the effects of displacements of the artery axis such the ones that occur in the coronaries because of the heart movement.

A.4. *Constant pressure on each axial section*. We assume that the pressure P is constant on each section, so that it depends only on z and t.

A.5. *No body forces*. We neglect body forces. However, the inclusion of the gravity force is straightforward (it just add a term of the from gh to the pressure). A slightly more complicated (yet still feasible) addition would be the one that describes the change of gravity forces occurring when a person is rising from an horizontal position.

A.6. *Dominance of axial velocity*. The velocity components orthogonal to the z axis are negligible compared to the component along z. The latter is indicated by u_z and its expression in cylindrical coordinates is supposed to be of the form

$$u_z(t,r,z) = \overline{u}(t,z) s\left(rR^{-1}(z)\right) \tag{1.1}$$

where $\overline{u}$ is the *mean velocity* on each axial section and $s : \mathbb{R} \to \mathbb{R}$ is a *velocity profile*. The fact that the velocity profile does not vary in time and space is in contrast with experimental observations and numerical results carried out with full scale models. However, it is a necessary assumption for the derivation of the reduced model. One may then think s as being a profile representative of an average flow configuration.

A generic axial section will be indicated by $\mathcal{S} = \mathcal{S}(t,z)$. Its measure A is given by

$$A(t,z) = \int_{\mathcal{S}(t,z)} d\sigma = \pi R^2(t,z) = \pi(R_0(z) + \eta(t,z))^2. \tag{1.2}$$

The mean velocity $\overline{u}$ is then given by

$$\overline{u} = A^{-1} \int_{\mathcal{S}} u_z d\sigma,$$

and from (1.1) it follows easily that s must be such that

$$\int_0^1 s(y) y dy = \frac{1}{2}$$

We will indicate with α the *momentum-flux correction coefficient*, (sometimes also called Coriolis coefficient) defined as

$$\alpha = \frac{\int_{\mathcal{S}} {u_z}^2 d\sigma}{A\overline{u}^2} = \frac{\int_{\mathcal{S}} s^2 d\sigma}{A}, \tag{1.3}$$

where the dependence of the various quantities on the spatial and time coordinates is understood. It is immediate to verify that $\alpha \geq 1$. In general this coefficient will vary in time and space, yet in our model it is taken constant as a consequence of (1.1).

A possible choice for the profile law is the parabolic profile $s(y) = 2(1 - y^2)$ that corresponds to the well known Poiseuille solution characteristic of steady flows in circular tubes. In this case we have $\alpha = \frac{4}{3}$. However, for blood flow in arteries it has been found that the velocity profile is, on average, rather flat. Indeed, a profile law often used for blood flow in arteries (see for instance [31]) is a power law of the type $s(y) = \gamma^{-1}(\gamma + 2)(1 - y^\gamma)$ with typically $\gamma = 9$ (the value $\gamma = 2$ gives again the parabolic profile). Correspondingly, we have $\alpha = \frac{\gamma+2}{\gamma+1} = 1.1$. Furthermore, we will see that the choice $\alpha = 1$, which indicates a completely flat velocity profile, simplifies the analysis.

The mean flux Q, defined as

$$Q = \int_{\mathcal{S}} u_z d\sigma = A\overline{u},$$

is one of the main variables of our problem, together with A and the pressure P.

There are (at least) three ways of deriving our model. The first one moves from the incompressible Navier-Stokes equations and performs an asymptotic analysis by assuming that the ratio $\frac{R_0}{L}$ is small, thus discarding the higher order terms with respect to $\frac{R_0}{L}$ [2]. The second approach derives the model directly from the basic conservation laws written in integral form. The third approach consists of integrating the Navier-Stokes equations on a generic section $\mathcal{S}$. We will follow the latter and we will indicate with Γ_t^w the wall boundary of Ω_t, which now reads

$$\Gamma_t^w = \{(r, \theta, z) : \, r = R(z, t), \, \theta \in [0, 2\pi) \, z \in (0, L)\}$$

while $\mathbf{n}$ is the outwardly oriented normal to $\partial\Omega_t$. Under the previous assumptions, the momentum along z and continuity equations, in the hypothesis of constant viscosity, are

$$\frac{\partial u_z}{\partial t} + \operatorname{div}(u_z \mathbf{u}) + \frac{1}{\rho}\frac{\partial P}{\partial z} - \nu \Delta u_z = 0, \tag{1.4a}$$

$$\operatorname{div} \mathbf{u} = 0, \tag{1.4b}$$

and on the tube wall we have the following kinematic condition

$$\mathbf{u} = \dot{\boldsymbol{\eta}}, \quad \text{on } \Gamma_t^w,$$

where $\dot{\boldsymbol{\eta}} = \frac{\partial \boldsymbol{\eta}}{\partial t} = \frac{\partial \eta}{\partial t}\mathbf{e}_r$ is the vessel wall velocity.

The convective term in the momentum equation has been taken in divergence form because it simplifies the further derivation.

To ease notation, in this section we will omit to explicitly indicate the time dependence, with the understanding that all variables are considered at time t. Let us consider the portion $\mathcal{P}$ of Ω_t, sketched in Fig. 1.4, comprised between $z = z^* - \frac{dz}{2}$ and $z = z^* + \frac{dz}{2}$, with $z^* \in (0, L)$ and $dz > 0$ small enough so that $z^* + \frac{dz}{2} < L$ and $z^* - \frac{dz}{2} > 0$. The part of $\partial\mathcal{P}$ laying on the tube wall is indicated by $\Gamma^w_{\mathcal{P}}$. The reduced model is derived by integrating (1.4b) and (1.4a) on $\mathcal{P}$ and passing to the limit as $dz \to 0$, assuming that all quantities are smooth enough

We will first report a useful result whose proof may be found, for instance, in [24].

Let $f : \Omega_t \times I \to \mathbb{R}$ *be an axisymmetric function, i.e.* $\dfrac{\partial f}{\partial \theta} = 0$. *Let us indicate by* f_w *the value of* f *on the wall boundary and by* $\overline{f}$ *its mean value on each axial section, defined by*

$$\overline{f} = A^{-1} \int_{\mathcal{S}} f d\sigma.$$

We have the following relation $\frac{\partial}{\partial t}(A\overline{f}) = A\overline{\frac{\partial f}{\partial t}} + 2\pi R \dot{\eta} f_w$.

In particular taking $f = 1$ *we recover that*

$$\frac{\partial A}{\partial t} = 2\pi R \dot{\eta}. \tag{1.5}$$

We are now ready to derive our reduced model. We start first from the continuity equation. Using the divergence theorem, we obtain

$$0 = \int_{\mathcal{P}} \operatorname{div} \mathbf{u} = -\int_{\mathcal{S}^-} u_z + \int_{\mathcal{S}^+} u_z + \int_{\Gamma^w_{\mathcal{P}}} \mathbf{u} \cdot \mathbf{n} = -\int_{\mathcal{S}^-} u_z + \int_{\mathcal{S}^+} u_z + \int_{\Gamma^w_{\mathcal{P}}} \dot{\boldsymbol{\eta}} \cdot \mathbf{n}. \tag{1.6}$$

We have exploited the fact that $\mathbf{n} = -\mathbf{e}_z$ on $\mathcal{S}^-$ while $\mathbf{n} = \mathbf{e}_z$ on $\mathcal{S}^+$. Now, since $\dot{\boldsymbol{\eta}} = \dot{\eta}\mathbf{e}_r$, we deduce

$$\int_{\Gamma^w_{\mathcal{P}}} \dot{\boldsymbol{\eta}} \cdot \mathbf{n} = [2\dot{\eta}\pi R(\overline{z})dz + o(dz)] = \text{ (by (1.5)) } = \frac{\partial}{\partial t} A(\overline{z})dz + o(dz).$$

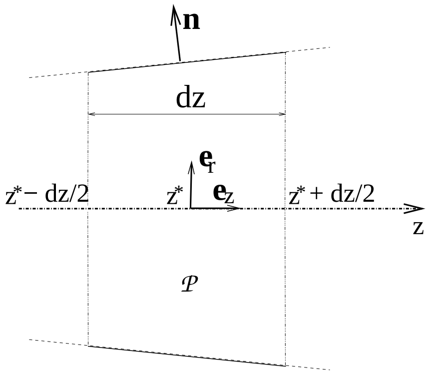

Figure 1.4: A longitudinal section (θ =const.) of the tube and the portion between $z = z^* - \frac{dz}{2}$ and $z = z^* + \frac{dz}{2}$ used for the derivation of the 1D reduced model.

By substituting into (1.6), using the definition of Q, and passing to the limit as $dz \to 0$, we finally obtain

$$\frac{\partial A}{\partial t} + \frac{\partial Q}{\partial z} = 0,$$

which is the *reduced form of the continuity equation.*

We will now consider all terms in the momentum equation in turn. Again, we will integrate them over $\mathcal{P}$ and consider the limit as dz tends to zero.

$$\int_{\mathcal{P}} \frac{\partial u_z}{\partial t} = \frac{d}{dt}\int_{\mathcal{P}} u_z - \int_{\partial\mathcal{P}} u_z \mathbf{g}\cdot\mathbf{n} = \frac{d}{dt}\int_{\mathcal{P}} u_z.$$

In order to eliminate the boundary integral we have exploited the fact that $u_z = 0$ on $\Gamma^w_{\mathcal{P}}$ and $\mathbf{g} = \mathbf{0}$ on $\mathcal{S}^-$ and $\mathcal{S}^+$. We may then write

$$\int_{\mathcal{P}} \frac{\partial u_z}{\partial t} = \frac{\partial}{\partial t}[A(\overline{z})\overline{u}(\overline{z})dz + o(dz)] = \frac{\partial Q}{\partial t}(\overline{z})dz + o(dz).$$

Moreover, we have

$$\int_{\mathcal{P}} \mathrm{div}(u_z\mathbf{u}) = \int_{\partial\mathcal{P}} u_z\mathbf{u}\cdot\mathbf{n} = -\int_{\mathcal{S}^-} {u_z}^2 + \int_{\mathcal{S}^+} {u_z}^2 + \int_{\Gamma^w_{\mathcal{P}}} u_z\mathbf{g}\cdot\mathbf{n} =$$
$$\alpha[A(\overline{z}+\frac{dz}{2})\overline{u}^2(\overline{z}+\frac{dz}{2}) - A(\overline{z}-\frac{dz}{2})\overline{u}^2(\overline{z}-\frac{dz}{2})] = \frac{\partial \alpha A\overline{u}^2}{\partial z}(\overline{z})dz + o(dz).$$

Again, we have exploited the condition $u_z = 0$ on $\Gamma^w_{\mathcal{P}}$.

Since the pressure is assumed to be constant on each section, we obtain

$$\int_{\mathcal{P}} \frac{\partial P}{\partial z} = -\int_{\mathcal{S}^-} P + \int_{\mathcal{S}^+} P + \int_{\Gamma^w_{\mathcal{P}}} Pn_z =$$
$$A(\overline{z}+\frac{dz}{2})P(\overline{z}+\frac{dz}{2}) - A(\overline{z}-\frac{dz}{2})P(\overline{z}-\frac{dz}{2}) + \int_{\Gamma^w_{\mathcal{P}}} Pn_z \quad (1.7)$$

Since $\int_{\partial\mathcal{P}} n_z = 0$, we may write that

$$\int_{\Gamma^w_{\mathcal{P}}} Pn_z = P(\overline{z})\int_{\Gamma^w_{\mathcal{P}}} n_z + o(dz) = -P(\overline{z})\int_{\partial\mathcal{P}\setminus\Gamma^w_{\mathcal{P}}} n_z + o(dz) =$$
$$-P(\overline{z})(A(\overline{z}+\frac{dz}{2}) - A(\overline{z}-\frac{dz}{2})) + o(dz)$$

By substituting the last result into (1.7) we have

$$\int_{\mathcal{P}} \frac{\partial P}{\partial z} = A(\overline{z}+\frac{dz}{2})P(\overline{z}+\frac{dz}{2}) - A(\overline{z}-\frac{dz}{2})P(\overline{z}-\frac{dz}{2}) -$$
$$P(\overline{z})[A(\overline{z}+\frac{dz}{2}) - A(\overline{z}-\frac{dz}{2})] + o(dz)$$
$$= \frac{\partial(AP)}{\partial z}(\overline{z})dz - P(\overline{z})\frac{\partial A}{\partial z}(\overline{z})dz + o(dz) = A\frac{\partial P}{\partial z}(\overline{z})dz + o(dz).$$

We finally consider the viscous term,

$$\int_{\mathcal{P}} \Delta u_z = \int_{\partial\mathcal{P}} \boldsymbol{\nabla} u_z \cdot \mathbf{n} = -\int_{\mathcal{S}^-} \frac{\partial u_z}{\partial z} + \int_{\mathcal{S}^+} \frac{\partial u_z}{\partial z} + \int_{\Gamma^w_{\mathcal{P}}} \boldsymbol{\nabla} u_z \cdot \mathbf{n}.$$

We neglect $\frac{\partial u_z}{\partial z}$ by assuming that its variation along z is small compared to the other terms. Moreover, we split $\mathbf{n}$ into two vector components, the radial component $\mathbf{n}_r = n_r\mathbf{e}_r$ and $\mathbf{n}_z = \mathbf{n} - \mathbf{n}_r$. Owing to the cylindrical geometry, $\mathbf{n}$ has no component along the circumpherential coordinate and, consequently, $\mathbf{n}_z$ is indeed oriented along z. We may thus write

$$\int_{\mathcal{P}} \Delta u_z = \int_{\Gamma^w_{\mathcal{P}}} (\boldsymbol{\nabla} u_z \cdot \mathbf{n}_z + \boldsymbol{\nabla} u_z \cdot \mathbf{e}_r n_r)\, d\sigma.$$

Again, we neglect the term $\boldsymbol{\nabla} u_z \cdot \mathbf{n}_z$, which is proportional to $\frac{\partial u_z}{\partial z}$. We recall relation (1.1) to write

$$\int_{\mathcal{P}} \Delta u_z = \int_{\Gamma^w_{\mathcal{P}}} n_r \boldsymbol{\nabla} u_z \cdot \mathbf{e}_r d\sigma = \int_{\Gamma^w_{\mathcal{P}}} \overline{u} R^{-1} s'(1)\mathbf{n} \cdot \mathbf{e}_r d\sigma = 2\pi \int_{\overline{z}-\frac{dz}{2}}^{\overline{z}+\frac{dz}{2}} \overline{u} s'(1) dz,$$

where we have used the relation $n_r d\sigma = 2\pi R dz$ and indicated by s' the first derivative of s.

Then, $\int_{\mathcal{P}} \Delta u_z \approx 2\pi \overline{u}(\overline{z}) s'(1) dz$.

By substituting all results into (1.4a), dividing all terms by dz and passing to the limit as $dz \to 0$, we may finally write the momentum equation of our one dimensional model as follows

$$\frac{\partial Q}{\partial t} + \frac{\partial(\alpha A \overline{u}^2)}{\partial z} + \frac{A}{\rho}\frac{\partial P}{\partial z} + K_r \overline{u} = 0,$$

where

$$K_r = -2\pi\nu s'(1)$$

is a *friction parameter*, which depends on the type of profile chosen, i.e. on the choice of the function s in (1.1). For a profile law given by $s(y) = \gamma^{-1}(\gamma+2)(1-y^\gamma)$ we have $K_r = 2\pi\nu(\gamma+2)$. In particular, for a parabolic profile we have $K_r = 8\pi\nu$ (which is the value generally used in practice). For $\gamma = 9$ we obtain instead $K_r = 22\pi\nu$.

To conclude, the final system of equations reads, foe $z \in (0, L)$ and $t \in I$

$$\frac{\partial A}{\partial t} + \frac{\partial Q}{\partial z} = 0, \tag{1.8a}$$

$$\frac{\partial Q}{\partial t} + \alpha \frac{\partial}{\partial z}\left(\frac{Q^2}{A}\right) + \frac{A}{\rho}\frac{\partial P}{\partial z} + K_r\left(\frac{Q}{A}\right) = 0, \tag{1.8b}$$

where the unknowns are A, Q and P and α is here taken constant.

Remark 1.1. *For the case $\alpha = 1$, it is possible to rewrite the system it terms of the variables $(A, \overline{u})$, by simple algebraic manipulation the momentum equation becomes*

$$\frac{\partial \overline{u}}{\partial t} + \frac{\partial}{\partial z}\left(\frac{P}{\rho} + \frac{1}{2}\overline{u}^2\right) + K_r \overline{u} = 0,$$

the continuity equation being unaltered. This change of variables is allowable only whenever the solution is smooth. In general, the (A, Q) system is more fundamental since it stems directly from the basic conservation principles.

1.2.1 Accounting for the vessel wall displacement

In order to close system (1.8) we have to provide a relation for the pressure. A complete mechanical model for the structure of the vessel wall would provide a differential equation which links the displacement and its spatial and temporal derivatives to the force applied by the fluid. We will consider equation of this kind in a later section. Here we will adopt instead an hypothesis quit commonly used in practice. Namely, that the inertial terms are neglegible and that the elastic stresses in the circumferential direction are dominant. Under this assumption, the wall mechanics reduces to an algebraic relation linking pressure to the wall deformation and consequently to the vessel section A. More precisely, the relation should involve the whole normal component of the wall stress, yet since we have neglected the viscous contribution, the only normal stress acting on the wall is that due to the pressure.

In a most general setting, we may assume that the pressure satisfies a relation like

$$P(t,z) - P_{ext} = \psi(A(t,z); A_0(z), \boldsymbol{\beta}(z)), \tag{1.9}$$

where we have outlined that the pressure will in general depend also on $A_0 = \pi R_0^2$ and on a set of coefficients $\boldsymbol{\beta} = (\beta_0, \beta_1, \cdots, \beta_p)$, related to physical and mechanical properties, that are, in general, *given* functions of z. Here P_{ext} indicates the external pressure exherted by the organs outside the vessel (often taken equal to 0). We require that ψ be (at least) a C^1 function of all its arguments and be defined for all $A > 0$ and $A_0 > 0$, while the range of variation of $\boldsymbol{\beta}$ will depend by the particular mechanical model chosen for the vessel wall.

Furthermore, we require that for all allowable values of A, A_0 and $\boldsymbol{\beta}$

$$\frac{\partial \psi}{\partial A} > 0, \quad \text{and} \quad \psi(A_0; A_0, \boldsymbol{\beta}) = 0. \tag{1.10}$$

By exploiting the well known linear elastic law for a cylindrical vessel and using the fact that

$$\eta = (\sqrt{A} - \sqrt{A_0})/\sqrt{\pi} \tag{1.11}$$

we can obtain the following expression for ψ

$$\psi(A; A_0, \beta_0) = \beta_0 \frac{\sqrt{A} - \sqrt{A_0}}{A_0}. \tag{1.12}$$

We have identified $\boldsymbol{\beta}$ with the single parameter $\beta_0 = \frac{\sqrt{\pi} h_0 E}{1-\xi^2}$. The latter depends on z only in those cases where the Young modulus E or the vessels thickness h_0 are not constant.

It is immediate to verify that all the requirements in (1.10) are indeed satisfied.

Another commonly used expression for the pressure-area relationship is given by [14, 31]

$$\psi(A; A_0, \boldsymbol{\beta}) = \beta_0 \left[\left(\frac{A}{A_0} \right)^{\beta_1} - 1 \right].$$

In this case, $\boldsymbol{\beta} = (\beta_0, \beta_1)$, where $\beta_0 > 0$ is an elastic coefficient while $\beta_1 > 0$ is normally obtained by fitting the stress-strain response curves obtained by experiments.

Another alternative formulation [17] is

$$\psi(A; A_0, \boldsymbol{\beta}) = \beta_0 \tan \left[\pi \left(\frac{A - A_0}{2A_0} \right) \right],$$

where again the coefficients vector $\boldsymbol{\beta}$ reduces to a single coefficient β_0.

In the following, whenever not strictly necessary we will omit to indicate the dependence of the various quantities on A_0 and $\boldsymbol{\beta}$, which is however always understood.

1.2.2 The final model

By exploiting relation (1.9) we may eliminate the pressure P from the momentum equation. To that purpose we will indicate by $c_1 = c_1(A; A_0, \boldsymbol{\beta})$ the following quantity

$$c_1 = \sqrt{\frac{A}{\rho}\frac{\partial \psi}{\partial A}}, \tag{1.13}$$

which has the dimension of a velocity and, as we will see later on, is related to the speed of propagation of simple waves along the tube.

By simple manipulations (1.8) may be written in *quasi-linear* form as follows

$$\frac{\partial}{\partial t}\mathbf{U} + \mathbf{H}(\mathbf{U})\frac{\partial \mathbf{U}}{\partial z} + \mathbf{S}(\mathbf{U}) = \mathbf{0}, \tag{1.14}$$

where,

$$\mathbf{U} = \begin{bmatrix} A \\ Q \end{bmatrix},$$

$$\mathbf{H}(\mathbf{U}) = \begin{bmatrix} 0 & 1 \\ \dfrac{A}{\rho}\dfrac{\partial \psi}{\partial A} - \alpha \overline{u}^2 & 2\alpha\overline{u} \end{bmatrix} = \begin{bmatrix} 0 & 1 \\ c_1^2 - \alpha\left(\dfrac{Q}{A}\right)^2 & 2\alpha\dfrac{Q}{A} \end{bmatrix}, \tag{1.15}$$

and

$$\mathbf{S}(\mathbf{U}) = \begin{bmatrix} 0 \\ K_R\left(\dfrac{Q}{A}\right) + \dfrac{A}{\rho}\dfrac{\partial \psi}{\partial A_0}\dfrac{dA_0}{dz} + \dfrac{A}{\rho}\dfrac{\partial \psi}{\partial \boldsymbol{\beta}}\dfrac{d\boldsymbol{\beta}}{dz} \end{bmatrix}.$$

Clearly, if A_0 and $\boldsymbol{\beta}$ are constant the expression for $\mathbf{S}$ becomes simpler. A *conservation form* for (1.14) may be found as well and reads

$$\frac{\partial \mathbf{U}}{\partial t} + \frac{\partial}{\partial z}[\mathbf{F}(\mathbf{U})] + \mathbf{B}(\mathbf{U}) = \mathbf{0}, \tag{1.16}$$

where

$$\mathbf{F}(\mathbf{U}) = \begin{bmatrix} Q \\ \alpha\frac{Q^2}{A} + C_1 \end{bmatrix}$$

is the vector of fluxes,

$$\mathbf{B}(\mathbf{U}) = \mathbf{S}(\mathbf{U}) - \begin{bmatrix} 0 \\ \dfrac{\partial C_1}{\partial A_0}\dfrac{dA_0}{dz} + \dfrac{\partial C_1}{\partial \boldsymbol{\beta}}\dfrac{d\boldsymbol{\beta}}{dz}, \end{bmatrix}$$

and C_1 is a primitive of c_1^2 with respect to A, given by

$$C_1(A; A_0, \boldsymbol{\beta}) = \int_{A_0}^{A} c_1^2(\tau; A_0, \boldsymbol{\beta})\, d\tau.$$

Again, if A_0 and $\boldsymbol{\beta}$ are constant, the source term $\mathbf{B}$ simplifies and becomes $\mathbf{B} = \mathbf{S}$. System (1.16) allows to identify the vector $\mathbf{U}$ as the the *conservation variables* of our problem.

Remark 1.2. *In the case we use relation (1.12) we have*

$$c_1 = \sqrt{\frac{\beta_0}{2\rho A_0}} A^{\frac{1}{4}}, \quad C_1 = \frac{\beta_0}{3\rho A_0} A^{\frac{3}{2}}. \tag{1.17}$$

If $A \geq 0$, the matrix $\mathbf{H}$ possesses two real eigenvalues. Furthermore, if $A > 0$ the two eigenvalues are distinct and (1.14) is a strictly hyperbolic *system of partial differential equations.*

Proof. By performing standard algebraic computations we obtain the following expression for the eigenvalues of $\mathbf{H}$,

$$\lambda_{1,2} = \alpha \overline{u} \pm c_\alpha, \tag{1.18}$$

where

$$c_\alpha = \sqrt{c_1^2 + \overline{u}^2 \alpha\, (\alpha - 1)}.$$

Since $\alpha \geq 1$, c_α is a real number. If $c_\alpha > 0$ the two eigenvalues are distinct. A sufficient condition to have $c_\alpha > 0$ is $c_1 > 0$ and, thanks to the definition of c_1 and (1.10), this is always true if $A > 0$. If $\alpha = 1$, this condition is also necessary.

The existence of a complete set of (right and left) eigenvectors is an immediate consequence of $\mathbf{H}$ having distinct eigenvalues. ☐

Remark 1.3. *As remarked in the Introduction, system (1.8) shares many analogies with the 1D compressible Euler equations after identifying the section area A with the density. The equivalence is not complete as the term $\frac{\partial P}{\partial z}$ in the Euler equations is here replaced by $A\frac{\partial P}{\partial z}$.*

Characteristics analysis

Let ($\mathbf{l}_1$, $\mathbf{l}_2$) and ($\mathbf{r}_1$, $\mathbf{r}_2$) be two couples of left and right eigenvectors of the matrix $\mathbf{H}$ in (1.15), respectively. The matrices $\mathbf{L}$, $\mathbf{R}$ and $\boldsymbol{\Lambda}$ are defined as

$$\mathbf{L} = \begin{bmatrix} \mathbf{l}_1^T \\ \mathbf{l}_2^T \end{bmatrix}, \qquad \mathbf{R} = \begin{bmatrix} \mathbf{r}_1 & \mathbf{r}_2 \end{bmatrix}, \qquad \boldsymbol{\Lambda} = \mathrm{diag}(\lambda_1, \lambda_2) = \begin{bmatrix} \lambda_1 & 0 \\ 0 & \lambda_2 \end{bmatrix}. \tag{1.19}$$

Since right and left eigenvectors are mutually orthogonal, without loss of generality we choose them so that $\mathbf{LR} = \mathbf{I}$. Matrix $\mathbf{H}$ may then be decomposed as

$$\mathbf{H} = \mathbf{R}\boldsymbol{\Lambda}\mathbf{L}, \tag{1.20}$$

and system (1.14) written in the equivalent form

$$\mathbf{L}\frac{\partial \mathbf{U}}{\partial t} + \mathbf{\Lambda}\mathbf{L}\frac{\partial \mathbf{U}}{\partial z} + \mathbf{L}\mathbf{S}(\mathbf{U}) = \mathbf{0}, \quad z \in (0, L),\, t \in I. \tag{1.21}$$

If there exist two quantities W_1 and W_2 which satisfy

$$\frac{\partial W_1}{\partial U} = \mathbf{l}_1, \quad \frac{\partial W_2}{\partial U} = \mathbf{l}_2, \tag{1.22}$$

we will call them *characteristic variables* of our hyperbolic system. We point out that in the case where the coefficients A_0 and $\boldsymbol{\beta}$ are not constant, $\mathbf{W}_1$ and $\mathbf{W}_2$ are not autonomous functions of $\mathbf{U}$.

By setting $\mathbf{W} = [W_1, W_2]^T$ system (1.21) may be elaborated into

$$\frac{\partial \mathbf{W}}{\partial t} + \mathbf{\Lambda}\frac{\partial \mathbf{W}}{\partial z} + \mathbf{G} = \mathbf{0}, \tag{1.23}$$

where

$$\mathbf{G} = \mathbf{L}\mathbf{S} - \frac{\partial W}{\partial A_0}\frac{dA_0}{dz} - \frac{\partial W}{\partial \boldsymbol{\beta}}\frac{d\boldsymbol{\beta}}{dz}. \tag{1.24}$$

Componentwise

$$\frac{\partial W_i}{\partial t} + \lambda_i\frac{\partial W_i}{\partial z} + G_i = 0,\, i = 1, 2 \tag{1.25}$$

Note that in general G_i will depend on W_1 and W_2 through the dependence of $\mathbf{S}$ on $\mathbf{U}$.

These expressions are quite general, in the case where $\mathbf{S} = \mathbf{0}$ and the coefficients A_0 and $\boldsymbol{\beta}$ are constant $\mathbf{G} = \mathbf{0}$ and (1.23) takes the simpler form

$$\frac{\partial \mathbf{W}}{\partial t} + \mathbf{\Lambda}\frac{\partial \mathbf{W}}{\partial z} = \mathbf{0}, \tag{1.26}$$

which component-wise reads

$$\frac{\partial W_i}{\partial t} + \lambda_i\frac{\partial W_i}{\partial z} = 0,\, i = 1, 2 \tag{1.27}$$

which is the a non-linear (since λ_i will in general depend on W_1 and W_2) first order wave equation. If we consider the *characteristic line* $y_i(t)$ which satisfies the differential equation

$$\frac{d}{dt}y_i(t) = \lambda_i(t, y_i(t)), \quad i = 1, 2$$

then (1.27) may be rewritten as

$$\frac{d}{dt}W_i(t, y_i(t)) = 0 \quad i = 1, 2 \tag{1.28}$$

which shows that W_i is *constant along the i-th characteristic line*.

In the more general case we will have

$$\frac{d}{dt}W_i(t, y_i(t)) + G_i(W_1, W_2) = 0, \quad i = 1, 2 \tag{1.29}$$

where we have made evident the dependence of G_i on the characteristic variables. Clearly the latter system if slightly more complex, yet it might be approximated numerically by a ODE system solver. Again an approximation of (1.29) might be used to provide boundary compatibility conditions for our numerical scheme. We will postpone the discussinon to Sect. 1.3.

Remark 1.4. *If we linearise the system (i.e. we take the λ_i constant), (1.28) has a general solution of the form*

$$W_i(t, z) = \varphi_i(z - \lambda_i t), \quad i = 1, 2$$

where the φ_i's are functions that have to be consistent with the initial and boundary conditions of the original problem. This relation enlighten the wave-like nature of blood flow in arteries; the general solution is a super-imposition of waves traveling at speed λ_1 and λ_2,

$$\begin{bmatrix} A(t, z) \\ Q(t, z) \end{bmatrix} = \mathbf{L}^{-1} \begin{bmatrix} \varphi_i(z - \lambda_1 t) \\ \varphi_2(z - \lambda_2 t), \end{bmatrix}$$

being in this case **L** *constant. In the non-linear case the interaction is more complex, yet the basic features of the solution are the same.*

The linearised system is the basis of many relationships for pulse wave propagation often found in the bio-engineering and medical literature.

Remark 1.5. *The relations found so far are valid in regions where* the solution is continuous. *Blood flow does not present discontinuities (at least in most situations) so we will not go further into this matter. Indeed it may be shown [6] that, for the typical values of the mechanical and geometric parameters in physiological conditions and the typical vessel lengths in the arterial tree, the solution of our hyperbolic system remains smooth, in accordance to what happens in the actual physical problem (which is however dissipative, a feature which has been neglected in our one-dimensional model).*

Yet, anyone interested in the analysis or the numerical aspect of discontinuous solutions of hyperbolic system may consult, for instance [19] or [13].

The expression for the left eigenvectors $\mathbf{l}_1$ and $\mathbf{l}_2$ is given by

$$\mathbf{l}_1 = \zeta \begin{bmatrix} c_\alpha - \alpha\overline{u} \\ 1 \end{bmatrix}, \qquad \mathbf{l}_2 = \zeta \begin{bmatrix} -c_\alpha - \alpha\overline{u} \\ 1 \end{bmatrix},$$

where $\zeta = \zeta(A, \overline{u})$ is any arbitrary smooth function of its arguments with $\zeta > 0$. Here we have expressed $\mathbf{l}_1$ and $\mathbf{l}_2$ as functions of $(A, \overline{u})$ instead of (A, Q) as is more convenient for the next developments. Thus, relations (1.22) become

$$\frac{\partial W_1}{\partial A} = \zeta \left[c_\alpha - \overline{u}\,(\alpha - 1)\right], \quad \frac{\partial W_1}{\partial \overline{u}} = \zeta A \tag{1.30a}$$

$$\frac{\partial W_2}{\partial A} = \zeta \left[-c_\alpha - \overline{u}\,(\alpha - 1)\right], \quad \frac{\partial W_2}{\partial \overline{u}} = \zeta A. \tag{1.30b}$$

For a hyperbolic system of two equations it is always possible to find the characteristic variables (or, equivalently, the Riemann invariants) locally, that is in a sufficiently small neighbourhood of any point **U** [13, 18], yet the existence of global characteristic variables is not in general guaranteed. However, in the special case $\alpha = 1$, (1.30) takes the much simpler form

$$\frac{\partial W_1}{\partial A} = \zeta c_1, \quad \frac{\partial W_1}{\partial \overline{u}} = \zeta A, \quad \frac{\partial W_2}{\partial A} = -\zeta c_1, \quad \frac{\partial W_2}{\partial \overline{u}} = \zeta A.$$

Let us show that a set of global characteristic variables for our problem does exist in this case. We remind that a classic Calculus result affirms that the condition for the integrability of the differential form, and thus for the existence of the characteristic variable W_1 is that

$$\frac{\partial^2 W_1}{\partial A \partial \overline{u}} = \frac{\partial^2 W_1}{\partial \overline{u} \partial A},$$

for all allowable values of A and $\overline{u}$. Since now c_1 does not depend on $\overline{u}$, the above condition yields

$$c_1 \frac{\partial \zeta}{\partial \overline{u}} = \zeta + A \frac{\partial \zeta}{\partial A}.$$

In order to satisfy this relation, it is sufficient to take $\zeta = \zeta(A)$ such that $\zeta = -A \frac{\partial \zeta}{\partial A}$. A possible instance is $\zeta = A^{-1}$. The resulting differential form is

$$\partial W_1 = \frac{c_1}{A} \partial A + \partial \overline{u},$$

and by proceeding in the same way for W_2 we have $\partial W_2 = -\frac{c_1}{A} \partial A + \partial \overline{u}$.

To integrate it in the $(A, \overline{u})$ plane we need to fix the zero state. i.e. the value of A and Q for which the characteristic variables are zero. Here we take $(A, \overline{u}) = (A_0, 0)$, obtaining

$$W_1 = \overline{u} + \int_{A_0}^{A} \frac{c_1(\tau)}{\tau} d\tau, \qquad W_2 = \overline{u} - \int_{A_0}^{A} \frac{c_1(\tau)}{\tau} d\tau. \tag{1.31}$$

Remark 1.6. If we adopt relation (1.12) *and use the expression for c_1 given in (1.17), after simple computations we have*

$$W_1 = \overline{u} + 4(c_1 - c_{1,0}), \qquad W_2 = \overline{u} - 4(c_1 - c_{1,0}), \tag{1.32}$$

where $c_{1,0}$ is the value of c_1 corresponding to the reference vessel area A_0. We may also write, after a few simple algebraic manipulations

$$W_1 = \overline{u} + \frac{2(P - P_{ext})}{\rho(c_1 + c_{1,0})}, \qquad W_1 = \overline{u} - \frac{2(P - P_{ext})}{\rho(c_1 + c_{1,0})} \tag{1.33}$$

Finally, we might invert the relationship between W and $\mathbf{U}$ to obtain

$$A = \left(\frac{2\rho A_0}{\beta}\right)^2 \left(\frac{W_1 - W_2}{8} + c_{1,0}\right)^4, \qquad Q = A \frac{W_1 + W_2}{2}. \tag{1.34}$$

These expressions may become handy when dealing with boundary or interface conditions, as we will see later on.

Remark 1.7. *The choice of $(A, Q) = (A_0, 0)$ as zero reference state for the calculation of the characteristic variables in (1.31) is somehow arbitrary. It is particularly convenient since it appears natural to associate a zero characteristic variables to the state "at rest". Yet another common choice is to integrate the differential form from $(A, Q) = (0, 0)$. However this is not always possible since the integral in (1.31) may not exist when the integration interval in the A axis includes the zero.*

However, this choice is allowed when adopting the pressure-area relation (1.12). The corresponding expression are obtained by setting $c_{1,0} = 0$ in (1.32), (1.33) and (1.34).

Under physiological conditions, typical values of the flow velocity and mechanical characteristics of the vessel wall are such that $c_\alpha >> \alpha\overline{u}$. Consequently $\lambda_1 > 0$ and $\lambda_2 < 0$, i.e. the flow is sub-critical everywhere. In the light of this consideration, from now on we will always assume sub-critical regime (and smooth solutions).

Remark 1.8. *We also point out that the derivation of the conservative form may be carried out only if β and A_0 are smooth functions of z. In case of abrupt changes of the Young modulus, for instance because of the presence of a prosthesis we either resort to a regularisation of E or to a domain decomposition strategy. We will present the former technique here while the domain decomposition method will be presented in Sect. 1.4.*

Boundary conditions

System (1.8) must be supplemented by proper boundary conditions. The number of conditions to apply at each end equals the number of characteristics entering the domain through that boundary. Since we are only considering sub-critical flows *we have to impose exactly one boundary condition at both $z = 0$ and $z = L$.*

An important class of boundary conditions are the so-called *non-reflecting or 'absorbing'*. They allow the simple wave associated to the outgoing characteristic variable to exit the computational domain with no reflections. Following [33, 15] non-reflecting boundary conditions for one dimensional systems of non-linear hyperbolic equation in conservation form like (1.16) may be written as

$$\mathbf{l}_1 \cdot \left(\frac{\partial \mathbf{U}}{\partial t} + \mathbf{B}(\mathbf{U})\right) = 0 \text{ at } z = 0, \quad \mathbf{l}_2 \cdot \left(\frac{\partial \mathbf{U}}{\partial t} + \mathbf{B}(\mathbf{U})\right) = 0 \text{ at } z = L,$$

for all $t \in I$, which in fact, by defining $R_i = \mathbf{l}_i\mathbf{B}$, may be written in the form

$$\frac{\partial W_1}{\partial t} + R_1(W_1, W_2) = 0 \text{ at } z = 0, \quad \frac{\partial W_2}{\partial t} + R_2(W_1, W_2) = 0 \text{ at } z = L,$$

where we have put into evidence the possible dependence of R_1 and R_2 on W_1 and W_2 through the dependence of $\mathbf{B}$ on $\mathbf{U}$.

Whenever taking $\mathbf{B} = \mathbf{0}$ on the boundary is acceptable, these conditions are equivalent to impose a constant value to the incoming characteristic variable(typically calculated either from the initial value of the problem at hand or from a reference solution). When $S \neq 0$, the R term takes into account the “natural evolution” of the incoming characteristic variable at the boundary due to the presence of the source term. A boundary condition of this type is quite convenient at the outlet (distal) section, particularly whenever we have no better data to impose on that location.

At the inlet (proximal) section instead one usually desires to impose values of pressure or mass flux derived from measurements or other means. Let us suppose, without loss of generality, that $z = 0$ is an inlet section. Whenever an explicit formulation of the characteristic variables is available, the boundary condition may be expressed directly in terms of the entering characteristic variable W_1, i.e., for all $t \in I$

$$W_1(t) = g_1(t) \text{ at } z = 0, \tag{1.35}$$

g_1 being a given function. However, seldom one has directly the boundary datum in terms of the characteristic variable, since is normally given in terms of physical variables.

If one has at disposal the time history $q(t)$ of a just one physical variable $\phi = \phi(A, Q)$ (for instance the pressure) the boundary condition

$$\phi(A(t), Q(t)) = q(t), \quad \forall t \in I, \quad \text{at } z = 0,$$

is admissible under certain restrictions [26], which in our case reduce to exclude the case where ϕ may be expressed as function of only W_2. In particular, it may be found that for the problem at hand the imposition of average pressure, total pressure or mass flux are all admissible.

Sometimes we know the time variation of both pressure and mass flux at the boundary (for instance taken from measurements). We *cannot impose both!*, since this is in contrast with the mathematical characteristic of our differential problem. If we want to account for both boundary data a possible technique is to derive the corresponding value of g_1 using directly the definition of the characteristic variable W_1. If $P_m = P_m(t)$ and $Q_m = Q_m(t)$ are the measured average pressure and mass flux at $z = 0$ for $t \in I$ and $W_1(A, Q)$ indicates the characteristic variable W_1 as function of A and Q, like in (1.31), we may pose

$$g_1(t) = W_1\left(\psi^{-1}(P_m(t) - P_{ext}), Q_m(t)\right), \quad t \in I,$$

in (1.35). This means that P_m and Q_m are not *imposed exactly* at $z = 0$ (this would not be possible since our system accounts for only one boundary condition at each end of the computational domain), yet we require that at all times t the value of A and Q at $z = 0$ lies on the curve in the (A, Q) plane defined by

$$W_1(A, Q) - W_1\left(\psi^{-1}(P_m(t) - P_{ext}), Q_m(t)\right) = 0.$$

Remark 1.9. *If the integration of (1.22) is not feasible (as, for instance, in the case $\alpha \neq 1$), one may resort to the* pseudo-characteristic *variables [26], $\mathbf{Z} = [Z_1,\ Z_2]^T$, defined by linearising (1.22) around an appropriately chosen reference state. One obtains*

$$\mathbf{Z} = \overline{\mathbf{Z}} + \mathbf{L}(\overline{\mathbf{U}})\left(\mathbf{U} - \overline{\mathbf{U}}\right) \tag{1.36}$$

where $\overline{\mathbf{U}}$ is the chosen reference state and $\overline{\mathbf{Z}}$ the corresponding value for $\mathbf{Z}$. One may then use the pseudo-characteristic variables instead of $\mathbf{W}$ and repeat the previous considerations.

In the context of a time advancing scheme for the numerical solution of (1.16) the reference state is usually taken as the solution computed at the previous time step.

1.2.3 More complex wall laws that account for inertia and viscoelasticity

The algebraic relation (1.9) assumes that the wall is instantaneously in equilibrium with the pressure forces acting on it. Indeed, this approach correspond to the so called *independent ring model* for the mechanics of the vessel wall (see for instance [28] or [24]).

More sophisticated models may be introduced by employing a differential law for the vessel structure. We will provide here only the general framework, leaving to the next section more details about the numerical implementation. In the case where a ’shell approximation’ is used for the vessel wall we can consider the following differential law to link the pressure (which is the acting force) to the wall radial displacement η,

$$P - P_{ext} = \gamma_0 \frac{\partial^2 \eta}{\partial t^2} + \gamma_1 \frac{\partial \eta}{\partial t} + \gamma_2 \frac{\partial^2 (A - A_0)}{\partial z^2} + \psi(A; A_0, \boldsymbol{\beta}), \tag{1.37}$$

where $\gamma_0 = \rho_w h_0$, $\gamma_1 = \frac{\gamma}{R_0^2}$ and the last term is the elastic response, modelled is the same way as done before. Here, ρ_w is the density of the tissue which forms the vessel walls, h_0 is the wall reference thickness, here taken constant, γ is a viscoelasticity coefficient which accounts for the damping effects due to the vessel material and the action of the surrounding tissue (by employing a simple Voigt/Kelvin model [12]). Finally, γ_2 is the longitudinal pre-load stress (it is well known that arteries in-vivo are normally under a longitudinal tension.

The idea is to manipulate the equation so to recover (after a few reasonable assumptions) a two-equation system.

In the following, we indicate by $\dot{A}$ and $\ddot{A}$ the first and second time derivative of A. We will substitute the following identities

$$\frac{\partial \eta}{\partial t} = \frac{1}{2\sqrt{\pi A}} \dot{A}, \qquad \frac{\partial^2 \eta}{\partial t^2} = \pi^{-\frac{1}{2}} \left(\frac{1}{2\sqrt{A}} \ddot{A} - \frac{1}{4\sqrt{A^3}} \dot{A}^2 \right)$$

that are derived from (1.2), into (1.37) while

$$\frac{\partial^2 \eta}{\partial z^2} = \pi^{-\frac{1}{2}} \left(\frac{1}{2\sqrt{A}} A'' - \frac{1}{4\sqrt{A^3}} (A')^2 \right),$$

having indicated with a $'$ the spatial derivative.

We obtain a relation that links the pressure also to the time and space derivatives of A, which we write in all generality as

$$P - P_{ext} = \tilde{\psi}(A, \dot{A}, \ddot{A}, A', A''; A_0) + \psi(A; A_0, \boldsymbol{\beta}),$$

where $\tilde{\psi}$ is a non-linear function which derives from the treatment of the terms containing the derivatives of $\boldsymbol{\eta}$. Since it may be assumed that the contribution to the pressure is in fact dominated by the term ψ, we will simplify this relationship by linearising $\tilde{\psi}$ around the state $A = A_0$, $\dot{A} = \ddot{A} = 0$ and $A' = A_0'$, $A'' = A_0''$. By doing that, after some simple algebraic manipulations, one finds

$$P - P_{ext} = \frac{\gamma_0}{2\sqrt{\pi A_0}} \ddot{A} + \frac{\gamma_1}{2\sqrt{\pi A_0}} \dot{A} + \frac{\gamma_1}{2\sqrt{\pi A_0}} (A - A_0)'' + \psi(A; A_0, \boldsymbol{\beta}), \tag{1.38}$$

Replacing this expression for the pressure in the momentum equation requires to compute the term

$$\frac{A}{\rho} \frac{\partial P}{\partial z} = \frac{\gamma_0 A}{2\rho\sqrt{\pi A_0}} \frac{\partial^3 A}{\partial z \partial t^2} + \frac{\gamma_1 A}{2\rho\sqrt{\pi A_0}} \frac{\partial^2 A}{\partial z \partial t} + \frac{\gamma_2 A}{2\rho\sqrt{\pi A_0}} \frac{\partial^3 (A - A_0)}{\partial z^3} + \frac{A}{\rho} \frac{\partial \psi}{\partial z}.$$

The last term in this equality may be treated as previously, while the first two terms may be further elaborated by exploiting the continuity equation. Indeed, we have

$$\frac{\partial^2 A}{\partial z \partial t} = -\frac{\partial^2 Q}{\partial z^2}, \quad \frac{\partial^3 A}{\partial z \partial t^2} = -\frac{\partial^3 Q}{\partial t \partial z^2}$$

Therefore, the momentum equation with the additional terms deriving from inertia, viscoelasticity, and longitudinal pre-stress becomes

$$\frac{\partial Q}{\partial t} + \frac{\partial F_2}{\partial z} - \frac{\gamma_0 A}{2\rho\sqrt{\pi A_0}}\frac{\partial^3 Q}{\partial t \partial z^2} - \frac{\gamma_1 A}{2\rho\sqrt{\pi A_0}}\frac{\partial^2 Q}{\partial z^2} - \frac{\gamma_2 A}{2\rho\sqrt{\pi A_0}}\frac{\partial^3 A}{\partial z^3} + \tilde{B}_2 = 0, \tag{1.39}$$

where with F_2 we have indicated the second component of F in (1.16) while $\tilde{B}_2 = B_2 + \frac{\gamma_2 A}{2\rho\sqrt{\pi A_0}}\frac{\partial^3 A_0}{\partial z^3}$ accounts for the possibility that A_0 is not constant. The continuity equation remains unaltered.

Remark 1.10. *This analysis puts into evidence that the wall inertia and longitudinal pre-stress introduce a* dispersive *(third order derivatives) term into the momentum equation, while the viscoelasticity has a* diffusive *(second order derivatives) effect.*

Remark 1.11. *The problem with the model just presented is that it is difficult to get reasonable values for the various constant. That is the reason why the simpler model is usually preferred, despite its limitations.*

Furthermore the characteristic of the differential problem changes with the appearance of second and even third order derivatives, which makes the numerical treatment and the identification of proper boundary conditions more troublesome.

Often, not all the effects are to be taken into account at the same time. For instance one may just add the inertia term.

1.3 Numerical discretisation of the basic model

We will here consider the equations in conservation form (1.16) and the simple algebraic relationship (1.12).

We then have

$$\begin{aligned}
\mathbf{F}(\mathbf{U}) &= \begin{bmatrix} Q \\ \alpha\dfrac{Q^2}{A} + \displaystyle\int_0^A c_1^2 dA \end{bmatrix} = \begin{bmatrix} Q \\ \alpha\dfrac{Q^2}{A} + \dfrac{\beta}{3\rho A_0}A^{\frac{3}{2}} \end{bmatrix} && (1.40) \\
\mathbf{B}(\mathbf{U}) &= \begin{bmatrix} 0 \\ K_R\frac{Q}{A} + \frac{A}{A_0\rho}\left(\frac{2}{3}A^{\frac{1}{2}} - A_0^{\frac{1}{2}}\right)\frac{\partial\beta}{\partial z} \quad - \\ \frac{\beta}{\rho}\frac{A}{A_0^2}\left(\frac{2}{3}A^{\frac{1}{2}} - \frac{1}{2}A_0^{\frac{1}{2}}\right)\frac{\partial A_0}{\partial z} \end{bmatrix}, && (1.41)
\end{aligned}$$

where we have taken into account of possible variations of A_0 (tapering) and of $\beta = Eh_0\sqrt{\pi}$ because of possible changes of the Young modulus E.

The flux Jacobian $\mathbf{H}$ may be readily computed as

$$\mathbf{H}(\mathbf{U}) = \frac{\partial \mathbf{F}}{\partial \mathbf{U}} = \begin{bmatrix} 0 & 1 \\ -\alpha\dfrac{Q^2}{A^2} + \dfrac{\beta}{2\rho A_0}A^{\frac{1}{2}} & 2\alpha\dfrac{Q}{A} \end{bmatrix}. \tag{1.42}$$

The characteristic variables are given in (1.32) while (1.34) gives the inverse relationship.

1.3.1 The Taylor-Galerkin scheme

We discretize our system by a second order Taylor-Galerkin scheme [7], which might be seen as the finite element counterpart of the well known Lax-Wendroff scheme. It has been chosen for its excellent dispersion error characteristic and its simplicity of implementation.

The derivation here is made sightly more involved than for the classical systems of conservation laws due to the presence of the source term.

From (1.16) we may write

$$\frac{\partial \mathbf{U}}{\partial t} = -\mathbf{B} - \frac{\partial \mathbf{F}}{\partial z} \tag{1.43}$$

$$\frac{\partial^2 \mathbf{U}}{\partial t^2} = -\mathbf{B}_{\mathbf{U}}\frac{\partial \mathbf{U}}{\partial t} - \frac{\partial}{\partial z}\left(\mathbf{H}\frac{\partial \mathbf{U}}{\partial t}\right) = \mathbf{B}_{\mathbf{U}}\left(\mathbf{B} + \frac{\partial \mathbf{F}}{\partial z}\right) + \frac{\partial (\mathbf{H}\mathbf{B})}{\partial z} + \frac{\partial}{\partial z}\left(\mathbf{H}\frac{\partial \mathbf{F}}{\partial z}\right), \tag{1.44}$$

where we have denoted $\mathbf{B}_{\mathbf{U}} = \dfrac{\partial \mathbf{B}}{\partial \mathbf{U}}$. We now consider the time intervals (t^n, t^{n+1}), for $n = 0, 1, \dots$, with $t^n = n\Delta t$, Δt being the time step, and we discretize in time using a Taylor series truncated at the second order, to obtain the following semi-discrete system for the approximation $\mathbf{U}^n$ of $\mathbf{U}(t^n)$

$$\begin{aligned}\mathbf{U}^{n+1} \;\; = \;\; & \mathbf{U}^n - \Delta t\frac{\partial}{\partial z}\left[\mathbf{F}^n - \frac{\Delta t}{2}\mathbf{H}^n\mathbf{B}^n\right] + \frac{\Delta t^2}{2}\left[\mathbf{B}^n_{\mathbf{U}}\frac{\partial \mathbf{F}}{\partial z}^n + \frac{\partial}{\partial z}\left(\mathbf{H}^n\frac{\partial \mathbf{F}^n}{\partial z}\right)\right] \\ & - \Delta t\left(\mathbf{B}^n + \frac{\Delta t}{2}\mathbf{B}^n_{\mathbf{U}}\mathbf{B}^n\right), \quad n = 0, 1, \dots, \end{aligned} \tag{1.45}$$

where $\mathbf{U}^0$ is provided by the initial conditions and $\mathbf{F}^n$ stands for $\mathbf{F}(\mathbf{U}^n)$ (a similar notation holds for $\mathbf{H}^n$, $\mathbf{B}^n$ and $\mathbf{B}^n_{\mathbf{U}}$).

The space discretisation is carried out using the Galerkin finite element method [26]. The interval $[0, L]$ is subdivided into N elements $[z_i, z_{i+1}]$, with $i = 0, \dots, N$ and $z_{i+1} = z_i + h_i$, with $\sum_{i=0}^{N-1} h_i = L$, where $h_i > 0$ is the local element size. Let V_h be the space of piecewise linear finite element functions (see Fig. 1.5) and $\mathbf{V}_h = [V_h]^2$, while $\mathbf{V}^0_h = [V^0_h]^2 = \{\mathbf{v}_h \in \mathbf{V}_h \,|\mathbf{v}_h = \mathbf{0}$ at $z = 0$ and $z = L\}$. It follows from standard finite element theory that $V_h = \mathrm{span}(\psi_i, \quad i = 0, \dots, N+1)$ while $V^0_h = \mathrm{span}(\psi_i, \quad i = 1, \dots, N)$, being ψ_i the linear finite element nodal function associated to the node at $z = z_i$. As usually done in finite element theory, the formulation will be written in a compact form by employing vector valued test functions $\boldsymbol{\psi}_h \in \mathbf{V}_h$. The discrete continuity and momentum equations are recovered by taking test functions of the form $\boldsymbol{\psi}_h = [\psi_h, 0]^T$ and $\boldsymbol{\psi}_h = [0, \psi_h]^T$, respectively.

At each time step we seek the solution $\mathbf{U}_h \in \mathbf{V}_h$ that we may write $\mathbf{U}^n_h(z, t) = \sum_{i=0}^{N+1} \mathbf{U}^n_i \psi_i(z, t)$, with $\mathbf{U}^n_i = [A^n_i, Q^n_i]$ the approximation of A and Q at mesh node z_i.

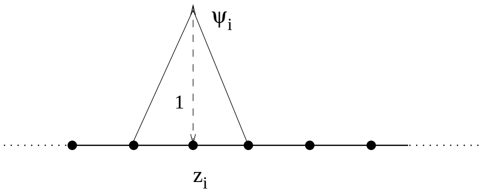

Figure 1.5: Linear finite element mesh and finite element nodal function ψ_i.

Further, we indicate by

$$(\mathbf{u}, \mathbf{v}) = \int_0^L \mathbf{u} \cdot \mathbf{v} dz$$

the $\mathbf{L}^2(0, L)$ scalar product.

Using the abridged notations $\mathbf{F}_{LW}(\mathbf{U}) = \mathbf{F}(\mathbf{U}) - \frac{\Delta t}{2}\mathbf{H}(\mathbf{U})\mathbf{B}(\mathbf{U})$ and $\mathbf{B}_{LW}(\mathbf{U}) = \mathbf{B}(\mathbf{U}) + \frac{\Delta t}{2}\mathbf{B}_{\mathbf{U}}(\mathbf{U})\mathbf{B}(\mathbf{U})$, the finite element formulation of (1.45) is :

given $\mathbf{U}_h^0$ obtained by interpolation from the initial data, for $n \geq 0$, find $\mathbf{U}_h^{n+1} \in \mathbf{V}_h$ which satisfies the following equations for the interior nodes

$$\begin{aligned}(\mathbf{U}_h^{n+1}, \boldsymbol{\psi}_h) = (\mathbf{U}_h^n, \boldsymbol{\psi}_h) + \Delta t \left(\mathbf{F}_{LW}(\mathbf{U}_h^n), \frac{d\boldsymbol{\psi}_h}{dz}\right) - \frac{\Delta t^2}{2}\left(\mathbf{B}_{\mathbf{U}}(\mathbf{U}_h^n)\frac{\partial \mathbf{F}(\mathbf{U}_h^n)}{\partial z}, \boldsymbol{\psi}_h\right) \\ - \frac{\Delta t^2}{2}\left(\mathbf{H}(\mathbf{U}_h^n)\frac{\partial \mathbf{F}}{\partial z}(\mathbf{U}_h^n), \frac{d\boldsymbol{\psi}_h}{dz}\right) - \Delta t \left(\mathbf{B}_{LW}(\mathbf{U}_h^n), \boldsymbol{\psi}_h\right), \ \forall \boldsymbol{\psi}_h \in \mathbf{V}_h^0 \quad (1.46)\end{aligned}$$

together with the relation for boundary nodes obtained from the boundary and compatibility conditions, as discussed in the next section. By taking $\boldsymbol{\psi}_h = [\psi_i, 0]^T$ and $\boldsymbol{\psi}_h = [0, \psi_i]^T$, for $i = 1, \ldots N$ we obtain N discrete equations for continuity and momentum, respectively, for a total of $2(N+2)$ unknowns (A_i and Q_i for $i = 0, \ldots, N+1$). The boundary and compatibility conditions have then to provide four additional relations.

System (1.46) has been obtained by multiplying (1.45) by $\boldsymbol{\psi}_h$, integrating over the domain and applying integration by parts on the spatial derivative terms. No boundary terms appear as a result of this operation since $\boldsymbol{\psi}_h$ is zero at the boundary.

It is well known that, thanks to chioce of linear finite elements, the term on the left-hand side will give rise to a tridiagonal system governed by the so called *mass matrix*. By performing the *lumping* of the mass matrix [26] we may reduce the system to a diagonal one, very simple to solve. Yet this will downgrade the dispersion characteristics of the scheme.

Remark 1.12. *The integrals in (1.46) involve the non-linear functions* $\mathbf{F}$ *and* $\mathbf{H}$*. In order to compute them we might resort to numerical integration. A possibility is to take a piecewise linear approximation for the fluxes, i.e.* $\mathbf{F}(\mathbf{U}) \simeq \sum_{i=0}^{N+1} \mathbf{F}(\mathbf{U}_i^n)\psi_i$*, while employing a piecewise constant approximation for* $\mathbf{H}$*.*

It is however important to ensure that the chosen approximation is strongly consistent *with respect to constant solution, i.e. that the discrete scheme be still able to represent constant solution exactly. In particular, if the initial conditions are* $Q = 0$ *and* $A = A_0$ *and the boundary conditions such that no waves are entering the domain, then the trivial constant solution* $Q = 0$, $A = A_0$ *of the differential problem has to be also a solution of the discrete system, i.e. we must have* $A_i^n = A_0(z_i)$ *and* $Q_i^n = 0$ *at all time steps.*

A third-order scheme (in time) may be derived by following the indications in [1]. However, in our case this would imply the coupling of the equations for A_h and Q_h, that are instead completely decoupled in (1.46), thus incresing the computational costs. For this reason, we have considered only the second-order scheme. However, many of the considerations that we develop in this note apply also to the third-order version.

The second order Taylor-Galerkin scheme (1.46) entails a time step limitation. A linear stability analysis [23] indicates that the following condition should be satisfied

$$\Delta t \leq \frac{\sqrt{3}}{3} \min_{0\leq i\leq N}\left[\frac{h_i}{\max_{k=i}^{i+1}(c_{\alpha,k}+|\overline{u}_k|)}\right], \tag{1.47}$$

where $c_{\alpha,i}$ and $\overline{u}_i$ here indicate the values of c_α and $\overline{u}$ at mesh node z_i, respectively. This condition corresponds to a CFL number of $\frac{\sqrt{3}}{3}$, typical of a second order Taylor-Galerkin scheme in one dimension [23]. Another modification proposed in [1] allows to extend the CFL number limit to 1 while maintaining a second order scheme. For the sake of simplicity we do not provide here more details, which may be found in the cited literature.

1.3.2 Boundary and compatibility conditions

Formulation (1.46) provides the values only at internal nodes, since we have chosen the test functions $\mathbf{v}_h$ to be zero at the boundary. The values of the unknowns at the boundary nodes must be provided by the application of the *boundary* and *compatibility* conditions.

The boundary conditions are not sufficient to close the problem *at numerical level* since they provide just two conditions, yet we need to find four additional relations. We want to stress that this problem is linked to the numerical scheme, not to the differential equations, which indeed only require one condition at each end (at least for the flow regime we are considering here).

Without loss of generality, let us consider the boundary $z = 0$ (analogous consideration may be made at $z = L$). Following the considerations made in Sect. 1.2.2, the boundary conditions will provide at each time step a relation of the type

$$\phi(A_0^{n+1}, Q_0^{n+1}) = q_0(t^{n+1}),$$

being q_0 the given boundary data. For instance, imposing the pressure would mean choosing $\phi(A,Q) = P = \psi(A; A_0(0), \beta(0))$, while imposing the mass flux would just mean $\phi(A,Q) = Q$. Finally, a non reflecting condition is obtained by $\phi(A,Q) = W_1(A,Q)$ and in this case q_0 is normally taken constant and equal to the value of W_1 at a reference state (typically $(A,Q) = (A_0, 0)$). Thus, in general ϕ is a non linear function.

This relation should be supplemented by a *compatibility condition*. In general , the compatibility conditions are obtained by projecting the equation along the eigenvectors corresponding to the characteristics that are exiting the domain. Therefore, we have to discretise the following set of equations at the two vessel ends [26].

$$\mathbf{l}_2 \cdot \left(\frac{\partial}{\partial t}\mathbf{U} + \mathbf{H}\frac{\partial \mathbf{U}}{\partial z} + \mathbf{S}(\mathbf{U})\right) = 0, \quad z = 0,\, t \in I, \tag{1.48a}$$

$$\mathbf{l}_1 \cdot \left(\frac{\partial}{\partial t}\mathbf{U} + \mathbf{H}\frac{\partial \mathbf{U}}{\partial z} + \mathbf{S}(\mathbf{U})\right) = 0, \quad z = L,\, t \in I. \tag{1.48b}$$

These two equations have to be suitable discretised in space and time. A possibility is to replace the content inside the two parentheses with the Taylor-Galerkin scheme written for the corresponding boundary point. This is obtained by taking as test function $\boldsymbol{\psi}_h$ in (1.46) the *linear finite element nodal function associated to the boundary node* at $z = 0$ and $z = L$, respectively. We need also to specify the value $\mathbf{l}_1$ and $\mathbf{l}_2$ (which are indeed function of $\mathbf{U}$!): one normally takes the value computed using the approximation of $\mathbf{U}_h$ at the previous time step. We have also to be aware o the fact that additional boundary integral terms will now appear in the formulation (1.46) because now the test function is not zero at the boundary. However, this may not be true in special cases.

Yet, although this technique has the advantage of ensuring that the discretisation error introduced by the compatibility conditions is of the same order of that of the numerical scheme it has the drawback of coupling the equation at the boundary nodes. An alternative which maintains a decoupled scheme is found by noting that (1.48) are in fact equivalent to equations (1.25) collocated respectively at node $z = 0$ and $z = L$.

Therefore at each time step we should solve

$$\frac{d}{dt}W_2(t, y_2(t)) + G_1 = 0, \quad \frac{d}{dt}W_1(t, y_1(t)) + G_2 = 0, \tag{1.49}$$

with $y_2(t^{n+1}) = 0$ and $y_1(t^{n+1}) = L$, respectively. Whenever $G_1 = G_2 = 0$ the solution is obtained by tracing back the characteristic lines exiting the domain and imposing that the corresponding characteristic variable is constant. A first order (in time) approximation would then give

$$W_2^{n+1}(0) = W_2^n(-\lambda_2^n(0)\Delta t), \quad W_1^{n+1}(L) = W_1^n(L - \lambda_1^n(L)\Delta t).$$

Thanks to the CFL condition we are sure that the foot of the characteristic line falls within the first (last) element.

A second order approximation might be obtained by following the technique described in [4]. When $\mathbf{G}(\mathbf{U}) \neq \mathbf{0}$ the values of $W_2^{n+1}(0)$ and $W_1^{n+1}(L)$ will have to be computed by numerically solving the associated ordinary differential equations (1.29).

Then, at $z = 0$ we have

$$\phi(A_0^{n+1}, Q_0^{n+1}) = q(t^{n+1}), \quad W_2(A_0^{n+1}, Q_0^{n+1}) = W_2^{n+1}(0), \tag{1.50}$$

where $W_2^{n+1}(0)$ has been obtained with the characteristic extrapolation technique just described. This is a non-linear system for the two unknowns A_0^{n+1} and Q_0^{n+1} at the boundary, which may be solved by a Newton method. Usually, by taking the values at the previous iteration as starting point, just few iterations are required to reach a tolerance within machine precision. The same approach may be repeated at the other boundary node.

Finally, a generic time step from t^n to t^{n+1} requires

- Solving the system for the boundary values A_h^{n+1} and Q_h^{n+1} at the boundary nodes (two uncoupled systems of non-linear equations for 4 unknowns in total);

- Using (1.46) to advance the interior nodes.

Remark 1.13. *The boundary system (1.50) might be simplified further by performing a suitable linearisation. Yet, since the cost of the Newton iterations at the boundary points is negligible compared to that of the calculation of the interior values, there is little practical advantage in doing so. Furthermore, one may add further approximation errors difficult to control.*

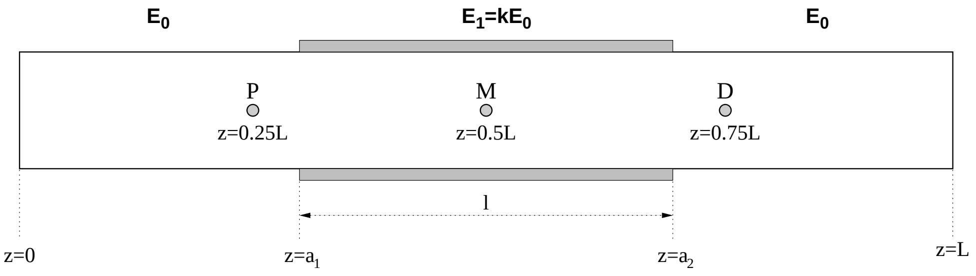

Figure 1.6: The layout of our numerical experiment.

1.3.3 Some numerical tests

Here we describe some numerical experiments we have performed in order to assess the numerical scheme just presented. We will consider the situation of a stented artery and study the changes in pressure pattern induced by the abrupt changes in the elastic characteristics due to the presence of the stent, which is a metallic wire frame which is expanded and permanently placed inside a stenosed artery in order to restore the lumen section. Fig. 1.6 shows the layout of the numerical experiment.

Three types of pressure input have been imposed at $z = 0$, namely an impulse input, that is a single sine wave with a small time period, a single sine wave with a more realistic time period and a periodic sine wave (see Fig. 1.7). The impulse have been used to better highlight the reflections.

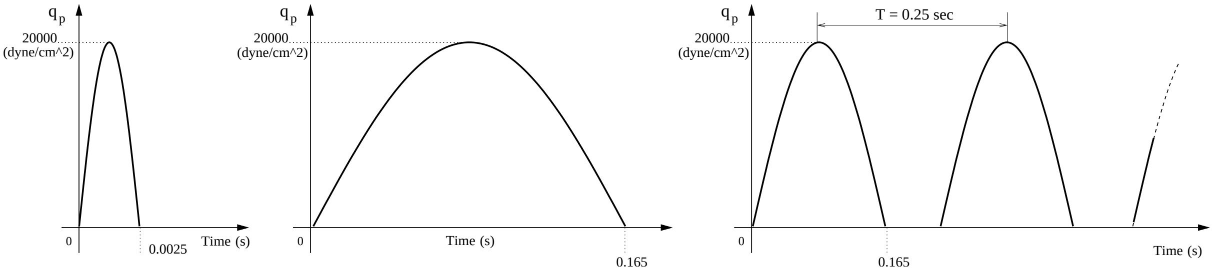

Figure 1.7: The three types of pressure input profiles used in the numerical experiments: an impulse (left) a more realistic sine wave (middle) and a periodic sine wave (right).

The part that simulates the presence of the prosthesis or stent of length l is comprised between coordinates a_1 and a_2. The corresponding Young's modulus has been taken as a multiple of the basis Young's modulus E_0 associated to the physiological tissue.

Three locations along the vessel have been identified and indicated by the letters D (distal), M (medium) and P proximal. They will be taken as monitoring point for the pressure variation. Different prosthesis length l have been considered; in all cases points P and D are located outside the region occupied by the prosthesis. Table 1.1 indicates the basic data which have been used in all numerical experiments. A time step $\Delta t = 2 \times 10^{-6}$s and the initial values $A = A_0$ and $Q = 0$ have been used throughout. We have also neglected the friction term, so that the source term $\mathbf{B}$ in equation (1.16) is zero and we have adopted (1.12) for the pressure-area relationship and put $P_{ext} = 0$.

The boundary data for this numerical tests are as follows. At the distal boundary $z = L$ we impose non reflecting boundary conditions by leaving W_2 constant and equal to its reference

	Parameter	
	Input Pressure Amplitude	$20\text{x}10^3\text{dyne/cm}^2$
FLUID	Viscosity, ν	0.035poise
	Density, ρ	1g/cm^3
	Young's Modulus, E_0	$3\text{x}10^6\text{dyne/cm}^2$
STRUCTURE	Wall Thickness, h	0.05cm
	Reference Radius, R_0	0.5cm

Table 1.1: Data used in the numerical experiments.

value. This simulates a tube of "infinite" length. At the proximal boundary, we would like to impose the chosen pressure input $p(0,t) = q_p(t)$. Yet, as already noted a direct imposition of the pressure will produce a reflecting boundary condition. To eliminate the reflections at the proximal boundary we would have to impose the incoming characteristic variable W_1. Therefore, we wish to transform the pressure condition in a condition on W_1. By recalling the expression of the characteristic variables given in 1.32) we note that we may write W_1 as function of P and W_2, as follows:

$$W_1(P, W_2) = W_2 + \frac{4}{\sqrt{\rho}}\left(\sqrt{P - \beta_0\sqrt{A_0}} - c_{1,0}\right).$$

Then we keep W_2 fixed at its initial value, $W_2 = W_{2,0}$ and impose at $z = 0$

$$W_1(t) = W_{2,0} + \frac{4}{\sqrt{\rho}}\left(\sqrt{q_p(t) - \beta_0\sqrt{A_0}} - c_{1,0}\right). \tag{1.51}$$

Although this relation imposes the pressure only implicitly and not in exact terms, it has been proved very effective and enjoys good non-reflecting properties. Furthermore, it has been found that in practice the pressure level obtained by this treatment differ by little (at most a few percent) by the values provided by q_p. This confirms that the propagation phenomena are strongly dominated by the pressure.

The formulation illustrated so far does not allow for a discontinuous variation of the Young modulus E. Therefore, we smoothed out the transition between E_0 and E_1, as depicted in Fig. 1.8. A transition zone of thickness 2δ has been set around the point $z = a_1$ and $z = a_2$. In that region the Young modulus varies between E_0 and E_1 with a fifth order polynomial law.

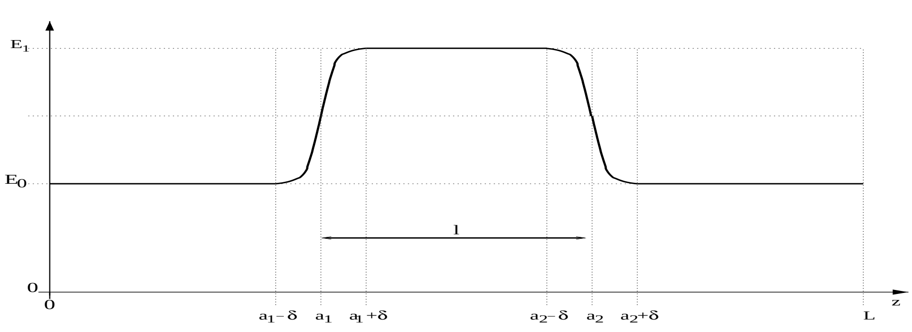

Figure 1.8: Variation of Young's modulus.

Case of an impulsive pressure wave

In Fig. 1.9 we show the results obtained for the case of a pressure impulse. We compare the results obtained with uniform Young's modulus E_0 and the corresponding solution when $E_1 = 100E_0$, $l = a_2 - a_1 = 5\text{cm}$ and $\delta = 0.5\text{cm}$. We have taken $L = 15\text{cm}$ and a non uniform mesh of 105 finite elements, refined around the points a_1 and a_2. When the Young modulus is uniform, the impulse travels along the tube undisturbed. In the case of varying E the situation changes dramatically. Indeed, as soon as the wave enters the region at higher Young's modulus it gets partially reflected (the reflection is registered by the positive pressure value at point P and $t \approx 0.015\text{s}$) and it accelerates. Another reflection occurs at the exit of the 'prosthesis', when E returns to its reference value E_0. The point M indeed registers an oscillatory pressure which corresponds to the waves that are reflected back and forth between the two ends of the prosthesis. The wave at point D is much weaker, because part of the energy has been reflected back and part of it has been 'captured' inside the prosthesis itself.

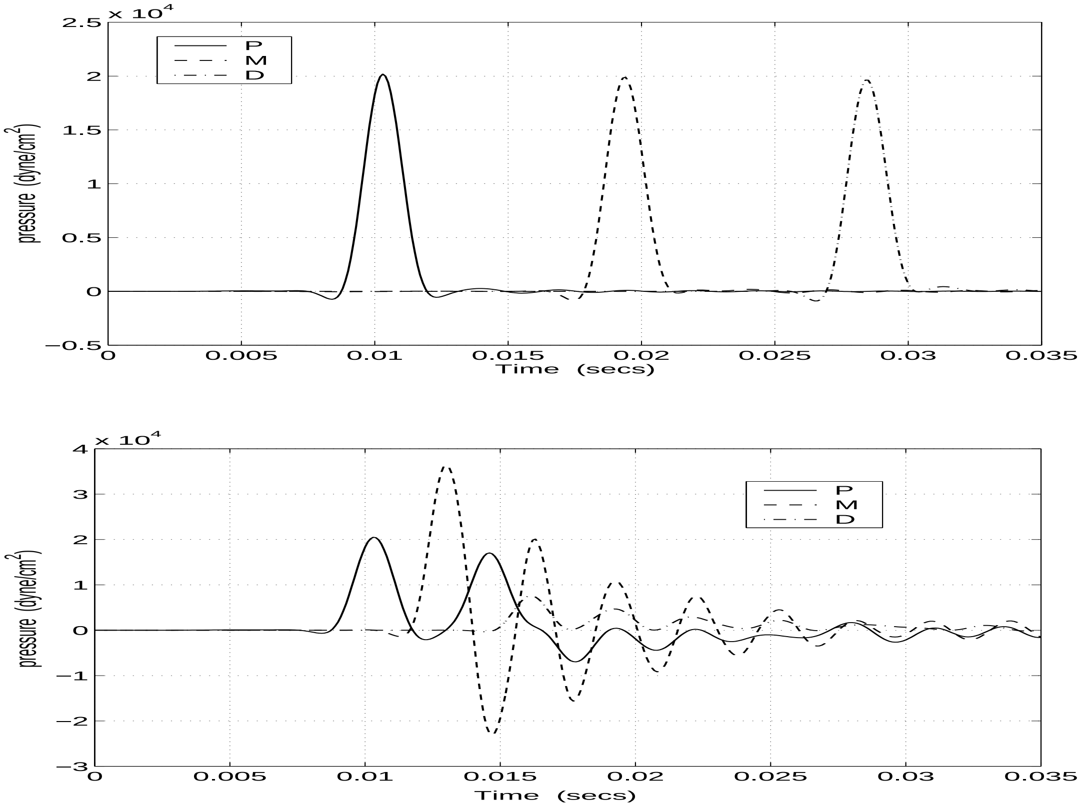

Figure 1.9: Pressure history at points P, M and D of figure 1.6, for an impulsive input pressure, in the case of constant (upper) and variable (lower) E.

Case of a sine wave

Now, we present the case of the pressure input given by the sine wave with a larger period shown in Fig. 1.7. We present again the results for both cases of a constant and a variable E. All other problem data have been left unchanged from the previous simulation. Now, the interaction among the reflected waves is more complex and eventually results in a less oscillatory solution (see Fig. 1.10). The major effect of the presence of the stent is a pressure build-up at the proximal point P, where the maximum pressure is approximately $2500 \mathrm{dynes/cm^2}$ higher than in the constant case. By a closer inspection one may note that the interaction between the incoming and reflected waves shows up in discontinuities in the slope, particularly for the pressure history at point P. In addition, the wave is clearly accelerated inside the region where E is larger.

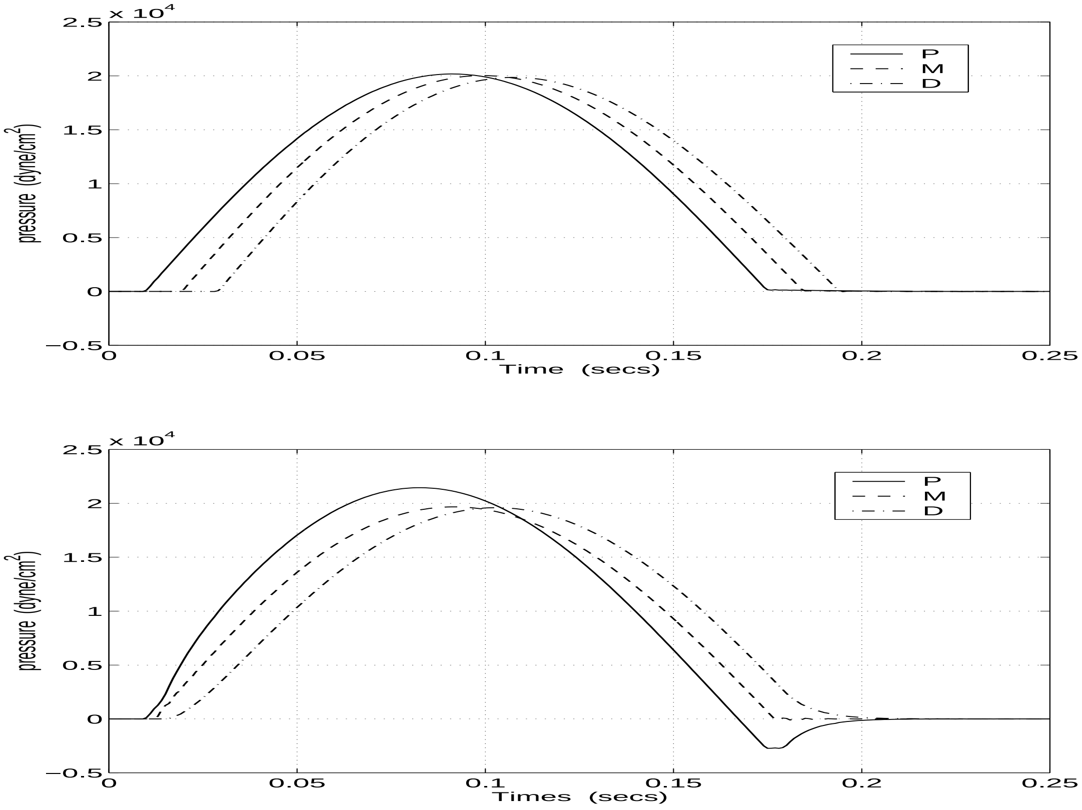

Figure 1.10: Pressure history at points P, M and D of figure 1.6, for a sine wave input pressure, in the case of constant (upper) and variable (lower) E.

In table 1.2 we show the effect of a change in the length of the prosthesis by comparing the maximum pressure value recorded for a prosthesis of 4, 14 and 24 cm, respectively. The values shown are the maximal values in the whole vessel, over one period. Here, we have taken $L = 60\mathrm{cm}$, $\delta = 1\mathrm{cm}$, a mesh of 240 elements and we have positioned in the three cases the prosthesis in the middle of the model. The maximum value is always reached at a point upstream the prosthesis. In the table we give the normalised distance between the upstream prosthesis section and of the point where the pressure attains its maximum.

Finally, we have investigated the variation of the pressure pattern due to an increase of $k = E/E_0$. Fig. 1.11 shows the result corresponding to $L = 20\mathrm{cm}$ and $\delta = 1\mathrm{cm}$ and various values for k. The numerical result confirms the fact that a stiffer prosthesis causes a higher excess pressure in the proximal region.

Prosthesis length (cm)	*Maximal pressure* (dyne/cm^2)	*Maximum location* $z_{\max}/l$
4	23.5×10^3	0.16
14	27.8×10^3	0.11
24	30.0×10^3	0.09

Table 1.2: Maximum pressure value for prosthesis of different length.

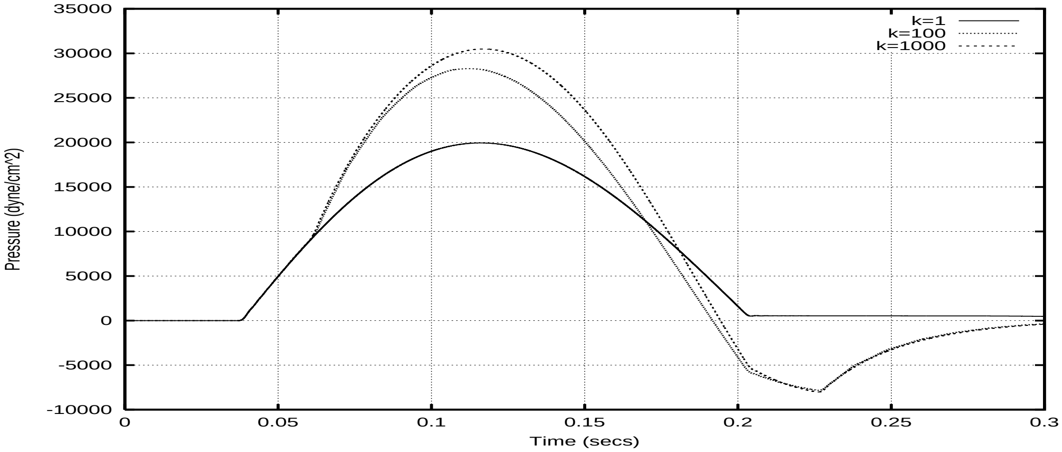

Figure 1.11: Pressure history at point P of figure 1.6, for a sine wave input pressure and different Young's moduli $E = kE_0$.

Case of a periodic sine wave

We consider here the case where the sine wave of the previous test case is repeated periodically with a period $T = 0.25\text{sec}$ as illustrated in Fig. 1.7. We have taken $L = 120\text{cm}$ and a prosthesis of 10cm between the points $a_1 = 70\text{cm}$ and $a_2 = 80\text{cm}$. All other problem data have been left unchanged. We have simulated six periods. Fig. 1.12 shows the pressure at the proximal position $z = 40\text{cm}$, i.e. a point which is 30cm far from the prosthesis. In that position, the incoming pressure wave adds to the reflected one and the result is a build-up of the maximum pressure of approximately $2650\text{dyne}/\text{cm}^2$. This simulation shows that the effects of the presence of a prosthesis are remarkable even far away form the prosthesis in the proximal region.

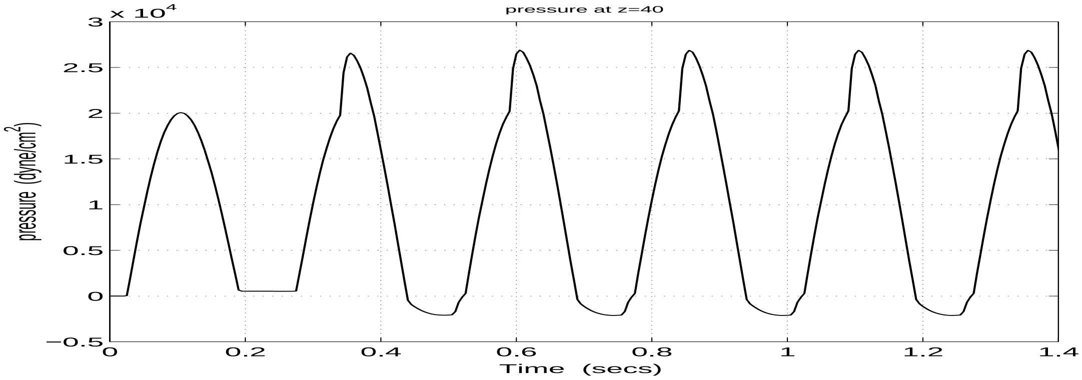

Figure 1.12: Pressure history at point $z = 40\text{cm}$, for a periodic sine wave input, in the case of a prosthesis positioned between $a_1 = 70\text{cm}$ and $a_2 = 80\text{cm}$.

1.4 Towards a network of one dimensional models

In this section we will introduce a domain decomposition method for branching. The vascular system is in fact a network of vessels that branches repeatedly and a model of just an artery is of little use. A simple and effective idea is to describe the network by 'gluing' together one dimensional models. Yet, we need to find proper interface conditions (i.e. mathematically sound and easy to treat numerically).

The technique may be adopted also in the case of abrupt changes of vessel characteristics, as an alternative to the regularisation presented in the previous section. Indeed, we will treat first the simple case of the coupling of two cylindrical segments of teh same artery, possibly featuring different mechanical properties..

1.4.1 Domain decomposition approach for prosthesis simulation

We consider the case of a single discontinuity at $z = \Gamma \in (0, L)$ of the Young modulus E and thus of coefficient β_0 in the pressure-area relationship (1.12), which is the one we adopt in this section. By following the arguments in [5] we may infer that in this situation A (and consequently P) is (in general) discontinuous at $z = \Gamma$. As a consequence, the product $A\frac{\partial P}{\partial z}$ in the momentum equation cannot be properly defined. This is the reason while the model is inadequate in this situation. However, the technique of regularization of E used in the previous section requires to employ of a fine mesh around Γ to properly represent the transition, with a consequent loss of efficiency of the numerical scheme. Also as a consequence of the CFL condition, which obliges us to use smaller time steps as the spacing gets finer [13]. Furthermore, if the solution is very steep, the Taylor-Galerkin scheme should be stabilised to avoid spurious oscillations, like all second-order schemes for non-linear hyperbolic problems, with the inevitable addition of extra numerical dissipation (and a more complex coding!).

Following the domain decomposition approach [27] we instead partition the vessel Ω into two subdomains $\Omega_1 = (0, \Gamma)$ and $\Omega_2 = (\Gamma, L)$ as shown in Fig. 1.13 and solve the original problem in the two subdomains separately. Yet, we need to find the proper interface conditions at Γ. For a standard system in conservation form, this would entail the continuity of the fluxes, which corresponds to the Rankine-Huguenot condition for a discontinuity that does not propagate [13]. Unfortunately, it is arguable whether the Rankine-Hugeunot conditions are applicable in our case since can the equations in form (1.16) *have been obtained under the assumption that the solution be smooth*.

Clearly, this problem concerns only the momentum equation as the continuity equation is originally in conservation form and, by standard arguments we derive that mass flux is continuous across the interface (a fact that agrees also with the physical intuition), that is $[Q] = Q^+ - Q^- = 0$, having indicated with a $+$ and a $-$ quantities respectively on the left and on the right of the interface Γ.

The interface condition for the momentum equation has to be driven instead by other considerations. A choice often adopted in the literature [21] is to impose the continuity of pressure. This condition just extrapolates what is done in simpler, linearised models, where the effect of the convective term in the momentum equation has been neglected. Yet, in our non-linear model, this condition allows for a possible increase of the energy of the system through the discontinuity, a condition hardly justifiable by physical means.

In [9, 8] it has been shown that for the model at hand and in the case $\alpha = 1$ a condition which ensures that the domain decomposed problem has the same stability properties of the ’uncoupled’ one is the continuity of the total average pressure, $P_t = P + \frac{1}{2}\rho\overline{u}^2 = P + \frac{\rho}{2}\left(\frac{Q}{A}\right)^2$, across the interface (together with the continuity of mass flux already established).

Then, referring again to Fig. (1.13), the coupled problem reads, in each domain Ω_i, $i = 1, 2$

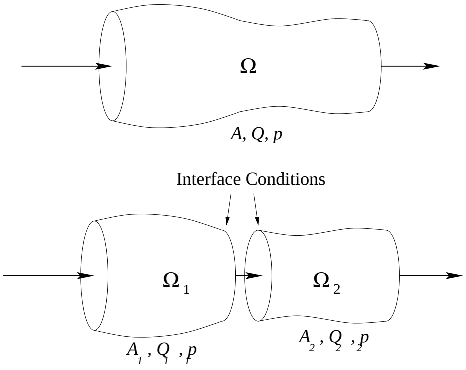

Figure 1.13: Domain decomposition of an artery featuring a discontinuous Young modulus

and for all $t \in I$,

$$\begin{cases} \dfrac{\partial A_i}{\partial t} + \dfrac{\partial Q_i}{\partial z} = 0 \\ \dfrac{\partial Q_i}{\partial t} + \dfrac{\partial}{\partial z}\left(\dfrac{Q_i^2}{A_i}\right) + A_i \dfrac{\partial P_i}{\partial z} + K_R \dfrac{Q_i}{A_i} = 0 \end{cases} \tag{1.52}$$

together with the interface conditions

$$\begin{cases} Q_1 = Q_2 \\ P_{t,1} = P_{t,2} \end{cases} \qquad \text{at } z = \Gamma, \tag{1.53}$$

and appropriate initial and boundary conditions at $z = 0$ and $z = L$.

To solve the problems in Ω_1 and Ω_2 separately, we have devised a decoupling technique which, at each time step from t^n to t^{n+1}, provides the Taylor-Galerkin algorithm with the values of the unknowns at the interface Γ. Since the interface conditions (1.53) are not enough to close our problem we have to supplement them with some compatibility conditions of the type discussed in Sect. 1.3.2, for instance in the form of the extrapolation of the characteristic variables exiting Ω_1 and Ω_2 at Γ.

We here indicate with W_1^- and W_2^+ the values at $z = \Gamma$ and $t = t^{n+1}$ of the (outgoing) characteristic variables W_1 and W_2, relative to domain Ω_1 and Ω_2, respectively, obtained by extrapolation from the data at $t = t^n$. While $W_i^-(A, Q)$ and $W_i^+(A, Q)$, for $i = 1, 2$ indicate the relations (1.31) computed at the two sides of the interface. We finally obtain the following non-linear system for the interface variables A^+, A^-, Q^+ and Q^- at time step $n + 1$

$$\begin{cases} Q^- - Q^+ = 0 \\ \psi(A^-; A_0^-, \beta_0^-) + \frac{\varrho}{2}\left(\dfrac{Q^-}{A^-}\right)^2 - \psi(A^+; A_0^+, \beta_0^+) + \frac{\varrho}{2}\left(\dfrac{Q^+}{A^+}\right)^2 = 0 \\ W_1^-(A^-, Q^-) - W_1^- = 0 \\ W_2^+(A^+, Q^+) - W_2^+ = 0 \end{cases} \tag{1.54}$$

which is solved again by a Newton scheme. For the sake of generality, we have assumed that also the reference section area A_0 might be discontinuous at $z = \Gamma$. It has been verified that the determinant of the Jacobian of system (1.54) is different from zero for all allowable values of the parameters, thus guaranteeing that the Newton iteration is well-posed. It has also been found that, by using as starting values the unknowns at time t^n, the method converges in few iterations with a tolerance of 10^{-8} on the relative increment.

For values of pressure and velocities typical of blood flow the value of pressure is much greater than the kinetic energy $\frac{\varrho}{2}\bar{u}^2$ This explains why the use of continuity of pressure (instead of total pressure) at the interface may in fact be employed without normally encountering stability problems. However, the conditions provided by (1.53) are, in our opinion, more sound.

Another alternative, which guarantees again a stability property, follows from the physical argument that the change of total pressure along the flow at Γ should be a non positive function of the mass flux. To account for this, one could impose instead of the second relation in (1.54) a relation of the type

$$P_t^+ - P_t^- = -\operatorname{sign}(Q) f(Q), \quad \text{at } z = \Gamma,$$

being f a positive monotone “energy dissipation function” satisfying $f(0) = 0$. However, the difficulties of finding an appropriate f for the problem at hand has brought us to consider only the continuity of total pressure, which clearly corresponds to $f \equiv 0$.

1.4.2 Branching

The flow in a bifurcation is intrinsically three dimensional; yet it may still be represented by means of a 1D model, following a domain decomposition approach, if one is not interested in the flow details inside the branch. Figure 1.14 shows a model for a bifurcation. We have simplified the real geometric structure by imposing that the bifurcation is located exactly on one point and neglecting the effect of the bifurcation angles. This approach has been followed also by other authors, like [22]. An alternative technique is reported in [32], where a separate tract containing the branch is introduced.

In order to solve the three problems in Ω_1 (main branch), Ω_2 and Ω_3 we need to find again appropriate interface conditions. The hyperbolic nature of the problem tells us that we need three conditions.

We follow the same route as before and we first state the conservation of mass across the bifurcation, i.e.

$$Q_1 = Q_2 + Q_3, \quad \text{at } z = \Gamma, t \in I. \tag{1.55}$$

We note that the orientation of the axis in the three branches is such that a positive value of Q_1 indicates that blood is flowing from the main branch Ω_1 into the other two. Again an energy analysis similar to that of the previous section allows us to conclude that a proper interface condition would entail the condition $P_{t,1}Q_1 - P_{t,2}Q_2 - P_{t,3}Q_3 \geq 0$. It is expected that the complex flow in the bifurcation will cause an energy dissipation and consequently a decrease in the total pressure in the direction of the flow field across the bifurcation, and this loss should be related to the fluid velocity (or flow rate) and to the bifurcation angles.

A possibility to account for this is to impose, at $z = \Gamma$, that

$$\begin{aligned} P_{t,1} - \text{sign}(\bar{u}_1) f_1(\bar{u}_1) &= P_{t,2} + \text{sign}(\bar{u}_2) f_2(\bar{u}_2, \alpha_2), \\ P_{t,1} - \text{sign}(\bar{u}_1) f_1(\bar{u}_1) &= P_{t,3} + \text{sign}(\bar{u}_3) f_3(\bar{u}_3, \alpha_3), \end{aligned} \tag{1.56}$$

where α_2 and α_3 are the angles of the branches Ω_2 and Ω_3 with respect to the main one (see fig. 1.15); f_1, f_2 and f_3 are positive functions and equal to zero when the first argument is zero. These can be chosen to be:

$$f_1(u) = \gamma_1 u^2, \quad f_i(u, \alpha) = \gamma_i u^2 \sqrt{2(1 - \cos\alpha)}, \; i = 2, 3, \tag{1.57}$$

where the γ_i are non-negative coefficients. Again, because of the complexity of obtaining the correct value for the γ_i it is usually preferred to just impose the continuity of total pressure, i.e

$$P_{t,1} = P_{t,2} = P_{t,3}, \quad \text{at } z = \Gamma. \tag{1.58}$$

which satisfies the stability condition (when coupled with the continuity of mass fluxes) and correspond to choosing all the γ_i equal to zero.

In the numerical scheme, (1.55) and (1.56) will be complemented by three compatibility relations, which can be expressed again by the extrapolation of the outgoing characteristic variables. We have thus a non linear system for the six unknowns A_i^{n+1}, Q_i^{n+1}, $i = 1, 2, 3$, at the interface location Γ, which is again solved by a Newton iteration.

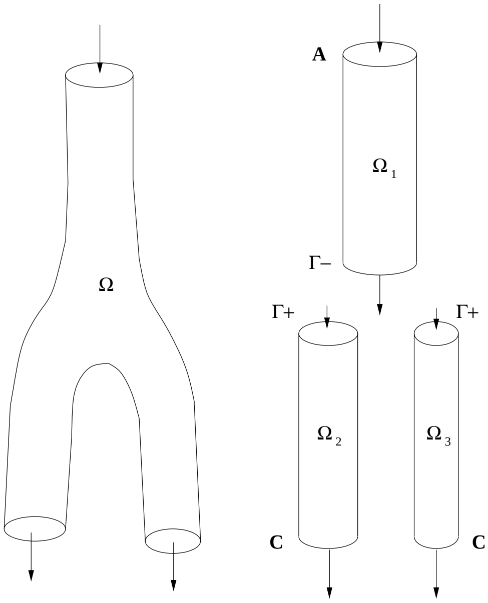

Figure 1.14: One dimensional model of bifurcation by domain decomposition technique

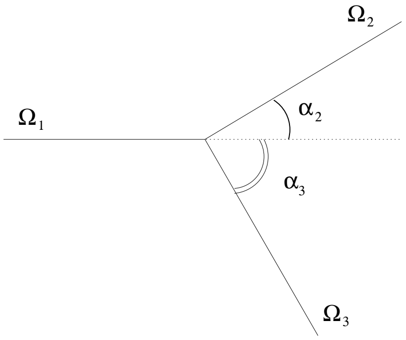

Figure 1.15: A sketch of a branching.

1.4.3 A numerical test: bifurcated channel with endograft

Here we show an application of the one dimensional model to a real-life problem. Abdominal aortic aneurysms (AAA) represent a significant and important vascular disease. They are characterised by an abnormal dilatation of a portion of the aorta. This swollen region would enlarge with time and, without a surgical treatment, it will eventually break with fatal consequences. Even if open surgical repair is still the standard treatment for AAA, endografts and endovascular stent grafts begin to play a major role as they allow a less invasive treatment (fig. 1.16).

The presence of an endograft may be treated by our one-dimensional model as a bifurcated channel with varying mechanical properties, as shown in Fig. 1.17. The domain is decomposed into 6 regions, Ω_i, $i = 1, \dots, 6$ and the interface conditions of type (1.53) or (1.55)-(1.58) are used where appropriate.

A preliminary numerical test has been carried out by selecting all Ω_i to be of equal length L=5 cm. We considered everywhere ρ =1 gr/cm^3, $\nu = 0.035\ cm^2/s$, $\alpha = 1$, h_0 =0.05 cm; while the Young's moduli have been taken to be equal to $E_{endograft} = 60\ 10^6\ dyne/cm^2$ for the endografted part (Ω_i, $i = 2, 3, 5$) and $E_{vessel} = 10\ 10^6\ dyne/cm^2$ for the remaining subdomains. The vessel reference radii have been taken to be $R_{0,1} = R_{0,2} = 0.6\ cm$, $R_{0,3} = R_{0,4} = 0.4\ cm$ and $R_{0,5} = R_{0,6} = 0.5\ cm$.

At inlet we have imposed a half sine pressure wave of period 0.1 s and amplitude 20000 $dyne/cm^2$.

The spatial grid was uniform with a total of 546 nodes. The computations were carried out with a time step Δt 0.00001 s.

Figures 1.18, 1.19, 1.20 report the time evolution for the area A and the two characteristic variables W_1 and W_2 at three given points, respectively at the middle of Ω_1, and of Ω_2 and of Ω_6. By inspecting figure 1.18 we remark that in W_1 we find the input wave imposed at inlet, while in W_2 we find the composition of two effects, the wave reflected from the beginning of the endograft and the wave reflected from the branching point. These modify the sinusoidal shape of the area A. On Figure 1.19 we find in W_2 only the wave reflected from the branching point. Finally, in figure 1.20 we do not find reflected waves (being the outlet boundary condition an absorbing one); moreover, in W_1 we can observe the part of the wave passing through the branches.

1.4.4 Simulation of a complex arterial network

Here we report on a simulation for a network formed by the main 55 arteries of the human cardiovascular system, more details may be found in [29]. The results shown here are indeed the same reported in this reference and have been obtained using a different numerical scheme, namely Discontinuous-Galerkin finite elements. However, the simulations have been repeated using the Taylor-Galerkin approach, with negligible difference in the obtained results.

Figure 1.21 shows the connectivity of the arteries used in our model of the arterial network, while the numerical values of the parameters of the arterial tree are included in table 1.3.

The flow in the 55 arteries is assumed initially to be at rest. The density of blood was taken to be $\rho = 1.021 \times 10^3 Kg/m^3$. A periodic half sine wave is imposed as an input wave form at the ascending aorta (artery 1), which has the form

$$A(t) = 1 - 0.597\,\delta(t)\,H\left[\delta(t)\right]\ ; \quad \delta(t) = \sin(wt + 0.628) - 0.588$$

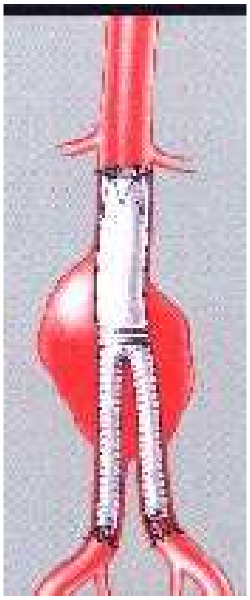

Figure 1.16: Endograft placement in the surgical treatment of abdominal aortic aneurysms.

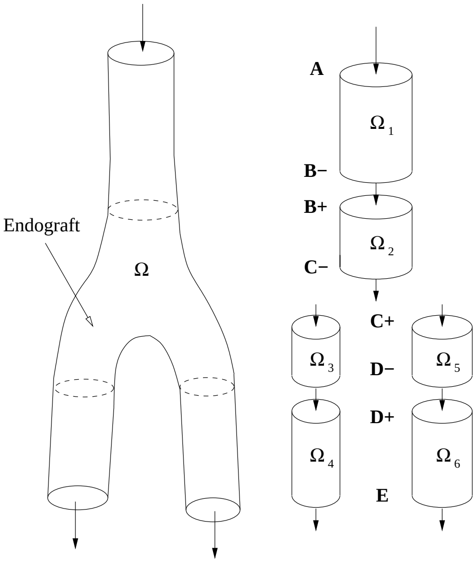

Figure 1.17: Modelling (left) and domain decomposition (right) of a bifurcation with an endograft.

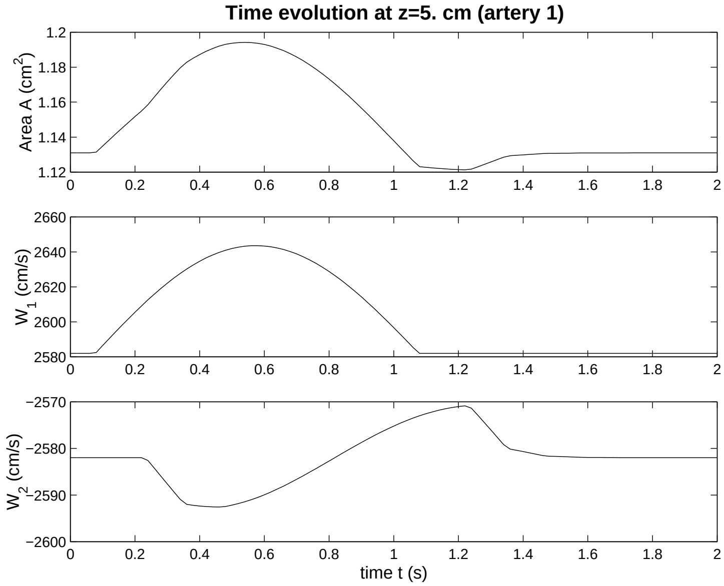

Figure 1.18: Bifurcation with endograft: time evolution for the area and the characteristic variables in the middle of domain Ω_1.

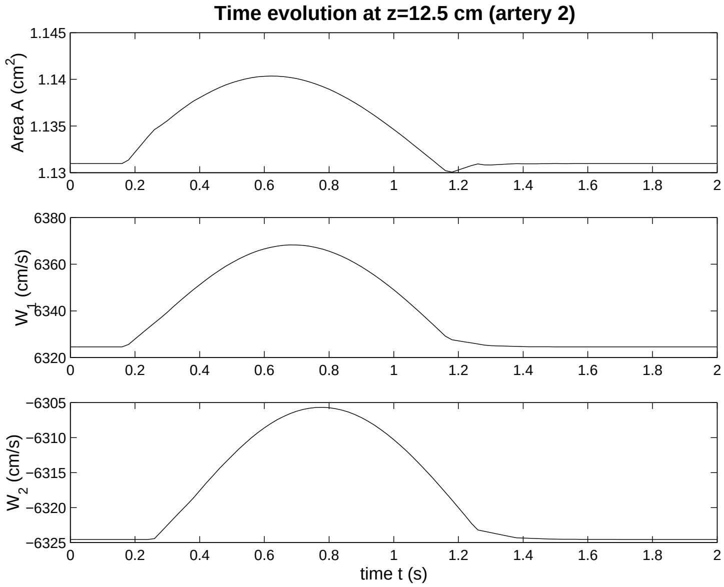

Figure 1.19: Bifurcation with endograft: time evolution for the area and the characteristic variables in the middle of domain Ω_2.

#	Artery	Length (cm)	Area (cm^2)	$\beta\ \left(kg\,s^{-2}\,cm^{-2}\right)$	R_t
1	Ascending Aorta	4.0	5.983	97	-
2	Aortic Arch I	2.0	5.147	87	-
3	Brachiocephalic	3.4	1.219	233	-
4	R. Subclavian I	3.4	0.562	423	-
5	R. Carotid	17.7	0.432	516	-
6	R. Vertebral	14.8	0.123	2590	0.906
7	R. Subclavian II	42.2	0.510	466	-
8	R. Radial	23.5	0.106	2866	0.82
9	R. Ulnar I	6.7	0.145	2246	-
10	R. Interosseous	7.9	0.031	12894	0.956
11	R. Ulnar II	17.1	0.133	2446	0.893
12	R. Internal Carotid	17.6	0.121	2644	0.784
13	R. External Carotid	17.7	0.121	2467	0.79
14	Aortic Arch II	3.9	3.142	130	-
15	L. Carotid	20.8	0.430	519	-
16	L. Internal Carotid	17.6	0.121	2644	0.784
17	L. External Carotid	17.7	0.121	2467	0.791
18	Thoracic Aorta I	5.2	3.142	124	-
19	L. Subclavian I	3.4	0.562	416	-
20	Vertebral	14.8	0.123	2590	0.906
21	L. Subclavian II	42.2	0.510	466	-
22	L. Radial	23.5	0.106	2866	0.821
23	L. Ulnar I	6.7	0.145	2246	-
24	L. Interosseous	7.9	0.031	12894	0.956
25	L. Ulnar II	17.1	0.133	2446	0.893
26	Intercostals	8.0	0.196	885	0.627
27	Thoracic Aorta II	10.4	3.017	117	-
28	Abdominal I	5.3	1.911	167	-
29	Celiac I	2.0	0.478	475	-
30	Celiac II	1.0	0.126	1805	-
31	Hepatic	6.6	0.152	1142	0.925
32	Gastric	7.1	0.102	1567	0.921
33	Splenic	6.3	0.238	806	0.93
34	Superior Mesenteric	5.9	0.430	569	0.934
35	Abdominal II	1.0	1.247	227	-
36	L. Renal	3.2	0.332	566	0.861
37	Abdominal III	1.0	1.021	278	-
38	R. Renal	3.2	0.159	1181	0.861
39	Abdominal IV	10.6	0.697	381	-
40	Inferior Mesenteric	5.0	0.080	1895	0.918
41	Abdominal V	1.0	0.578	399	-
42	R. Common Iliac	5.9	0.328	649	-
43	L. Common Iliac	5.8	0.328	649	-
44	L. External iliac	14.4	0.252	1493	-
45	L. Internal Iliac	5.0	0.181	3134	0.925
46	L. Femoral	44.3	0.139	2559	-
47	L. Deep Femoral	12.6	0.126	2652	0.885
48	L. Posterior Tibial	32.1	0.110	5808	0.724
49	L. Anterior Tibial	34.3	0.060	9243	0.716
50	R. External Iliac	14.5	0.252	1493	-
51	R. Internal Iliac	5.1	0.181	3134	0.925
52	R. Femoral	44.4	0.139	2559	-
53	R. Deep Femoral	12.7	0.126	2652	0.888
54	L. Posterior Tibial	32.2	0.110	5808	0.724
55	R. Anterior Tibial	34.4	0.060	9243	0.716

Table 1.3: Data used in the computational model of the 55 arteries.

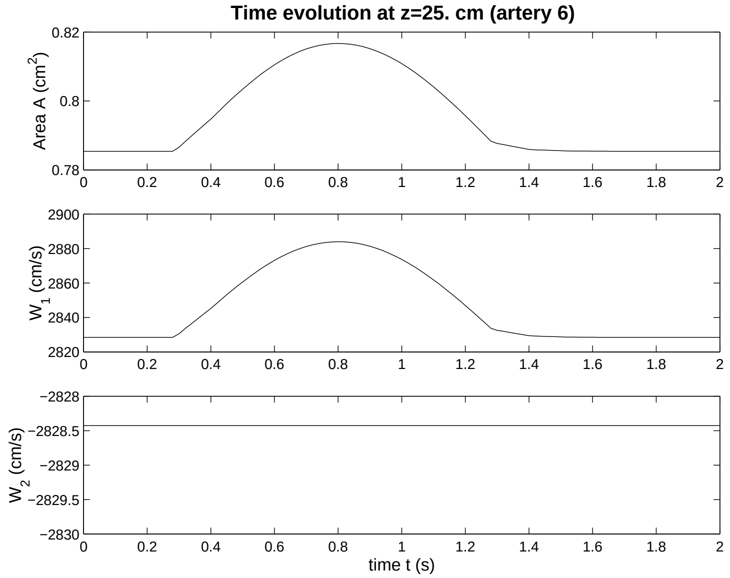

Figure 1.20: Bifurcation with endograft: time evolution for the area and the characteristic variables in the middle of domain Ω_6.

where $w = 2\pi/T$, $T = 1$ and $H(\delta)$ denotes the Heaviside step function. As explained in Sec. 1.3.3, to prevent spurious reflection the boundary condition has been imposed not directly but through the computation of an equivalent characteristic variable W_1. The graph of W_1 against time in figure 1.22 represents the form of the input wave. The upstream condition is either a non-reflecting condition or a *terminal resistance condition*. If at a terminal location W_1 and W_2 are the outgoing and the incoming characteristic variables, respectively, this condition states that $W_2 = -R_t W_1$, where the reflection coefficients R_t are listed in Table 1.3. The condition $R_t = 0$ would correspond to a non-reflecting condition, while $R_t = 1$ gives a perfect blockage since in that case $\overline{u} = 0$ at the terminal section.

Figures 1.22, 1.23 and 1.24 show eight time history graphs over a single cycle for three different arteries in the network: ascending aorta (artery 1), femoral artery (artery 46) and anterior tibial (artery 49). The history point was at the start of each artery. The results are shown for a free outflow (i.e. no terminal resistance) and with terminal resistance applied.

The inclusion of resistance to the terminal arteries increases the number of waves in the system due to forward travelling waves being reflected at the terminal vessels and introduces backward travelling waves, W_2, which are re-reflected at the bifurcations, hence a complex pattern of waves occurs in the network. Since the reflection coefficients are close to 1 in the terminal vessels W_2 is similar in magnitude to W_1 and will have a large effect on the wave forms, particularly in the end vessels, figure 1.24b. Introducing resistance has greatly changed the shapes of all the waves throughout the arterial network. The shape of the waves varies significantly from vessel to vessel whereas the shapes of the waves in the network with no terminal resistance were all very similar.

The inclusion of terminal resistance leads to more realistic results. Even though quantitative comparisons are difficult due to the lack of accurate values of the elastic properties of the arteries, the computed pressure (or area) waveforms show an increase in their peak value as we move down the system whilst the mean pressure slowly decreases. This behaviour is qualitatively sim-

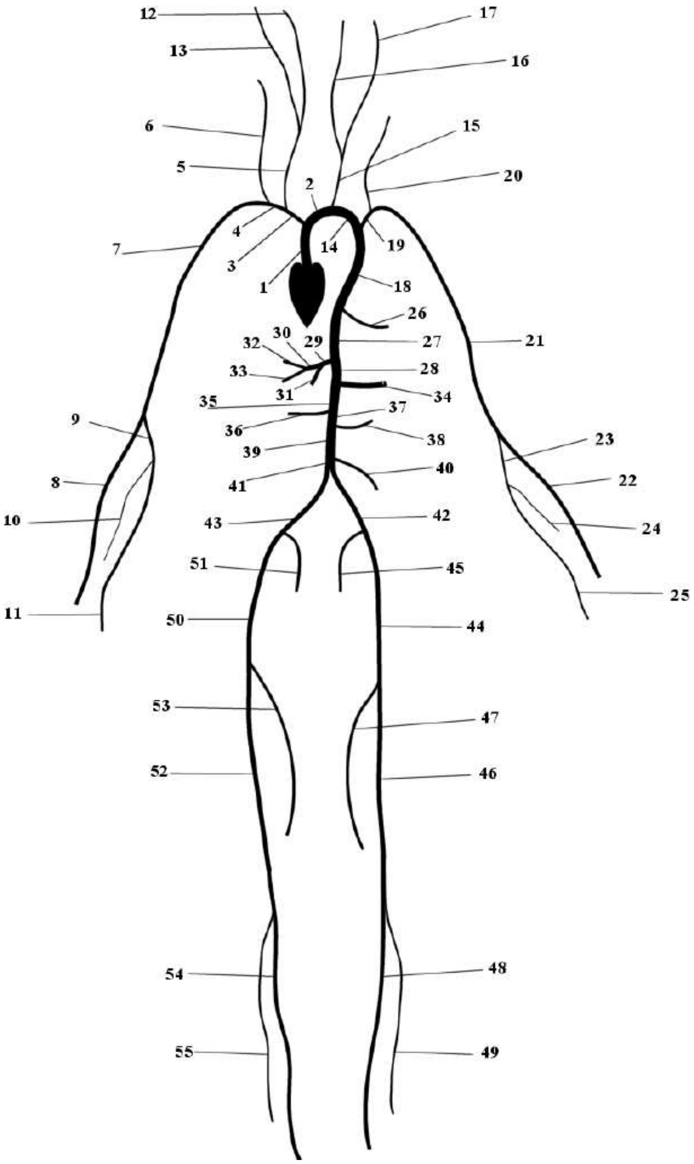

Figure 1.21: Connectivity of the 55 main arteries in the human arterial system.

ilar to that observed in the human arterial system, see for instance the in-vivo measuraments by Mills et al. (1970) reproduced in [20]. Terminal resistance also creates regions of flow reversal due to the reflected velocity wave and increases in area as a result of the re-enforcing effect of the reflected pressure wave. It has also produced a waveform which includes a diacrotic notch in the ascending aorta (artery 1). This is highlighted in the time evolution of the area depicted in figure 1.22b. This is also in agreement with in-vivo data [20].

1.5 More advanced models

In this last secton we present some preliminary results obtained using some advanced wall models following the technique autlined in Sec. 1.2.3. Here we adopt throughout relation (1.12) for the elastic contribution.

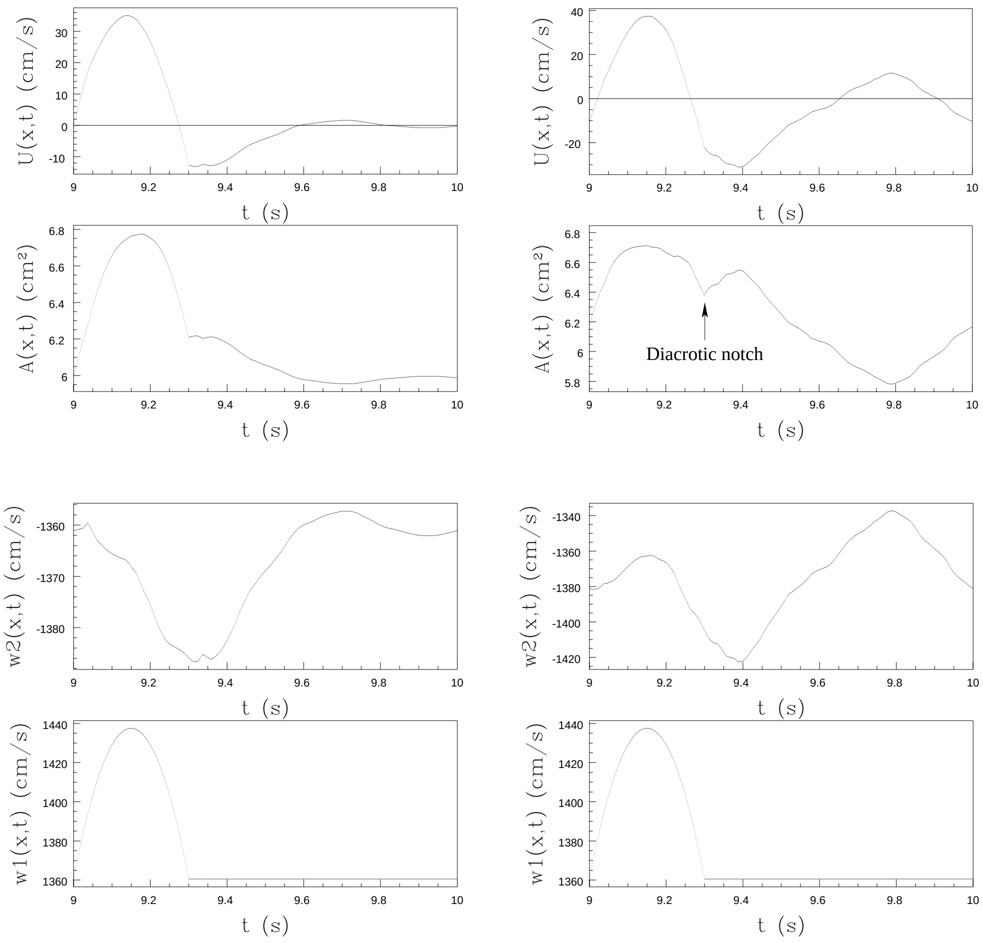

(a) (b)

Figure 1.22: Time histories at the ascending aorta (artery 1) considering: (a) no terminal resistance and (b) terminal resistance. Plots of velocity, area and the characteristic variables W_2 and W_1.

Therefore, the adopted model may be written as

$$m\frac{\partial^2 A}{\partial t^2} - \gamma\frac{\partial A}{\partial t} - a\frac{\partial^2}{\partial z^2}(\sqrt{A} - \sqrt{A_0}) + \beta_0\frac{\sqrt{A} - \sqrt{A_0}}{A_0} = P, \tag{1.59}$$

where we have taken $P_{ext} = 0$, A_0 and β_0 constant, while

$$m = \frac{\rho_w h_0}{2\sqrt{\pi}\sqrt{A_0}}, \quad \gamma = \frac{\tilde{\gamma}}{2\sqrt{\pi}\sqrt{A_0}}, \quad a = \frac{\tilde{a}}{\sqrt{\pi}}.$$

This model should be integrated with the fluid equations as already shown in order to retain the basic two-equations structure of the model. Since we assume that the dominant term is still the one related to the elestic properties of the vessel wall, we will adopt an operator splitting procedure for the numerical approximation, where the first operator is just the hyperbolic operator already analysed, which will be discretised again by the Taylor-Galerkin scheme.

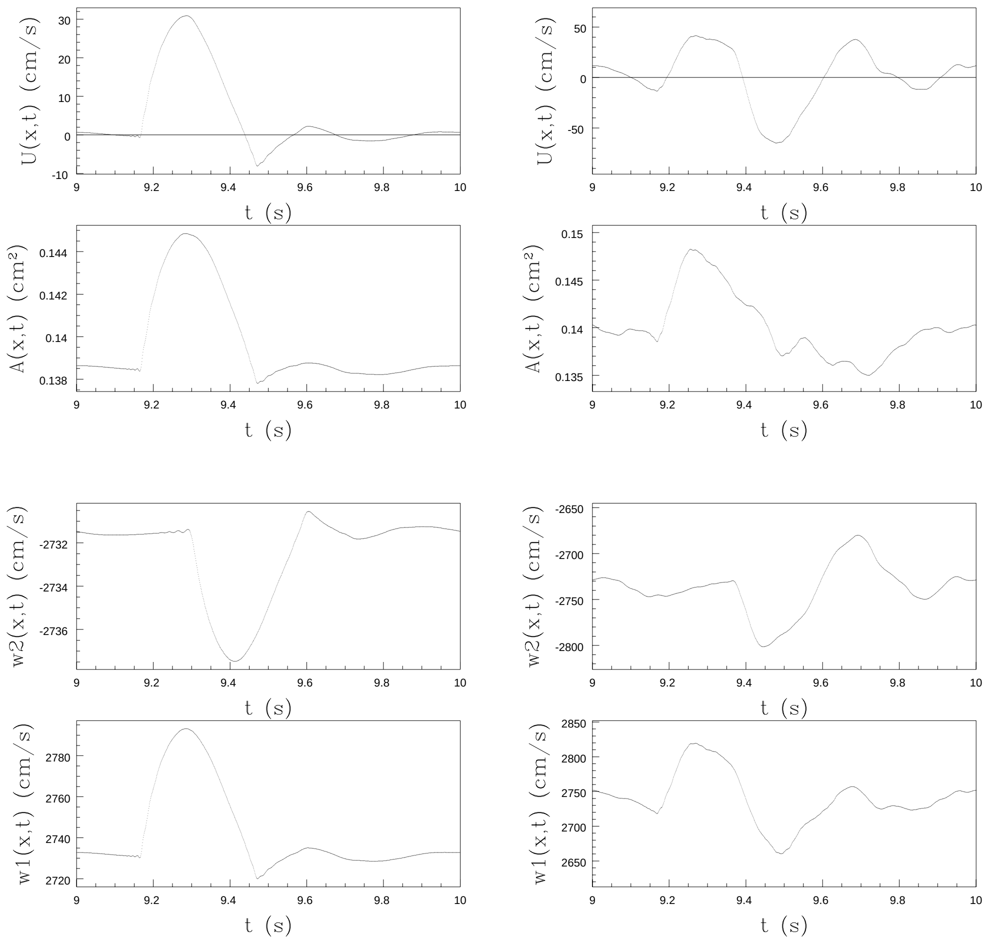

(a) (b)

Figure 1.23: Time histories at the femoral artery (artery 46) considering: (a) no terminal resistance and (b) terminal resistance. Plots of velocity, area and the characteristic variables W_2 and W_1.

We are mainly interested in identifying the effects of the extra terms on the vessel mechanics. The next sections will systematically analyse the effect of each of the added in turn.

1.5.1 Wall inertia term

The inertia term accounts for the wall mass and its acceleration: using physical arguments we can argue that it will be important only in case of large vessel mass and/or high frequency wave (big acceleration). In these cases we expect oscillations to occur at a frequency dependent on the wave length.

The contribution of this term in the momentum equation can be written, using the continuity equation, as

$$\frac{A}{\rho}\frac{\partial}{\partial z}\left(m\frac{\partial^2 A}{\partial t^2}\right) = -\frac{Am}{\rho}\frac{\partial^3 Q}{\partial t \partial z^2}. \tag{1.60}$$

System (1.16), augmented by the inertia term would then read

$$\begin{cases} \dfrac{\partial A}{\partial t} + \dfrac{\partial Q}{\partial z} = 0 \\ \dfrac{\partial Q}{\partial t} + \dfrac{\partial}{\partial z} F_2(A,Q) - \dfrac{Am}{\rho} \dfrac{\partial^3 Q}{\partial t \partial z^2} = B_2(A,Q), \end{cases} \tag{1.61}$$

where $F_2(A,Q)$ and $B_2(A,Q)$ denote the second component of the flux $\mathbf{F}$ and of the source term $\mathbf{B}$, respectively.

The differential system (1.61) may be written in an equivalent way by splitting the flow rate $Q = \widehat{Q} + \widetilde{Q}$, where $\widehat{Q}$ and $\widetilde{Q}$ are implicitly defined through the set of equations

$$\begin{aligned} &\frac{\partial A}{\partial t} + \frac{\partial Q}{\partial z} = 0 \\ &\frac{\partial \widehat{Q}}{\partial t} + \frac{\partial}{\partial z} F_2(A,Q) = S(A,Q) \\ &\frac{\partial \widetilde{Q}}{\partial t} - \frac{Am}{\rho} \frac{\partial^3 Q}{\partial t \partial z^2} = 0. \end{aligned} \tag{1.62}$$

This allows us to devise the following operator splitting strategy. On each time interval $[t^n, t^{n+1}]$, $n \geq 0$, system $(1.62)_{1,2}$ by the Taylor-Galerkin scheme described in Sec. 1.3.1 and we correct the mass flux by employing Eq. $(1.62)_3$. More precisely, the adopted finite element formulation for the latter equation reads: given A_h^{n+1} and $\widehat{Q}_h^{n+1}$, find $\widetilde{Q}_h \in V_h^0$ such that

$$\left(\frac{1}{A_h^{n+1}} \widetilde{Q}_h^{n+1}, \psi_h \right) + \frac{m}{\rho} \left(\frac{\partial \widetilde{Q}_h^{n+1}}{\partial z}, \frac{\partial \psi_h}{\partial z} \right) = \frac{m}{\rho} \left(\frac{\partial \widehat{Q}_h^{n+1}}{\partial z}, \frac{\partial \psi_h}{\partial z} \right), \quad \forall \psi_h \in V_h^0.$$

This corresponds to having imposed a homogeneous boundary condition for the correction term $\widetilde{Q}$.

An alternative approach can be found in [1].

In the following numerical experiments we have set $\rho = 1\ gr/cm^3$, ν =0.035 m^2/s, R_0 has been taken constant and equal to 0.5 cm, h_0 =0.05 cm and $E = 3\ 10^6\ dyne/cm^2$. The simulations have been carried out using a time step Δt =1 10^{-5} s.

Figure 1.25 shows the results for a realistic test problem where the vessel wall density is set to $\rho_w = 1 gr/cm^3$ and we take a wave of length 32 cm (picture on the top-left of Figure 1.25). It may be noted that the inertia term yields a relative variation in the vessel area of the order of 10^{-3}. We may also note the high frequency oscillations induced by the inertia term. Clearly, in real conditions these oscillations are damped out by the viscoelastic term. As high frequency are solicited, the variation in the flow rate behaviour is more important. We also report some numerical experiments carried out in the same geometrical configuration using a pressure wave pulse of length 4. cm (pictures on the top-left of Figures 1.26 and 1.27) and a wall density of 1 and 100 gr/cm^3, respectively. These tests have been carried out to enhance the inertia effects and are reported in Figures 1.26 and 1.27. Note, in particular, that the value 100 gr/cm^3 is unrealistic in physiological conditions. These tests show that the inertia term play a major role when the mass or the vessel acceleration are important.

A qualitative comparison with the result obtained by a two dimensional fluid-structure interaction code has been carried out only for the test case of Figure 1.26; a good agreement has been found.

1.5.2 Viscoelastic term

In the generalised string model there are two possible viscous effects. Here, we have considered only the term in the form $\tilde{\gamma}\frac{\partial \eta}{\partial t}$, since the term $(\tilde{c}\frac{\partial^3 \eta}{\partial t \partial z^2})$ will produce a fourth order spatial derivative in the momentum equation that makes its numerical treatment more difficult.

After introducing the term in the momentum equation and using the continuity equation, the modified system reads

$$\begin{cases} \dfrac{\partial A}{\partial t} + \dfrac{\partial Q}{\partial z} = 0 \\ \dfrac{\partial Q}{\partial t} + \dfrac{\partial F_2(A,Q)}{\partial z} - \dfrac{A\gamma}{\rho}\dfrac{\partial^2 Q}{\partial z^2} = B_2(A,Q). \end{cases} \tag{1.63}$$

This system has been solve by an operator splitting procedure similar to that introduced before and an implicit Euler discretisation for the correction term $\widetilde{Q}$.

Tests have been carried out to investigate the effects of the viscoelastic term. We set $\rho = 1\ gr/cm^3$, ν =0.035 m^2/s, $R_0 = 0.5\ cm$, h_0 =0.05 cm and $E = 3\ 10^6\ dyne/cm^2$. The simulations have been carried out with a time step Δt =1 $10^{-4}\ s$ and a space discretization $\Delta x = 0.1\ cm$.
In Figure 1.28 we report the results of a short half sine pressure wave (period 0.015 s, amplitude 20000 $dyne/cm^2$) and a longer one (period 0.3 s, amplitude 20000 $dyne/cm^2$) imposed at inlet. We should note that the solutions with (γ = 3 $gr/cm^3 s$) and without the viscoelastic term have a relative difference in the area of less than 1 %.

1.5.3 Longitudinal elasticity term

Experimental findings show that vessel walls are longitudinally pre-stressed [12]. This originates the second z derivative term in the generalised string model [24]. Accounting for this term by using the techniques previously illustrated would produce a modified system of the type

$$\begin{cases} \dfrac{\partial A}{\partial t} + \dfrac{\partial Q}{\partial z} = 0 \\ \dfrac{\partial Q}{\partial t} + \dfrac{\partial F_2(A,Q)}{\partial z} - \dfrac{Aa}{\rho}\dfrac{\partial^3}{\partial z^3}\left(\sqrt{A} - \sqrt{A_0}\right) = B_2(A,Q). \end{cases} \tag{1.64}$$

Solving this system by an operator splitting technique like that presented in Sec. 1.5.1 would require the solution of a differential equation for the correction term $\widetilde{Q}$ given by

$$\frac{\partial \widetilde{Q}}{\partial t} - \frac{Aa}{\rho}\frac{\partial^3}{\partial z^3}\left(\sqrt{A} - \sqrt{A_0}\right) = 0. \tag{1.65}$$

The correction $\widetilde{Q}_h^{n+1} \in V_h^0$ has been computed by a collocation procedure and using a finite difference approximation for the third derivative term of A_h^{n+1} (which is computed in the first step of the operator splitting procedure).

The effect of the longitudinal pre-stress is more important when strong area gradients are present. To analyse thus, we considered a stented artery of total length $L = 15\ cm$ with a stent of length 5 cm placed in the middle. The vessel has a radius $R_0 = 0.5$ cm and $h_0 = 0.05$ cm. The Young's modulus is $E = 3$ 10^6 $dyne/cm^2$ for the healthy portion of the artery and $E_s = 30$ 10^6 $dyne/cm^2$ for the stented part. At $z = 5$ cm and $z = 10$ cm the Young's modulus has been regularised by a fifth-order function (as done in [10]); the length of the variation zone was 0.1 cm. The coefficient $\tilde{a}$ was set to 10^4 gr/s^2. Finally, we have taken $\rho = 1$ gr/cm^3, $\nu = 0.035$ cm^2/s and $\alpha = 1$.

At inlet we imposed a half sine pressure wave of period $T = 0.4$ s and amplitude of 20000 $dyne/cm^2$.

Figure 1.29 shows that, without the longitudinal elasticity term (solution represented by a continuous line), there is an abrupt variation in the area. Clearly this solution is not physiological as we cannot have, in the limit, a discontinuous area. Taking in account the effect of the longitudinal elasticity term, that ”discontinuity”is smoothed with a jump between the values of the area on the left and the right of the same magnitude.

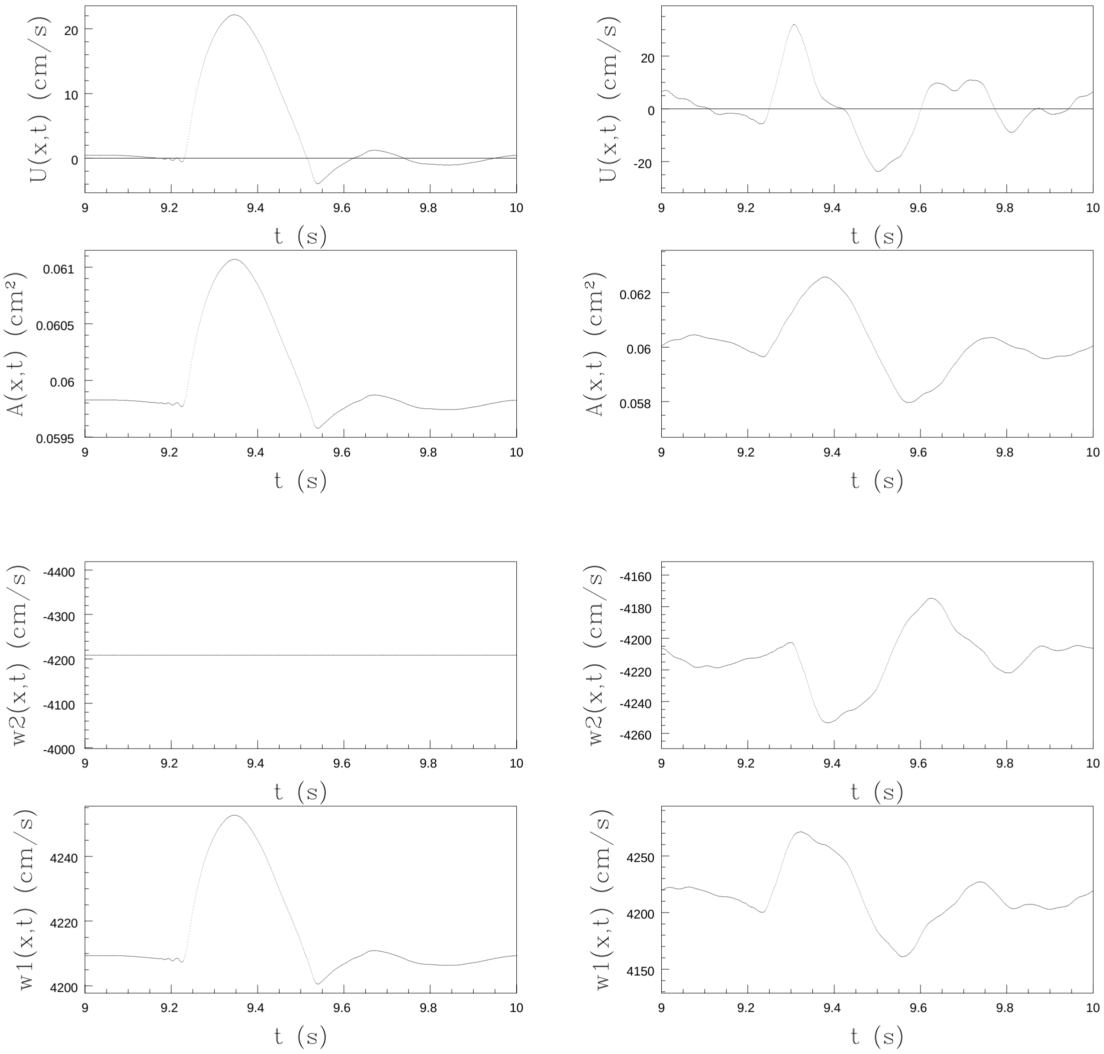

(a) (b)

Figure 1.24: Anterior tibial artery (terminal artery 49). Time history comparison of waves forms with: (a) no terminal resistance and (b) terminal resistance. Plots of velocity, area and the characteristic variables W_2 and W_1.

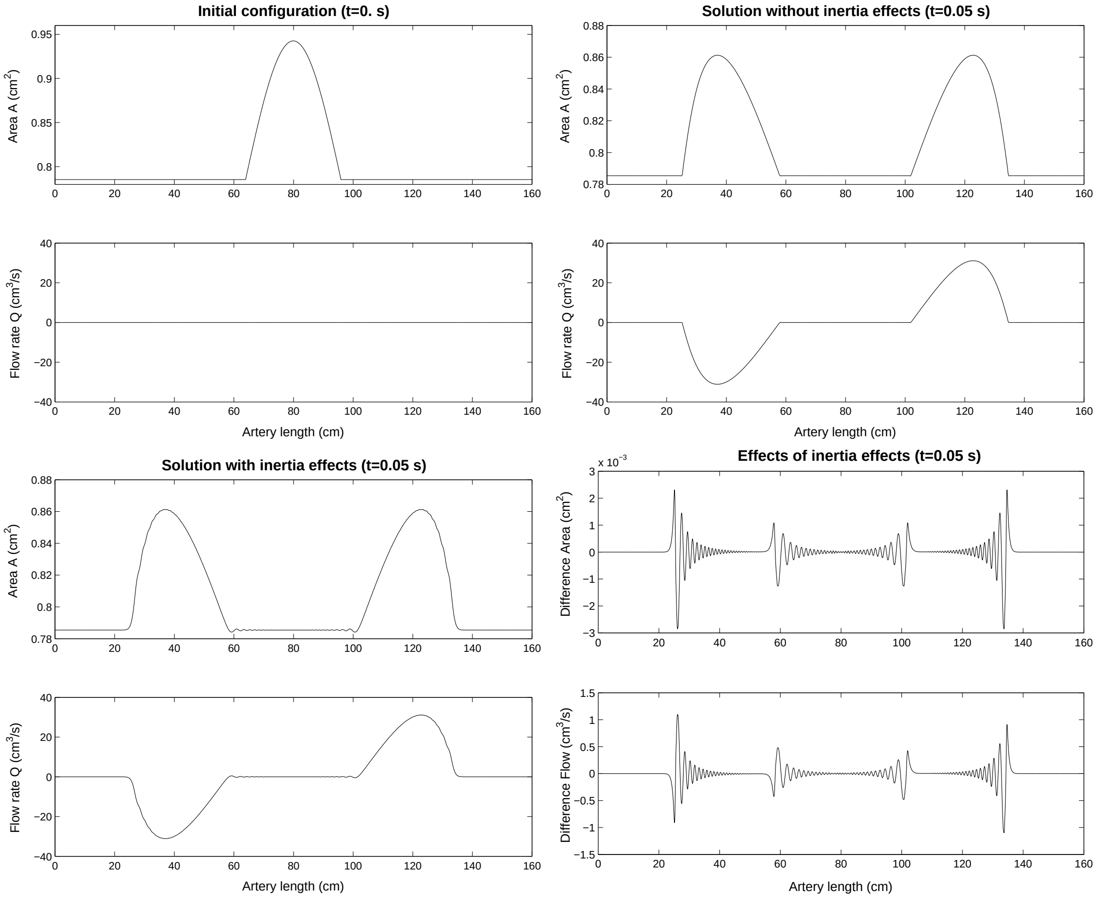

Figure 1.25: Inertia effects on the solution; on the top-left the initial configuration is reported: a half sine wave of length 35 cm. The solutions without inertia term (top-right), with inertia term (bottom-left) and the difference between the two (bottom-right) for a fixed time (0.05 s) are reported too.

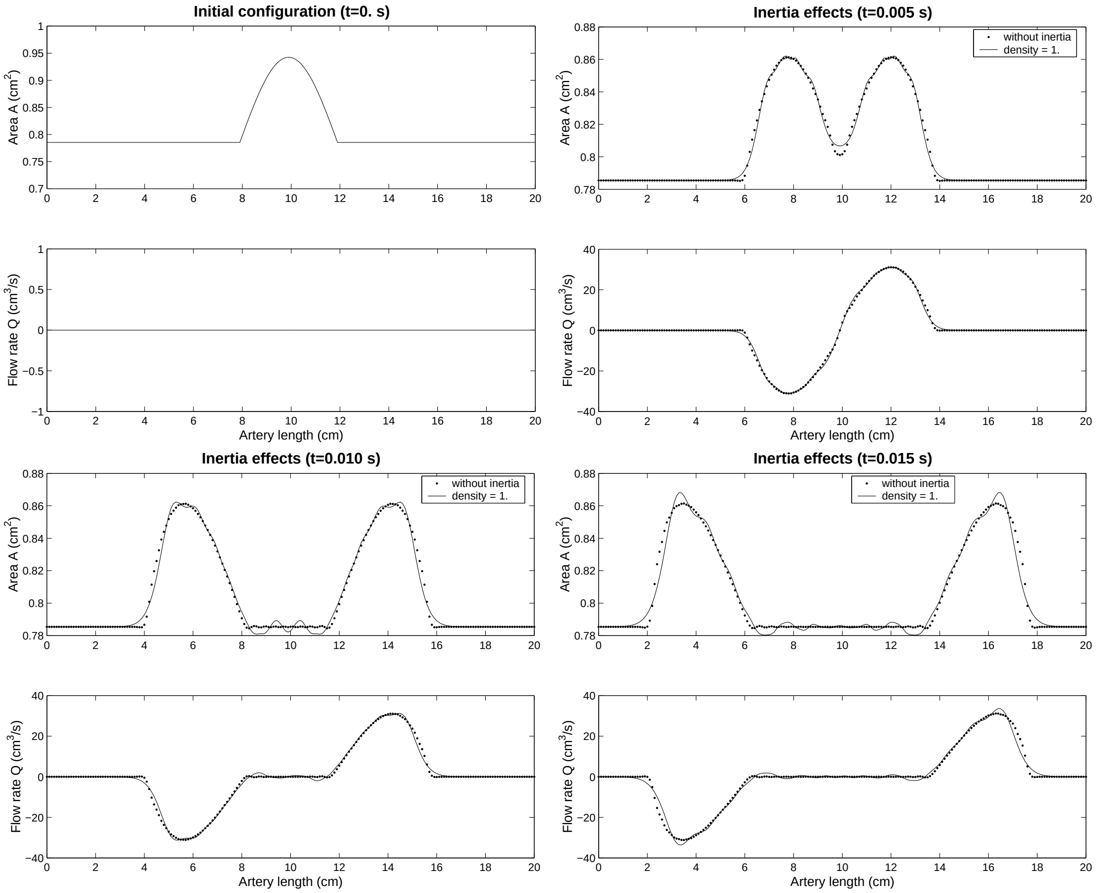

Figure 1.26: Inertia effects on the solution; on the top-left the initial configuration is reported: a half sine wave of length 4 cm. The solutions without inertia term (dotted line) and with inertia term, wall density set to 1 gr/cm^3, (continuous line) for different time steps are also reported.

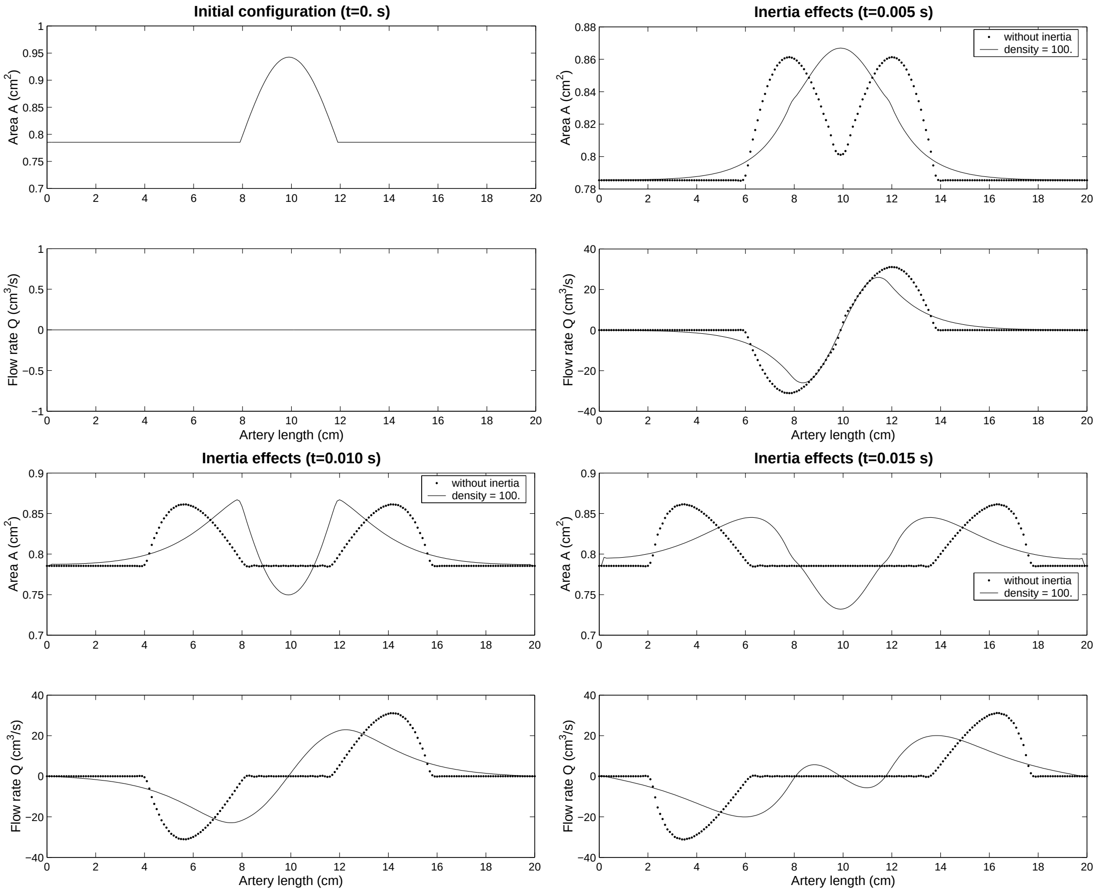

Figure 1.27: Inertia effects on the solution; on the top-left the initial configuration is reported: a half sine wave of length 4 cm. The solutions without inertia term (dotted line) and with inertia term, wall density set to 100 gr/cm^3, (continuous line) for different time steps are also reported.

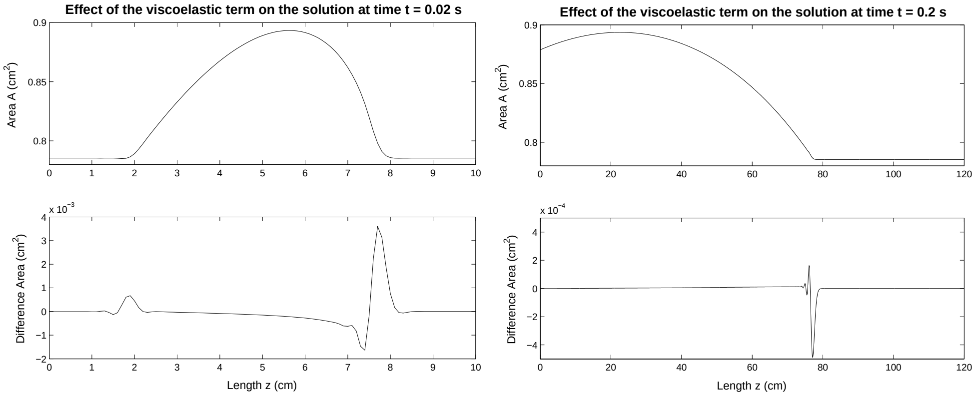

Figure 1.28: Viscoelasticity effects on the solution at two given time steps: solution of the problem without viscoelasticity term (top) and difference between the solutions with and without viscoelastic term (bottom).

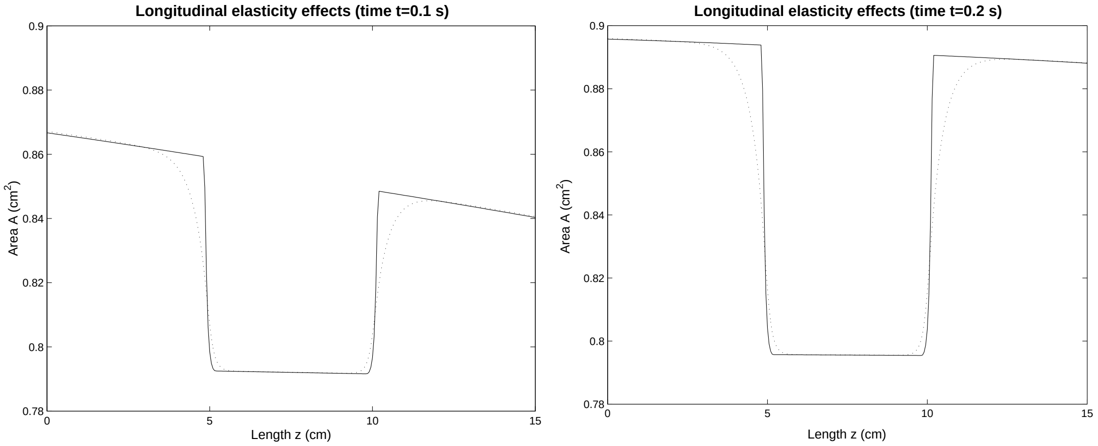

Figure 1.29: Longitudinal elasticity effects on the solution at two different time steps (the dotted line represents the solution with the longitudinal pre-stress term).

Bibliography

[1] D. Ambrosi and L. Quartapelle. A Taylor-Galerkin method for simulating nonlinear dispersive water waves. *J. Comput. Phys.*, 146(2):546–569, 1998.

[2] A.C.L. Barnard, W.A. Hunt, W.P. Timlake, and E. Varley. A theory of fluid flow in compliant tubes. *Biophys. J.*, 6:717–724, 1966.

[3] R. Botnar, G. Rappitsch, M.B. Scheidegger, D. Liepsch, K. Perktold, and P. Boesiger. Hemodynamics in the carotid artery bifurcation: A comparison between numerical simulations and in-vitro measurements. *J. of Biomech.*, 33:137–144, 2000.

[4] K. Boukir, Y. Maday, and B. Métivet. A high order characteristics method for the incompressible Navier-Stokes equations. *Comput. Methods Appl. Mech. Engrg.*, 116(1-4):211–218, 1994. ICOSAHOM'92 (Montpellier, 1992).

[5] S. Canic. Blood flow through compliant vessels after endovascular repair: wall deformations induced by the discontinuous wall properties. *Computing and Visualisation in Science*, 4(3):147–155, 2002.

[6] S. Canic and E.H. Kim. Mathematical analysis of the quasilinear effects in a hyperbolic model of blood flow through compliant axi-symmetric vessels. *Mathematical Methods in Applied Sciences*, 2002. (to appear).

[7] J. Donea, S. Giuliani, H. Laval, and L. Quartapelle. Time-accurate solutions of advection-diffusion problems by finite elements. *Comp. Meth. Appl. Mech. Engng.*, 45:123–145, 1984.

[8] L. Formaggia, J.-F. Gerbeau, F. Nobile, and A. Quarteroni. On the coupling of 3D and 1D Navier-Stokes equations for flow problems in compliant vessels. *Comp. Methods in Appl. Mech. Engng.*, 191:561–582, 2001.

[9] L. Formaggia, D. Lamponi, and A. Quarteroni. One dimensional models for blood flow in arteries. Rapport de Recherche d'Analyse Numerique 03/2002, IMA-MOCS, EPFL, 2002. sumbitted to Journal of Engineering Mathematics.

[10] L. Formaggia, F. Nobile, and A. Quarteroni. A one dimensional model for blood flow: application to vascular prosthesis. In I. Babuska, T. Miyoshi, and P.G. Ciarlet, editors, *Mathematical Modeling and Numerical Simulation in Continuum Mechanics*, volume 19 of *Lecture Notes in Computational Science and Engineering*, pages 137–153, Berlin, 2002. Springer-Verlag.

[11] L. Formaggia, F. Nobile, A. Quarteroni, and A. Veneziani. Multiscale modelling of the circulatory system: a preliminary analysis. *Computing and Visualisation in Science*, 2:75–83, 1999.

[12] Y.C. Fung. *Biomechanics: Mechanical Properties of Living Tissues.* Springer-Verlag, New York, 1993.

[13] E. Godlewski and P.-A. Raviart. *Numerical Approximation of Hyperbolic Systems of Conservation Laws*, volume 118 of *Applied Mathematical Sciences*. Springer, New York, 1996.

[14] K. Hayashi, K. Handa, S. Nagasawa, and A. Okumura. Stiffness and elastic behaviour of human intracranial and extracranial arteries. *J. Biomech.*, 13:175–184, 1980.

[15] G.W. Hedstrom. Nonreflecting boundary conditions for nonlinear hyperbolic systems. *J. Comp. Physics*, 30:222–237, 1979.

[16] T.H. Hughes, C. Taylor, and C. Zarins. Finite element modeling of blood flow in arteries. *Comp. Meth. Appl. Mech. Eng.*, 158:155–196, 1998.

[17] G.L. Langewouters, K.H. Wesseling, and W.J.A. Goedhard. The elastic properties of 45 human thoracic and 20 abdominal aortas *in vitro* and the parameters of a new model. *J. Biomech.*, 17:425–435, 1984.

[18] P.D. Lax. *Hyperbolic Systems of Conservation Laws and the Mathematical Theory of Shock Waves*. SIAM, Philadelphia, Pa., 1973. Conference Series in Applied Mathematics, No. 11.

[19] R.J. LeVeque. *Numerical Methods for Conservation Laws*. Birkhauser, Basel, 1990.

[20] W. W. Nichols and M. F. O'Rourke. *McDonald's blood flow in arteries*. Edward Arnold, third edition, 1990.

[21] M. Olufsen. *Modeling the arterial system with reference to an anestesia simulator*. PhD thesis, Rotskilde Univ., 1998. Tekst 345.

[22] M. Olufsen and J. Ottesen. A fluid dynamical model of the aorta with bifurcations. Tekst 297, Rotskilde Univ., 1995.

[23] L. Quartapelle. *Numerical solution of the incompressible Navier-Stokes equations*. Birkhäuser Verlag, Basel, 1993.

[24] A. Quarteroni and L. Formaggia. *Modelling of Living Systems*, chapter Mathematical Modelling and Numerical Simulation of the Cardiovascualr System. Handbook of Numerical Analysis. Elsevier Science, 2003. to appear.

[25] A. Quarteroni, M. Tuveri, and A. Veneziani. Computational vascular fluid dynamics: Problems, models and methods. *Computing and Visualisation in Science*, 2:163–197, 2000.

[26] A. Quarteroni and A. Valli. *Numerical Approximation of Partial Differential Equations*. Springer-Verlag, Berlin, 1994.

[27] A. Quarteroni and A. Valli. *Domain Decomposition Methods for Partial Differential Equations*. The Clarendon Press Oxford University Press, New York, 1999. Oxford Science Publications.

[28] V. Rideout and D. Dick. Difference-differential equations for fluid flow in distensible tubes. *IEEE Trans. Biomed. Eng.*, BME-14(3):171–177, 1967.

[29] S.J. Sherwin, L. Formaggia, J. Peiró, and V. Franke. Computational modelling of 1D blood flow with variable mechanical properties and its application to the simulation of wave propagation in the human arterial system. *Int. J. Numer. Meth. Fluids*, 2003. (to appear).

[30] S.J. Sherwin, O. Shah, D.J. Doorly, J. Peiró, Y. Papaharilaou, N. Watkins, C.G. Caro, and C.L. Dumoulin. The inflence of out-of-plane geometry on the flow within a distal end-to-side anastomosis. *ASME J. Biomech.*, 122:1–10, 2000.

[31] N.P. Smith, A.J. Pullan, and P.J. Hunter. An anatomically based model of coronary blood flow and myocardial mechanics. *SIAM J. Appl. Math.*, 62(3):990–1018.

[32] J.C. Stettler, P. Niederer, and M. Anliker. Theoretical analysis of arterial hemodynamics including the influence of bifurcations, part i: Mathematical model and prediction of normal pulse patterns. *Annals of Biomedical Engineering*, 9:145–164, 1981.

[33] K.W. Thompson. Time dependent boundary conditions for hyperbolic systems. *J. Comp. Physics*, 68:1–24, 1987.

[34] N. Westerhof, F. Bosman, C.J. De Vries, and A. Noordergraaf. Analog studies of the human systemic arterial tree. *J. Biomech.*, 2:121–143, 1969.

Chapter 2

Geometrical multiscale models of the cardiovascular system: from lumped parameters to 3D simulations

2.1 Why do we need multiscale models?

One of the major difficulties encountered when wishing to model in an accurate way the human cardiovascular system is that it is in fact formed by a closed network with a high level of inter-dependency. The flow dynamics of the blood in a specific vascular district (*local haemodynamics*) is strictly related to the global, systemic dynamics. For instance, the distribution of blood flow inside the various vascular districts, which is a systemic feature, influences for the blood dynamics in each district (local feature). Besides, the study of local flow feature is important since pathologies like the formation of local intimal thickening or plaques is strongly influenced by the local hemodynamics (see e.g. [48]). On the other hand, *local* alteration in vascular lumen induces a *global redistribution of the blood flow*, giving rise to compensatory mechanisms that, at some extents, can ensure a sufficient blood flow in the districts downstream the stenosis. Neglecting such effect provides only a partial information.

For instance, in [2], it is shown that even a strong reduction in the vascular lumen in a carotid bifurcation does not mean a relevant reduction of the blood supply to the brain. In [44] experimental results are explained by using a numerical model for the cerebral circulation. The authors simulate an occlusion of the Internal Carotid Artery (ICA) and compute, by means of classical 1D models for the circulation, the outcoming flow from the circle of Willis into the Middle Cerebral Artery (MCA). Both experimental and numerical results clearly show that, unless other vessels of the Willis circle are occluded, the blood supply flowing towards the cerebral system is not significantly reduced. This is due to the presence of compensatory systemic mechanisms that increases the blood flow in other incoming vessels.[1] (see Figs. 2.1, 2.2, 2.3).

This reciprocal influence between local and systemic hemodynamics has led to the concept of *geometrical "multiscale"* modelling of the circulation

---

[1] The compensation in [44] is essentially driven by mechanical effects. Other biochemical mechanisms such the so-called *autoregulation*, i.e. an increase of the vessel radii induced by a biochemical signal in presence of a stenosis is not considered here. This biochemical feedback, in fact, makes the downstream flow reduction even more less relevant and the overall system more reliable.

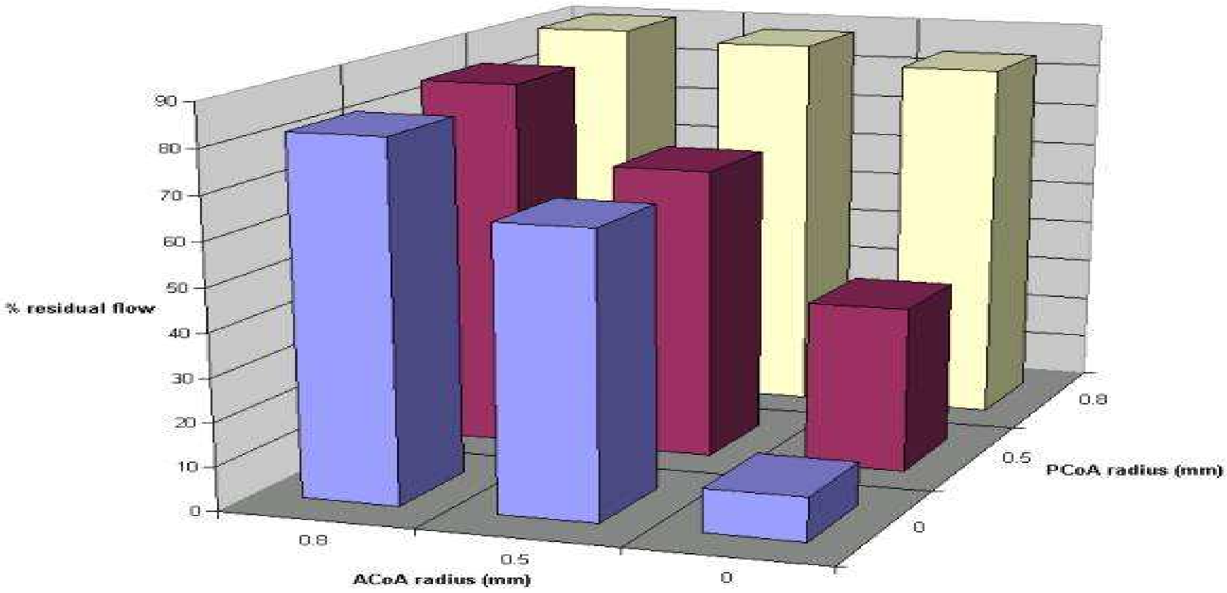

Figure 2.1: Flow reduction in the Middle Cerebral Artery (MCA) when an occlusion in an Internal Carotid Artery (ICA) is simulated. If the Anterior Communicating Artery (ACoA) and the Posterior Communicating Artery (PCoA) are physiologically perfused (radius 0.8 mm), the flow reduction is small. Flow reduction becomes significant if one or both the Communicating arteries are (partially or totally) occluded too.

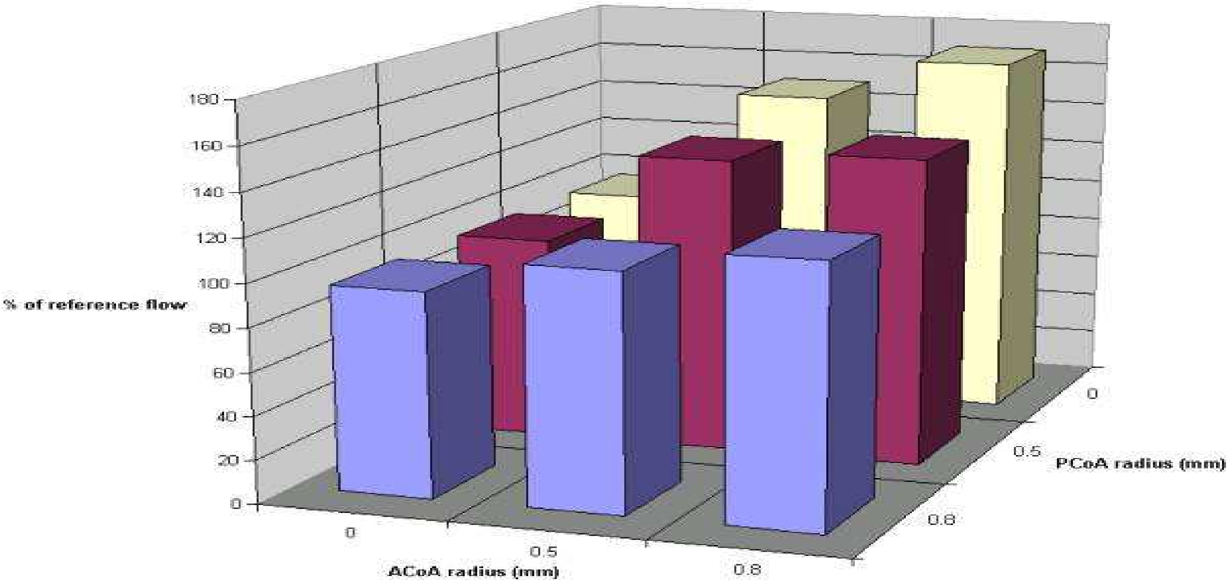

Figure 2.2: Flow increment in the health(=not occluded) ICA when the other is occluded under the same conditions simulated in Fig. 2.1. Pictures taken from [44].

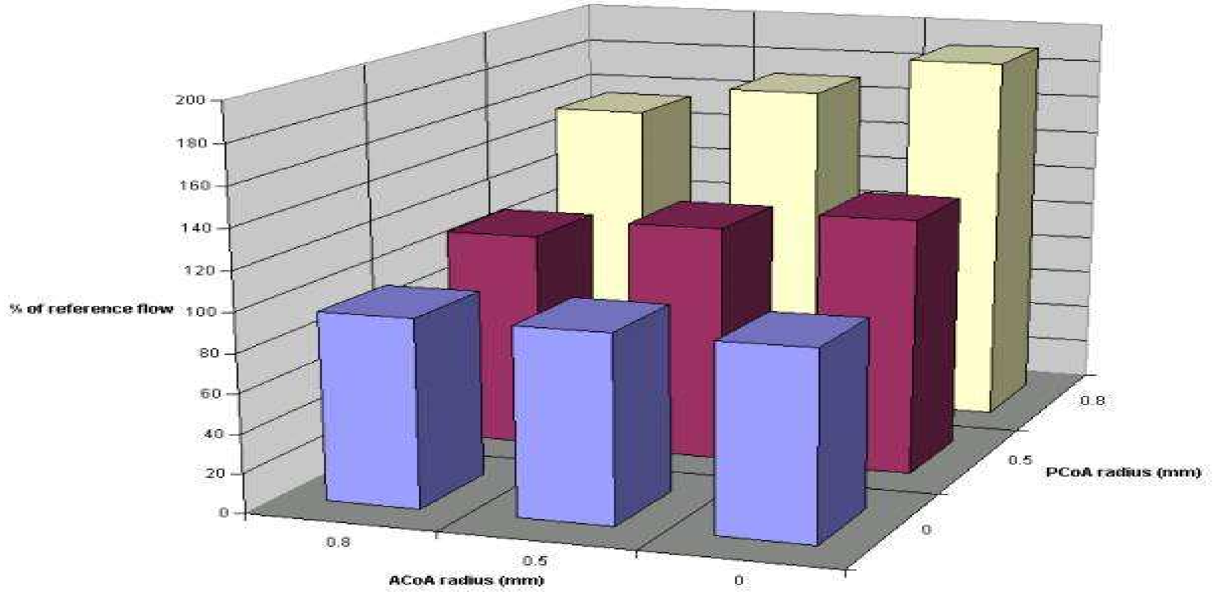

Figure 2.3: Flow increment in the Vertebral Artery (VA) when one ICA is occluded under the same conditions simulated in Fig. 2.1.

Remark 2.1. *The term "multiscale" is often used with different meanings in different fields of mathematical and numerical modelling. (e.g. wavelets, turbulence modelling etc.).*

Indeed, even in the present context we could consider other "multiscale" phenomena. For instance with respect to time, as the characteristic period driving the cardiovascular system is the heart beat, about 0.8 *s, while related phenomena, like atherosclerotic plaques formation, develop over months or years. The coupling of these different time scales is another challenge of numerical cardiovascular modelling.*

Therefore, in order to avoid ambiguities, we indicate by the term geometrical *our present multiscale perspective. In fact, this feature is common to all many problems involving modeling subregions of a larger and complex system, such as hydraulic or electric networks. Examples are the simulation of exhaust systems of Diesel engines (see [6]), and the design of electric circuits (see [1]).*

A multiscale perspective is relevant even when one is interested just on the description of the local flow. Indeed, the formulation of a mathematical well posed problem requires the specification of boundary data (see Fig. 2.4). The vascular walls are physical boundaries and the correct conditions are suggested by physical assumptions such as the continuity of the velocity field. However, artificial boundaries (e.g. Γ_{in}, Γ_{out1} and Γ_{out2} in Fig. 2.4) have to be introduced to delimit the vascular district at hand. In fact, they are the interface between the district under consideration and the remainder of the circulatory system. Boundary conditions on such boundaries are critical and, in fact, influenced by the "multiscale" nature of the circulation. Whenever such data are not available from specific (and accurate!) measurements, a proper boundary condition would require a mathematical description of the action of the circulatory system on the vascular district to hand. Clearly, since it is not affordable to describe the whole circulatory system at the same level of detail, this mathematical description relies on simpler models.

While the local model will be typically based on the solution of the incompressible Navier-Stokes possibly coupled with the dynamics of the vessel walls (see e.g. [28], [9]), the systemic

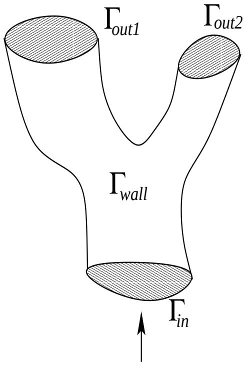

Figure 2.4: Schematic representation of a carotid bifurcation. We need to find suitable data for the “artificial” boundary sections Γ_{in}, Γ_{out1} and Γ_{out2}.

model will be based on *1D models*, such the ones introduces in [10], or, (more frequently) by *lumped parameters* models based on the solution of a system of ordinary differential equation (in time) for the average mass flow and pressure in the different compartments forming the cardiovascular system.

The lumped parameters models are often based on the analogy between hydraulic and electric networks. Indeed one of the first (if not the first) simulator of the cardiovascular system was analogic [45] and based on an actual electric network. Other very rough (and however popular) lumped models for the circulation are the Windkessel (see [22]) and its improved version, called Westkessel. They also admit a representation by an electric circuit (see Fig. 2.5).

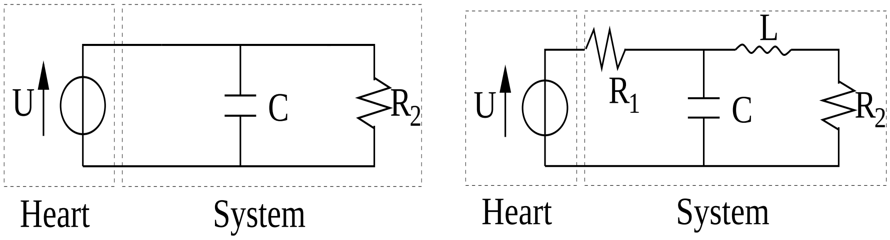

Figure 2.5: Representation of the classical Windkessel model and the modification introduced by N. Westerhof, (Westkessel model), based on electric circuits

Besides their intrinsic relevance, these models are of great interest in our multiscale perspective. Indeed, they provide a systemic description of the main phenomena related to the circulation (such as the compensatory mechanisms mentioned above) at a low computational cost. They may thus be coupled with an accurate (but local) description of a vascular district of interest.

The mathematical and numerical issues related to this coupling are nontrivial. The different level of detail of the different models is reflected by different mathematical features. Navier-Stokes equations are a system of non-linear partial differential equations which are essentially parabolic for the velocity, while the 1D models are (mainly) based on hyperbolic partial differential equations, and the lumped parameter models do not feature a spatial dependency and are described by means of ordinary differential equations in the time variable (for this reason, they are also called "0D models"). A particular care has therefore to be taken in managing the interfaces between models in order to have mathematically well posed problems and to guarantee accurate numerical results.

In these notes, we will start with a short introduction of the lumped parameter description of the circulation and its basic mathematical features (Sect. 2). Then we will focus our attention on the coupling between different models. We will consider first some basic issues for the numerical treatment of the Navier-Stokes problem coupled with 1D and 0D models (Sect. 3). Then, we will tackle multiscale models both from the mathematical and the numerical viewpoint. We will address both the 3D-0D and the 3D-1D models coupling (Sect. 4). Numerical results are presented in Sect. 5 to show the effectiveness of the multiscale approach not only for academic test cases but also in simulations of real medical interest.

2.2 Lumped parameters models for the circulation

Many biological systems feature complex mechanisms given by the interaction of elementary components. A possible and effective description of such systems is based on the identification of these elementary components, often called *compartments* (see e.g. [4]) and their mutual interaction. In the case of cardiovascular modeling, we could say that *a compartment is a part of the system which is reasonable to consider as a whole, according to the needed accuracy in the description of circulation. The behavior of the blood in a compartment is described in terms of quantities (typically the flow rate and pressure) "averaged" (in space) over the whole compartment.* The mathematical description of this system can be therefore provided by:

1. the description of each compartments;
2. the description of the interactions among the compartments.

The number of the compartments involved depends on the level of accuracy requested to the model. For instance, if one wants to investigate heart failures with the purpose of increasing the cardiac function without a significant (and dangerous) increment of the systolic pressure, a two-compartments description of the cardiovascular system can be enough, featuring the left ventricle and the systemic circulation respectively (see [22], Chap. 13). The *Windkessel* and *Westkessel* models are instances of two-compartments model (the heart and the vascular system), the latter featuring a more precise description of the vascular compartment. More complex examples can be found in [15] - Chap 5, and [17], Chap. 14, where an accurate sensitivity analysis of the parameters of a four-compartments description of the cardiovascular system is carried out. Other references are [18] and [47].

Lumped parameters models that we are going to introduce in view of multiscale modeling are, in fact, compartments models which can be described by following the two steps mentioned above. In particular, in the present notes, we will firstly introduce lumped parameters models (Sect. 2.2.1 and 2.2.2) for 1) a simple compliant cylindrical vessel and 2) the heart.

The mathematical description for the former will be obtained by a suitable averaging of the Navier-Stokes equations, after a few simplifying assumptions.

Then in (Sect. 2.2.3), we will consider models for the whole circulation, based on the assembly of models of type 1) and 2). We will extensively exploit at the descriptive level the analogy between hydraulic and electric networks.

2.2.1 Lumped parameters models for a cylindrical compliant vessel

The basic equations

Let us consider the simple cylindrical artery Ω illustrated in Fig. 2.6. In the sequel, $\mathbf{x}$ denote the vector of the space variables and $t > 0$ the time.

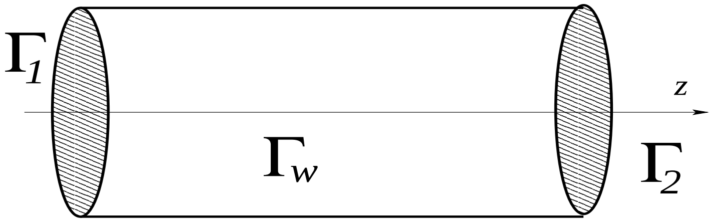

v

Figure 2.6: Single compliant vessel.

The boundary of Ω is composed by the compliant wall Γ_w and the sections Γ_1 and Γ_2, which are the interfaces with the rest of the system. We call Γ_1 the *proximal* or *upstream* section, i.e. the section from which the blood comes from the heart; similarly, Γ_2 is the *distal* or *downstream* section, through which the blood leaves Ω towards the periphery.

We associate to each particular district of this type an oriented *axis* z. The position along the vessel will be therefore identified by means of the abscissa associated to the axis, still called z. In Ω, we have $0 \le z \le l$ (we adopt here the symbol l instead of L to denote the vessel length since the latter will be used later to indicate the inductance). For every z, the axial section of the vessel will be denoted by $\mathcal{A}(t,z)$. In the sequel, $A(t,z)$ denotes the measure of $\mathcal{A}(t,z)$. Assuming a circular cylindrical domain, we will have $A(t,z) = \pi R^2(t,z)$, where $R(t,z)$ is the radius of the section in z. Finally $d\sigma$ will denote the infinitesimal part of $\mathcal{A}(t,z)$ and the volume of Ω will be denoted by $\mathcal{V}$.

The mathematical model for the description of the blood flow in Ω is given by the Navier-Stokes equations for an incompressible fluid associated to a constitutive structure law relating the stresses exerted by the fluid on the wall to the displacement of the vascular tissue: see e.g. [9], [28].

In order to obtain a simplified model for this fluid-structure interaction problem, we will introduce the same assumptions as for the deduction of 1D models discussed in [10] (Sect. 3), that we recall here for the sake of completeness.

1 *Axial symmetry*, i.e. independence of all quantities involved from the circumferential coordinate θ.

2 *Radial displacement*, i.e. each point on Γ_w moves only in the radial direction, so that if $\boldsymbol{\eta}$ is the wall displacement, $\mathbf{e}_r$ the unit vector in the radial direction and R_0 a reference radius, $\boldsymbol{\eta} = (R - R_0)\mathbf{e}_r$. This hypothesis is justified by experimental observations (see e.g. [11]).

3 *Fixed cylindrical axis*, i.e. the axis z is assumed to be fixed in time.

4 *Constant pressure on each section,* i.e. the pressure P is assumed to be dependent only on the axial coordinate z and time t.

5 *No body forces,* i.e. body forces such as the gravity are neglected.

6 *Dominance of axial velocity,* i.e. the components of the velocity field orthogonal to the axis z are considered negligible compared to the axial one. The axial component of the velocity will be denoted by u_z.

We now set $Q(t,z) := \displaystyle\int_{\mathcal{A}(t,z)} u_z d\sigma$ the volumetric mean flux through section $\mathcal{A}$ and, in particular,

$$Q_1(t) := Q\left(t,0\right), \quad P_1(t) = P\left(t,0\right), \quad Q_2(t) := Q\left(t,l\right), \quad P_2(t) = P\left(t,l\right). \tag{2.1}$$

Starting from the previous assumptions, we integrate over each section $\mathcal{A}(t,z)$ the (simplified) Navier-Stokes equations and obtain (see e.g. [9] and [10], Sect. 3) the following set of 1D equations for $z \in (0,L)$ and $t \in (0,T]$,

$$\begin{cases} \dfrac{\partial A}{\partial t} + \dfrac{\partial Q}{\partial z} = 0 \\ \dfrac{\partial Q}{\partial t} + \alpha \dfrac{\partial}{\partial z}\left(\dfrac{Q^2}{A}\right) + \dfrac{A}{\rho}\dfrac{\partial P}{\partial z} + K_R \dfrac{Q}{A} = 0 \end{cases} \tag{2.2}$$

complemented by a suitable set of boundary and initial data. In (2.2), α (momentum-flux correction coefficient), ρ (blood density) and K_R (friction parameter) are assumed to be constant. In particular, K_R is related to the (kinematic) blood viscosity ν and its actual expression depends on the velocity profile. If a parabolic Poiseuille profile is assumed (which is of course a simplifying assumption), $K_R = 8\pi\nu$. A, P and Q are the unknowns. In order to close the system, we need a further equation which is provided by the constitutive law for the vessel tissues. Different possible laws are discussed in [10], Sects. 3.1 and 3.3. In the context of lumped parameters model we assume a simple linear algebraic law. In other words, we introduce a further assumption.

7 *The vessel wall displacement η is related to the pressure P by an algebraic linear law.* Following [10], Sect. 3, we take

$$(P - P_{ext}) = c(R - R_0) = \beta_0 \frac{\sqrt{A} - \sqrt{A_0}}{A_0} \tag{2.3}$$

where P_{ext} and $A_0 = \pi R_0^2$ are a constant reference pressure and a constant reference area, respectively, while c is a constant related to the physical properties of the vascular tissues and $\beta_0 = A_0 c/\sqrt{\beta_0}$. More precisely, if h denotes the thickness of the vascular tissue, E the Young modulus, ξ^2 the Poisson ratio (which we set equal to 1/2, as for an incompressible tissue), the linear elastic constitutive law yields:

$$c = \frac{hE}{R_0^2(1-\xi^2)} = \frac{4hE}{3R_0^2}.$$

Now, observing that:

$$\frac{\partial A}{\partial t} = 2\pi R \frac{d\eta}{dt} \approx 2\pi R_0 \frac{\partial \eta}{\partial t},$$

we will assume:

$$\frac{\partial A}{\partial t} = \frac{3\pi R_0^3}{2Eh} \frac{\partial}{\partial t} P$$

In the sequel, we will set $k_1 = \dfrac{3\pi R_0^3}{2Eh}$.

In order to provide a lumped description of the behavior of the blood in the whole district Ω we need to perform a further averaging of (2.2), (2.3) over the axial coordinate $z \in (0, l)$. To this aim, it is useful to introduce the following notation. We define as *the (volumetric) mean flow rate over the whole district* the quantity

$$\hat{Q} = \frac{1}{l} \int_{\mathcal{V}} u_z dv = \frac{1}{l} \int_0^l \int_{\mathcal{A}(z)} u_z d\sigma dz = \frac{1}{l} \int_0^l Q dz. \tag{2.4}$$

Similarly , we define the *mean pressure over the whole compartment* as

$$\hat{p} = \frac{1}{l} \int\limits_0^l P dz. \tag{2.5}$$

Let us integrate in $z \in (0, l)$ the system (2.2). From the first equation, we obtain

$$\int_0^l \frac{\partial A}{\partial t} dz + \int_0^l \frac{\partial Q}{\partial z} dz = 0.$$

Since from (2.3), $\partial A / \partial t = k_1 \partial P / \partial t$ we can exploit the notation introduced in (2.1). The previous equation becomes

$$k_1 l \frac{d\hat{p}}{dt} + Q_2 - Q_1 = 0. \tag{2.6}$$

From the integration of the second equation of (2.2) we obtain

$$\int_0^l \left[\frac{\partial Q}{\partial t} + \alpha \frac{\partial}{\partial z} \left(\frac{Q^2}{A} \right) + \frac{A}{\rho} \frac{\partial P}{\partial z} + K_R \frac{Q}{A} \right] dz =$$
$$l \frac{d\hat{Q}}{dt} + \alpha \left[\frac{Q_2^2}{A_2} - \frac{Q_1^2}{A_1} \right] + \int_0^l \left[\frac{A}{\rho} \frac{\partial P}{\partial z} + K_R \frac{Q}{A} \right] dz = 0$$

In order to have a *linear model*, we introduce some further assumptions. Namely,

8 *The contribution of the convective terms may be neglected*, i.e. we assume that the quantity $(\frac{Q_2^2}{A_2} - \frac{Q_1^2}{A_1})$ is small compared to the other terms and can be discarded, which is quite reasonable for short pipes.

9 *The variation of A with respect to z is small compared to that of P and Q*, so that in the last integral we have

$$\int_0^l \left[\frac{A}{\rho}\frac{\partial P}{\partial z} + K_R\frac{Q}{A}\right] dz \approx \int_0^l \left[\frac{A_0}{\rho}\frac{\partial P}{\partial z} + K_R\frac{Q}{A_0}\right] dz.$$

By exploiting these assumptions we obtain, after some algebraic manipulations,

$$\frac{\rho l}{A_0}\frac{d\hat{Q}}{dt} + \frac{\rho K_R l}{A_0^2}\hat{Q} + P_2 - P_1 = 0. \tag{2.7}$$

Equations (2.6) and (2.7) represent a lumped parameters description of the blood flow in the compliant cylindrical vessel Ω, and involve the mean values of the flow rate and the pressure over the domain, as well as the upstream and downstream flow rate and pressure values. This model can be considered an *elementary brick* for the description of more complex systems, as will be presented next.

In this perspective, it is useful to introduce the “electric-network” analogy of these equations.

Electric analog of the lumped parameter models

In equations (2.6),(2.7) we have some coefficients which have been obtained from the integration process. They are in fact the lumped parameters which summarize the basic geometrical and physical features of the dynamic system formed by the blood flow and the vessel wall. Let us try to summarize their meaning.

R In (2.7) we set $R := \frac{\rho K_R l}{A_0^2}$. If we assume a parabolic velocity we have

$$R = \frac{8\pi\rho\nu l}{\pi^2 R_0^4} = \frac{8\mu l}{\pi R_0^4},$$

where R represents the *resistance* induced to the flow by the blood viscosity. Different expressions for R can be obviously obtained for different velocity profiles or if a non Newtonian rheology is introduced into the model (see e.g. [35], [45], [10], Sect. 3).

L In (2.7) we set $L := \frac{\rho l}{A_0} = \frac{\rho l}{\pi R_0^2}$. L represents the inertial term in the momentum conservation law and will be called the *inductance* of the flow.

C In (2.6) we set $C := k_1 l = \frac{3\pi R_0^3 l}{2Eh}$. C represents the coefficient of the mass storage term in the mass conservation law, due to the *compliance* of the vessel.

With this notation, equations (2.6), (2.7) becomes

$$\begin{cases} C\dfrac{d\hat{p}}{dt} + Q_2 - Q_1 = 0 \\ L\dfrac{d\hat{Q}}{dt} + R\hat{Q} + P_2 - P_1 = 0. \end{cases} \tag{2.8}$$

Now, assume that some upstream and downstream data are available. For instance, suppose that Q_1 *and* P_2 *are given*. Then, (2.8) represents a system of two equations for four unknowns, $\hat{Q}, \hat{p}, P_1$ and Q_2. In order to close mathematically the problem we need some further assumptions. In particular, the dynamic of the system is represented by $\hat{p}$ and $\hat{Q}$, i.e. by the unknowns that are under time derivative (the *state variables*), so it is reasonable to approximate the unknowns on the upstream and downstream sections with the state variables, that is

$$\hat{p} \approx P_1, \quad \hat{Q} \approx Q_2.$$

With these additional assumptions, which are reasonable for a short cylindrical pipe, the lumped parameters model becomes:

$$\begin{cases} C\dfrac{dP_1}{dt} + Q_2 = Q_1 \\ L\dfrac{dQ_2}{dt} + RQ_2 - P_1 = P_2. \end{cases} \tag{2.9}$$

where the upstream and downstream prescribed data have been plugged into the right hand side. This system can be illustrated by the electric $\mathcal{L}$-network shown in Figure 2.7 (left). The compliance has been gathered on section Γ_1, where the flow rate is prescribed, and the inertial effects have been allocated on Γ_2, where the mean pressure is provided.

In the electric network analogy, the blood flow rate is assimilated to the current, while the blood pressure corresponds to the voltage (see Tab. 2.1).

In a similar way, if the pressure P_1 and the flow rate Q_2 are prescribed, we still approximate the unknown quantities on the upstream and downstream sections with the state variables, i.e. $\hat{p} \approx P_2, \quad \hat{Q} \approx Q_1$, yielding the system

$$\begin{cases} C\dfrac{dP_2}{dt} - Q_1 = Q_2 \\ L\dfrac{dQ_1}{dt} + RQ_1 + P_2 = P_1. \end{cases} \tag{2.10}$$

The electric analog counterpart of (2.10), called $\mathcal{L}$-inverted network, is given in Figure 2.7, right.

The case when the mean pressures P_1 and P_2 are prescribed, can be modelled by a cascade connection of $\mathcal{L}$ and $\mathcal{L}$-inverted lumped representations. More precisely, if P_1, P_2 are prescribed at upstream and downstream, respectively, we split the vessel into two parts Ω_1 and Ω_2 of length

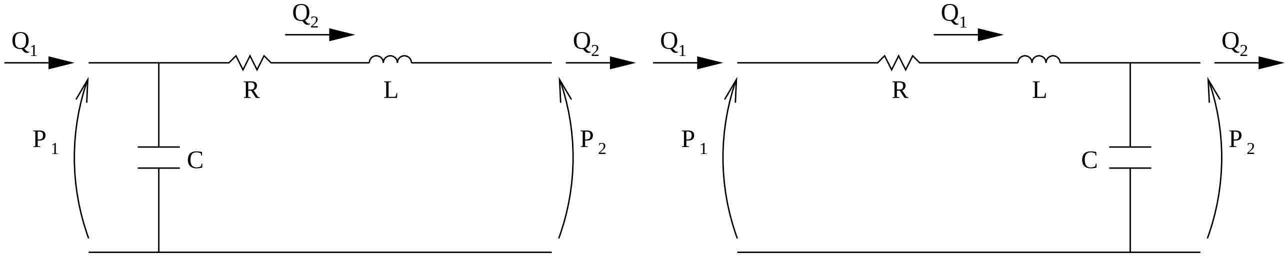

Figure 2.7: Lumped $\mathcal{L}$-network (left) and $\mathcal{L}$-inverted network (right) equivalent to a short pipe

Table 2.1: Correspondence table of the analogy between electric and hydraulic networks.

HYDRAULIC	ELECTRIC
Pressure	Voltage
Flow rate	Current
Blood viscosity	Resistance R
Blood inertia	Inductance L
Wall compliance	Capacitance C

$l/2$. On the first part Ω_1 we assume that P_1 and the flow rate $\hat{Q}$ are known; on the second one Ω_2 we assign the flow rate $\hat{Q}$ and the downstream pressure P_2. In this way, the whole vessel Ω is reinterpreted as the $\mathcal{T}$-network shown in Figure 2.8. The resulting differential system can be written:

$$\frac{d\mathbf{y}}{dt} = A\mathbf{y} + \mathbf{b}(P_1, P_2)$$

with $\mathbf{y} = (P, Q_1, Q_2)^T$,

$$A = \begin{pmatrix} 0 & \frac{1}{C} & -\frac{1}{C} \\ -\frac{2}{L} & -\frac{R}{L} & 0 \\ \frac{2}{L} & 0 & -\frac{R}{L} \end{pmatrix}, \quad \mathbf{b}(P_1, P_2) = \begin{pmatrix} 0 \\ \frac{2}{L} p_{up} \\ -\frac{2}{L} p_{dw} \end{pmatrix}.$$

In a similar way, if both the flow rates Q_1 and Q_2 are prescribed, the following system can be obtained

$$\frac{d\mathbf{y}}{dt} = A\mathbf{y} + \mathbf{b}(Q_1, Q_2)$$

where $\mathbf{y} = (P_1, Q, P_2)^T$,

$$A = \begin{pmatrix} 0 & -\frac{2}{C} & 0 \\ \frac{1}{L} & -\frac{R}{L} & -\frac{1}{L} \\ 0 & \frac{2}{C} & 0 \end{pmatrix}, \qquad \mathbf{b}(Q_1, Q_2) = \begin{pmatrix} \frac{2}{C} Q_1 \\ 0 \\ -\frac{2}{C} Q_2 \end{pmatrix}.$$

In this case, the vessel Ω is described by the electric π-network, obtained as a cascade connec-

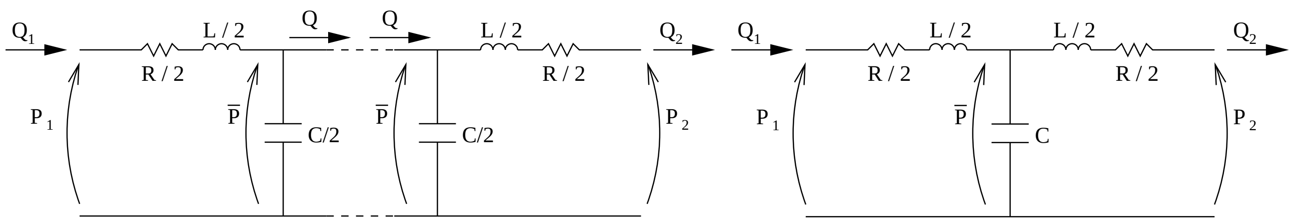

Figure 2.8: Cascade connection of a $\mathcal{L}$-inverted and a $\mathcal{L}$-network (left), lumped $\mathcal{T}$-network (right).

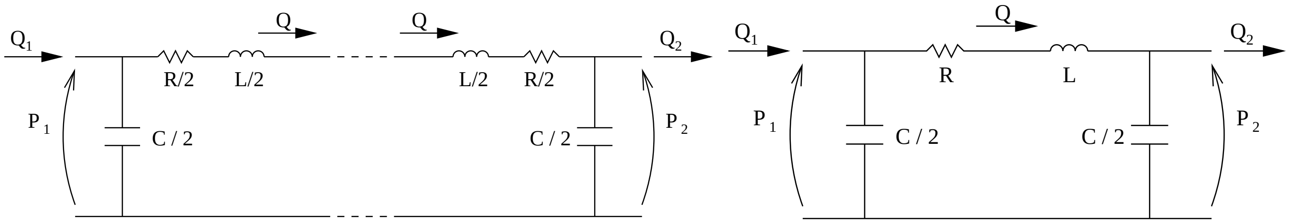

Figure 2.9: Cascade connection of a $\mathcal{L}$-network and a $\mathcal{L}$-inverted one (left), lumped π-network (right).

tion of a $\mathcal{L}$-network and a $\mathcal{L}$-inverted network (Figure 2.9).

In terms of electric network analysis, all the circuits we found are examples of *four terminal network* (see Fig. 2.10). A mathematical analysis of this kind of problems in the frequency domain can be carried out by introducing a matrix of impedances or transfer functions between each of the terminal variables of the network. Since in the present notes we are interested to couple lumped parameters models to the complete set of the Navier-Stokes equations, which are solved in the time domain, we will not go into details about the concept of matrix of impedances and their use. The interested reader may referred to [22], [13].

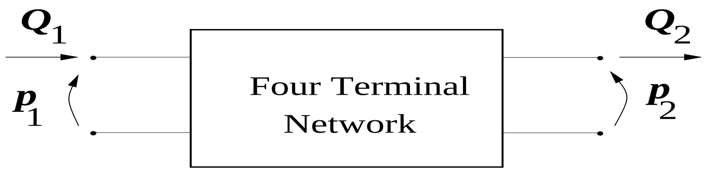

Figure 2.10: Generic representation for a four terminal network.

Let us observe that the four different circuits arise from four different possible assumptions about the kind of data prescribed on the upstream and downstream sections. With a little abuse of notation we could call them “boundary data”[2]. The four different lumped models can be considered therefore as the lumped parameters simplification of four different “boundary” values problems.

Remark 2.2. Steady motion. *Whenever the blood motion is steady, we may observe that the lumped model of the compliant tube reduces to an algebraic relation, corresponding to a purely resistive network. This is the assumption frequently made, for instance, in the capillaries districts, where the pulsatility of blood induced by the periodic pumping of the heart is largely damped by the compliance of the large arteries and the blood flow is essentially steady.*

Remark 2.3. *Some of the simplifications introduced can be removed (or reduced) by modifying the network. For instance, if one wants to account for a possible blood seepage in the domain* Ω *(due e.g. to some small branches that we do not want to model), it is possible to correct the original* π *network as illustrated in Fig. 2.11 where the added resistance* G *governs the amount of seepage (see [16]).*

---

[2] Actually, in the simplification leading to lumped parameters models the dependence on the space variables has been lost in the averages, so there is not a “boundary” of the domain.

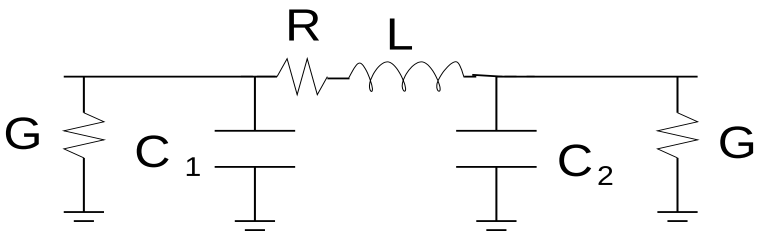

Figure 2.11: Electric network analogous for system accounting for a seepage.

*We present an improved model that can be appropriate when dealing with a large vessel. In this case, axial averaging could turn out to be too rough. We may deduce a more sophisticated scheme, a the price of a higher complexity, by considering the vessel as a set of cylindrical shells or "anular" elements (see 2.12) where the blood flows (*sleeve effect*). In this way, the transversal average is taken not over the whole section, but over* n *concentric annuli, reducing the associated approximation (see [16], [35]). The corrections can be still reinterpreted in terms of electric circuits, as illustrated in Fig. 2.13.*

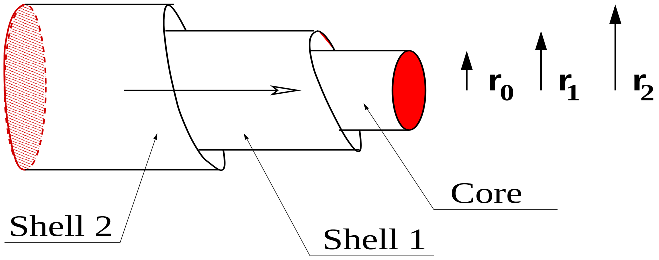

Figure 2.12: Representation of a cylindrical vessel as a set of concentric cylindrical shell ("sleeve effect")

2.2.2 Lumped parameters models for the heart

The heart is a special "compartment" of the vascular system that need a specific representation in the lumped parameters framework. It is subdivided into two parts, called to the right and the left heart, respectively, separated by the *septum*. The right heart supplies the pulmonary circulation, while the left pumps the blood into the systemic tree (see Fig. 2.14).

Each side consists of two chambers, the atrium and the ventricle, seprated by the atrioventricular valves (the *tricuspid* valve in the right side, the *mitral* valve in the left one). Their role is to receive fluid at low pressure and transfer it to a higher pressure region. In other words, each side acts as a *pump* (see [15]). Consider, for instance, the left ventricle. During the *diastolic phase* the inflow valve is open and the aortic outflow valve is closed. The blood enters from the left atrium at a pressure roughly equal that in the pulmonary veins (≈ 5 mm Hg). During the *systolic phase* the inflow valve closes while the outflow opens. Blood is then pumped into the arterial system with a pressure of about 100 mm Hg. Each ventricle can be described *as a vessel*

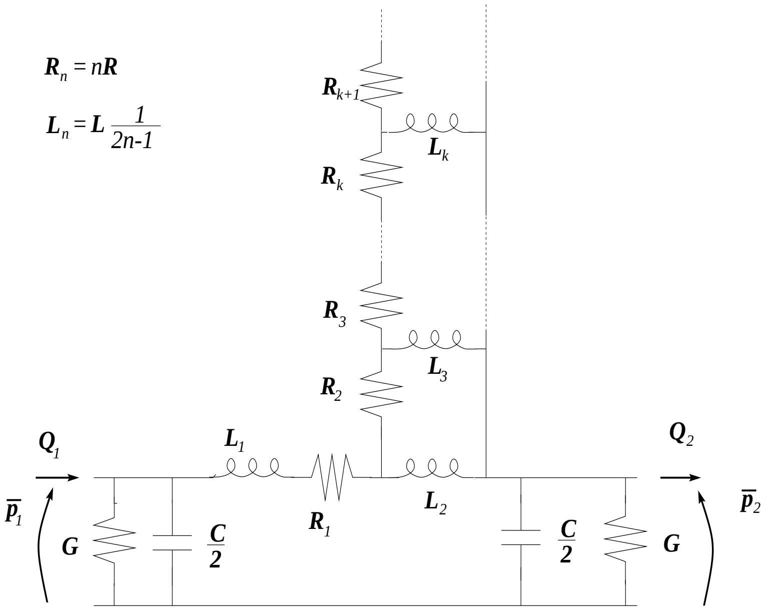

Figure 2.13: Electrical network for a compliant tube that accounts for both seepage and “sleeve effect”.

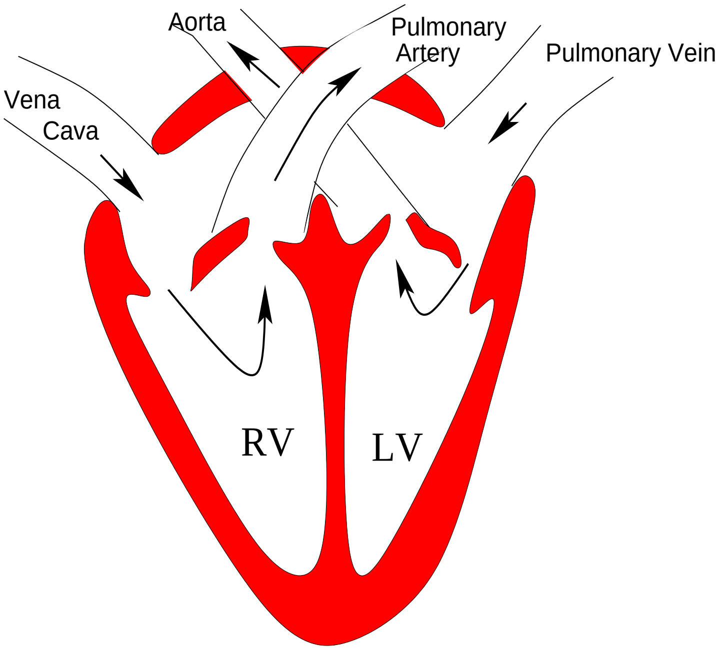

Figure 2.14: Schematic representation of the heart.

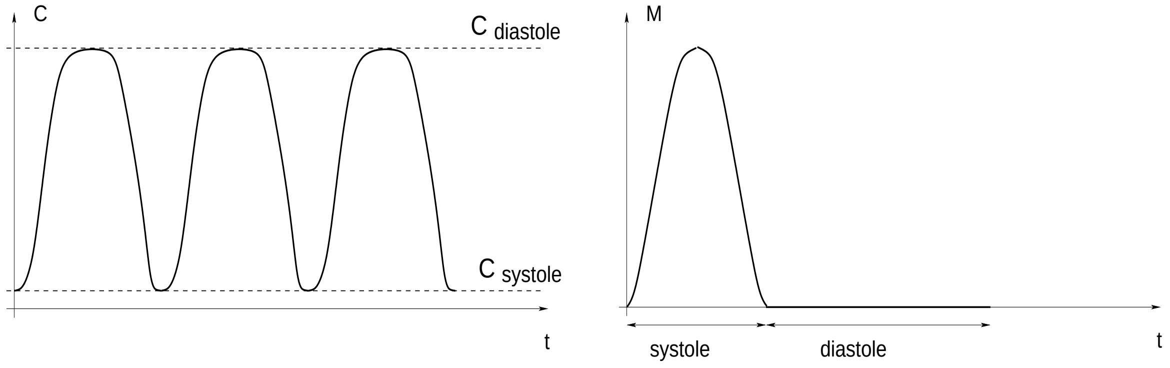

Figure 2.15: Qualitative diagrams for the time dependent compiance $C(t)$ in the ventricles (left) and the activating function $M(t)$ (right)

where the most significant feature is the compliance and *the compliance changes with time* (see [37], [15], [17], [5]). A corresponding law for the ventricle dynamics is therefore:

$$V(t) = V_d + C(t)\,(P(t) - P_{ext}) \tag{2.11}$$

where $P(t) - \P_{ext}$ is the intramural pressure, $V(t)$ the volume, $C(t)$ the compliance, V_d the so-called *dead volume*, which is assumed to be constant and taken equal to zero, as well as P_{ext}, for the sake of simplicity. $C(t)$ assumes values between two extrema, C_s and C_d (Fig. 2.15- left), giving rise to pressure-volume diagrams such the one illustrated in Fig. 2.16. This relation is however not suited for our computations, since in fact it describes the behaviour of the ventricle in its operative conditions, i.e. when "coupled" with the circulatory system. We want a model for the ventricle alone: its actual behaviour should be the result of the coupling and not imposed a priori!.

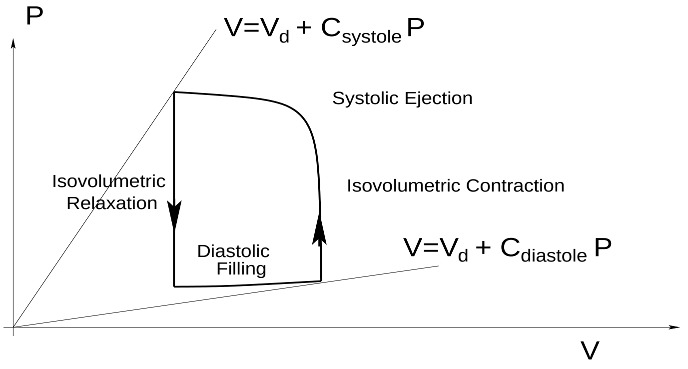

Figure 2.16: Diagram of the relation between pressure P and volume V in the a ventricle.

The starting point of the alternative model is the relation that links pressure and radius of an elastic spherical ball filled with fluid. Here and in the following we take $P_{ext} = 0$. We have

$$\pi R^2 P = 2\pi E h_0 R \frac{R - R_0}{R_0},$$

where R_0 is the reference sphere radius, which is the one reached when $P = 0$, h_0 a reference thickness of the ball surface and E the Young modulus. The contraction of the cardiac muscle may be taken into account by an increase of E (stiffening) and by a shortening of the muscle length (that is a reduction of R_0). It is more convenient to express this relation as a function of the volume V, instead of the radius. By recalling that $V = \dfrac{4}{3}\pi R^3$, a linearisation procedure leads to

$$P = \frac{E(t)h_0}{2\pi R_0^3(t)}\left(V - V_0(t)\right),$$

where we have indicated the coefficients that change in time because of the action of the muscle. This simplified model does indeed describe the major characteristic of the ventricle. If we indicate $C(t) = \dfrac{2\pi R_0^3(t)}{E(t)h_0}$ we may re-write the relation in the mode compact form

$$V(t) = C(t)P(t) + V_0(t),$$

where the difference with (2.11) is that now V_0 as the meaning of the reference volume, which changes in time because of the variation of the length of the muscle fibers.

By deriving with respect to time we obtain

$$\frac{dV}{dt} = Q = \frac{dC}{dt}P + C\frac{dP}{dt} + M_Q(t) \qquad (2.12)$$

where Q represents the (incoming) flow rate and $M_Q = \frac{dV_0}{dt}$ is the action exerted by the contraction of the cardiac muscle.

A lumped representation (electric analog) of each ventricle[3] is given in Fig. 2.17, where R accounts for an additional viscous resistance inside the ventricle and M_Q is represented by a generator of current.

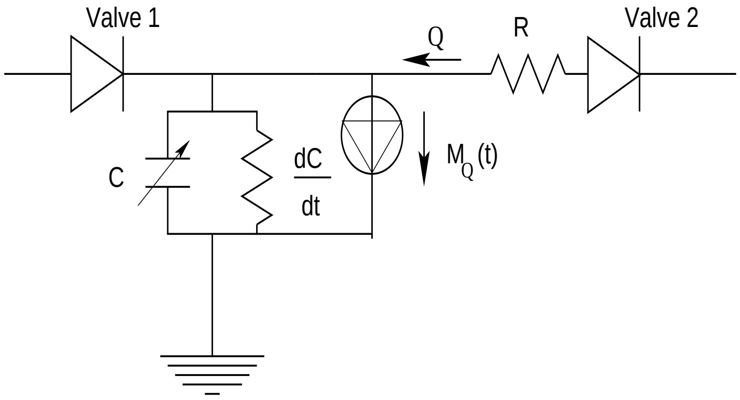

Figure 2.17: Network for the lumped parameters modeling of a ventricle.

In Fig. 2.17 we show the electrical equivalent of the proposed model, where presence of heart valves has been taken into account by *diodes* which allow th current flow in one direction only [4]. The behaviour of a diod can be represented mathematically by its characteristic function

$$Q(P) = Q_0(e^{\beta P} - 1)$$

---

[3] A mechanical representation of the heart working based on the classical Hill's model for the muscle can be found in [18] and [47].

[4] The same representation can be used also for the valves in the venous system, whenever needed.

where β is usually large. Sometimes this law is approximated by a two-state description (see Fig. 2.18),

$$\begin{array}{lll} Q = 0 & \text{if} & P < 0, \\ P = 0 & \text{if} & Q > 0. \end{array}$$

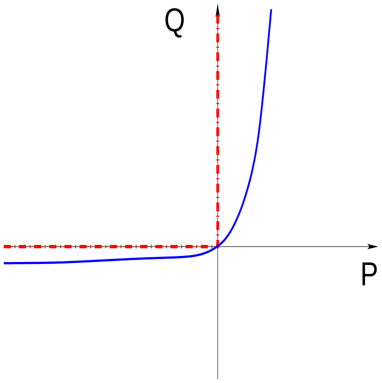

Figure 2.18: Characteristic function $Q - P$ of a diod: the correct curve (solid) and the approximated one (dotted).

We point out that the presence of the valves *introduces a nonlinear relation* in the lumped parameters model.

Sometimes the pressure-volume relation (2.13) is rewritten in the form

$$Q = \frac{dC}{dt} P^* + C \frac{dP^*}{dt}, \quad \text{with } P^* = P - M_P, \tag{2.13}$$

which corresponds to the circuit in Fig. 2.19. Here the action of the muscle is simulated by a voltage generator, instead of a current one. Furthermore, the variable resistance term $\frac{dC}{dt}$ is sometimes neglected.

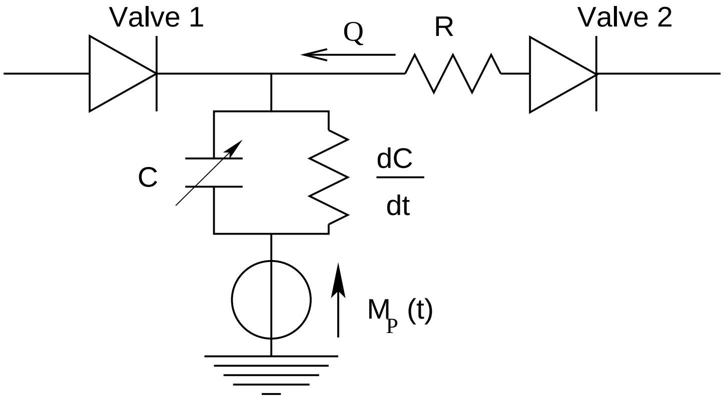

Figure 2.19: Alternative representation for the lumped parameters modeling of a ventricle.

2.2.3 Lumped parameters models for the circulatory system

The compartments described in the two previous Sections are the elementary bricks for building models for the whole system. As previously pointed out, the number of compartments depends on the accuracy requested to the model and, definitely, on the number of vessels that it is worthwhile to represent separately as single units.

The connection among the compartments is driven by *flux and momentum conservation* at the interfaces. As a direct consequence of the electric analogy the quantities that are matched are Q and the pressure P. There is a difference in this respect to the coupling of 1D models ([10]), where we imposed the continuity of total pressure. This choice is indeed consistent with the hypothesis of negligible convective terms.

In the electric analog, these relations correspond to the application of the classical *Kirchhoff laws* for the nodes (conservation of current) and the nets (conservation of the voltage). An sketch of the possible connection of different compartments is given in Fig. 2.20.

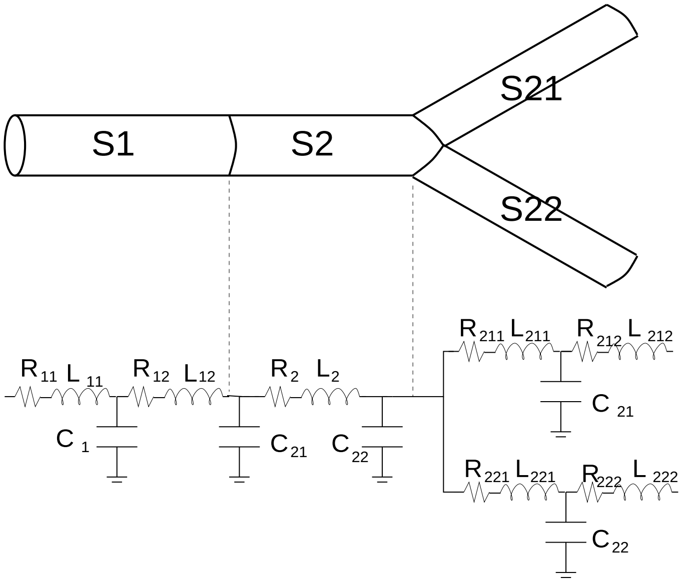

Figure 2.20: Lumped parameters model for a branched vessel as a cascade of T and π networks.

A detailed electric analog for the circulation is provided in [45] and in [24], where hundreds of elementary compartments are accounted for. A simpler example, taken from [25], is shown in Figure 2.21. Here, a particular attention is given to the coronary circulation, while the pulmonary circulation and the capillary bed have been represented with only a few elements.

From the mathematical viewpoint, a general representation of lumped parameters models is a Differential-Algebraic-Equations (DAE) system in the form

$$\left\{ \begin{array}{l} \dfrac{d\mathbf{y}}{dt} = B(\mathbf{y}, \mathbf{z}, t) \quad t \in (0, T] \\ G(\mathbf{y}, \mathbf{z}) = 0 \end{array} \right. \tag{2.14}$$

together with the *initial condition vector* $\mathbf{y}|_{t=t_0} = \mathbf{y}_0$. Here, $\mathbf{y}$ is the vector the state variables (associated to capacitors and inductors), $\mathbf{z}$ are other variables of the network and G the algebraic equations that derive from the Kirchhoff laws. If we suppose that the Jacobian matrix:

$$J := \frac{\partial G}{\partial \mathbf{z}}$$

is non singular[5], by the Implicit Function theorem we can express $\mathbf{z}$ as function of $\mathbf{y}$ and resort to the reduced Cauchy problem

$$\begin{aligned} &\frac{d\mathbf{y}}{dt} = \mathbf{\Phi}(\mathbf{y}, t) = A(\mathbf{y}, t)\mathbf{y} + \mathbf{r}(t) \quad t \in (0, T] \\ &\mathbf{y} = \mathbf{y}_0, \quad \text{at } t = t_0. \end{aligned} \tag{2.15}$$

The time dependence of matrix A is due to the heart action and is related to the variable ventricles compliances, while the dependence of A on $\mathbf{y}$ is due to the presence of diodes (non linear term). The forcing term $\mathbf{r}$ depends on t through the function $M(t)$.

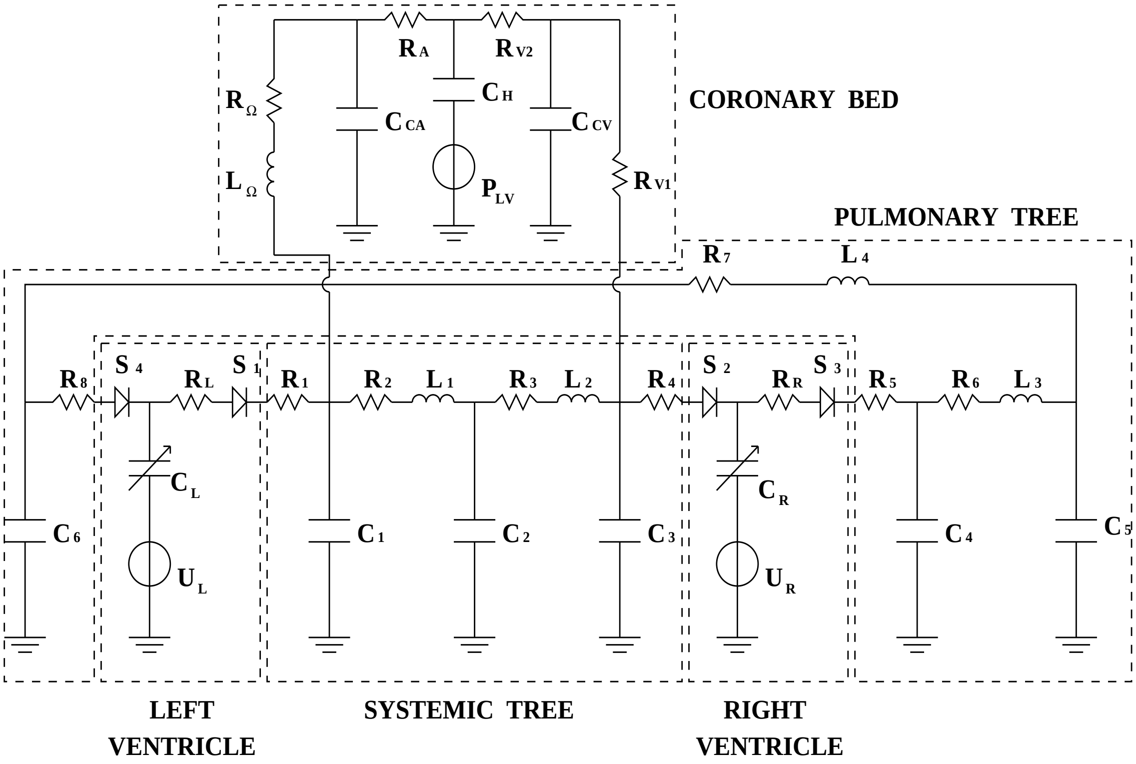

Figure 2.21: A possible network model for circulation.

Remark 2.4. Mathematical analysis of lumped parameters models: *We remind that, from classical results of Calculus, it is possible to prove that:*

1. *if $\mathbf{\Phi}(\mathbf{y}, t)$ is continuosly differentiable there exists a time interval $[0, T^*]$ in which the solution of the problem exists and is unique;*
2. *if, moreover, the derivatives $\partial\Phi_i/\partial y_j$ are bounded in all the time interval $[0, T]$, then the solution of the Cauchy problem exists and is unique in $[0, T]$.*

In the sequel, we will suppose that the previous hypotheses are verified.

---

[5] In this case, the DAE system is said to be *of index 1*.

2.3 Basic numerical issues for multiscale modeling

Our goal is now to investigate specific problems arising from the mathematical and numerical coupling of different models for blood flow, ranging from the Navier-Stokes equations up to lumped parameters models. In particular, we will have to manage the interfaces between models featuring a different level of detail. It is to be expected that the more accurate (pointwise) model would need on the interfaces more data than the mean models could give, being by far less accurate. The data referred to the lumped submodel are indeed a spatial average of the pointwise quantities which are, on the other side, considered by the accurate local submodel and that would be needed on the interfaces in order to make it well posed the Navier-Stokes boundary problem. We have, therefore, the problem of giving a well posed formulation of the local subproblem, filling up the defective data set provided by the reduced (1D or 0D as well) submodels. The main concern of multiscale modeling is to carry out this completion minimizing, as far as possible, the perturbations on the numerical solution. For example, if the flow rate (*mean value*) is known on the upstream section of a vascular district, there are many velocity profiles (*pointwise values*) on that section that can be associated to such mean data and, therefore, can be correctly prescribed to the Navier-Stokes problem. However, the choice of a specific profile will strongly influence (or perturb) the numerical solution in a non-controlled way. The present Section illustrates some techniques for avoiding the prescription of a velocity profile and, in general, for reducing perturbations on the numerical solution.

Before addressing the problem in its general form, let us illustrate it on a simple example, with the aim of introducing in a more concrete way the defective data problems.

2.3.1 A first (simple) example

Let us consider the simple electric circuit in Figure 2.22 (left), where y_i denotes the pressure drop applied to C_i (for $i = 1, \dots, 4$) and the flow rate crossing R_i and L_i (for $i = 5, \dots, 8$). Let Ω be the cylindrical pipe identified with the branch consisting of R_8 and L_8. Denote by P_{up}, P_{dw} and Q_{up}, Q_{dw} the mean pressures and the flow rates at the upstream and downstream, respectively. Setting $\mathbf{y} = (y_1, \dots, y_7)^T$, the circuit in Figure 2.22 (right) is described by the following system

$$\begin{cases} \dfrac{d\mathbf{y}}{dt} = A\mathbf{y} + \mathbf{r}(t) + \mathbf{b}(Q_{up}(t), Q_{dw}(t)), \qquad t > 0 \\ \mathbf{y}(0) = \mathbf{y}_0 \end{cases} \tag{2.16}$$

where

$$A_{ij} = \begin{cases} 1/C_i & \text{if } i = 1,2,3, j = i+4, \\ -1/C_i & \text{if } i = 2,3,4, j = i+3, \\ -R_i/L_i & \text{if } i = 5,6,7, j = i, \\ 1/L_i & \text{if } i = 5,6,7, j = i-3, \\ -1/L_i & \text{if } i = 6,7, j = i-4, \\ 0 & \text{otherwise,} \end{cases}$$

and

$$r_i = \begin{cases} U/L_5 & \text{if } i = 5, \\ -U/L_6 & \text{if } i = 6, \\ 0 & \text{otherwise.} \end{cases}$$
$$b_i = \begin{cases} Q_{up}/C_1 & \text{if } i = 1, \\ Q_{dw}/C_4 & \text{if } i = 4, \\ 0 & \text{otherwise.} \end{cases} \tag{2.17}$$

Here, $\mathbf{r}(t)$ accounts for the action of the pressure source $M(t)$ and $\mathbf{b}(Q_{up}, Q_{dw})$ involves the interface flow rates. As a first simple example of a multiscale model, we replace the branch containing R_8 and L_8 by the more accurate 3D model based on the Navier-Stokes system, in a fixed (no compliance) cylindrical domain. As mentioned above, the main concern in this heterogeneous coupling refers to the matching between two subproblems with a substantially different level of accuracy. In the example at hand, in particular, we have that the state variables of the lumped model $y_1(t)$ and $y_4(t)$ of the lumped model play the role of the mean pressure on the upstream and downstream sections of the district modelled by the Navier-Stokes equations. In other words, we have the interface conditions:

$$\begin{cases} y_1(t) = \int_{\Gamma_{up}} p(\mathbf{x}, t) d\boldsymbol{\gamma}, \\ y_4(t) = \int_{\Gamma_{dw}} p(\mathbf{x}, t) d\boldsymbol{\gamma}. \end{cases} \tag{2.18}$$

In a similar way, for what concerns the flow rates, we have other interface conditions by setting

$$\begin{cases} Q_{up}(t) = \int_{\Gamma_{up}} \mathbf{u} \cdot \mathbf{n} d\boldsymbol{\gamma}, \\ Q_{dw}(t) = \int_{\Gamma_{dw}} \mathbf{u} \cdot \mathbf{n} d\boldsymbol{\gamma}. \end{cases} \tag{2.19}$$

The heterogeneous model obtained coupling the Navier-Stokes equations and the ODE system (2.16) with the interface conditions (2.18) or (2.19) (or even their possible combinations) is not well posed. Indeed, in a classical setting, a necessary condition for the well posedness of the Navier-Stokes problem is that at each point on the boundary a number of conditions equal to the spatial dimension of the problem. Typically, one can prescribe the components of the velocity (Dirichlet boundary condition) or those of the Cauchy normal stress (Neumann boundary condition), or an appropriate combination of velocity and normal stress. In this case, on the contrary, we have only averaged quantities on the upstream and downstream boundary portions. Therefore, if we want to use reduced models (0D or 1D) to feed boundary data to a more detailed local model, we need a way to "translate" these mean quantities in mathematically sound boundary conditions for the Navier-Stokes equations.

A viable approach to handle the case of defective boundary conditions, is provided by the so called *do-nothing* boundary conditions proposed in [14], where it is provided a general framework for managing defective boundary data problems. This approach is really effective and easy in particular for the case of *defective pressure boundary data*, the so-called *mean pressure drop problem*. The general settings in the case of a *mean flow rate (or net flux) problems* seems however more difficult to implement due to the presence of special functional spaces which are not easy to discretize in the framework, for instance, of a Galerkin-Finite Elements discretization. For this reason, another, somehow more flexible, alternative approach based on the use of *Lagrange multipliers*, has been proposed in [8].

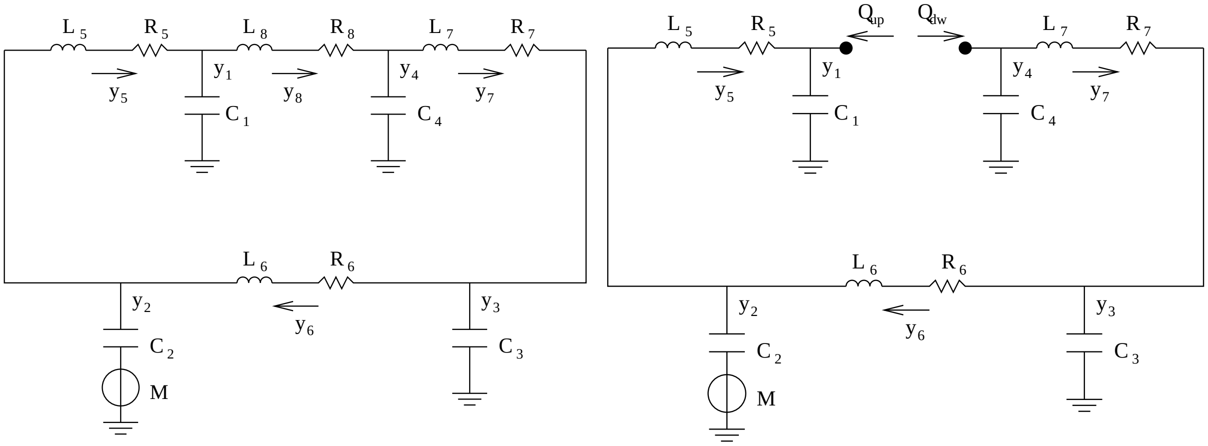

Figure 2.22: Example of lumped model (left) and the system obtained by elimination of the pipe represented by R_8 and L_8 (right).

We will introduce the do-nothing approach both in the case of the mean pressure and net flux problems in Sect. 2.3.2. The Lagrange multiplier approach for the flux problem and its numerical implementation are presented in Sect. 2.3.2

2.3.2 Defective boundary data problems

For the sake of clarity, let us provide a general statement of defective boundary data problems. Let Ω be a bounded domain of $\mathbb{R}^d$, $d = 2$ or 3, whose boundary $\partial\Omega$ is decomposed into the union of Γ and several disjoint sections $\Gamma_0, \Gamma_1, \ldots, \Gamma_n$, $n \geq 1$ (see Figure 2.23).

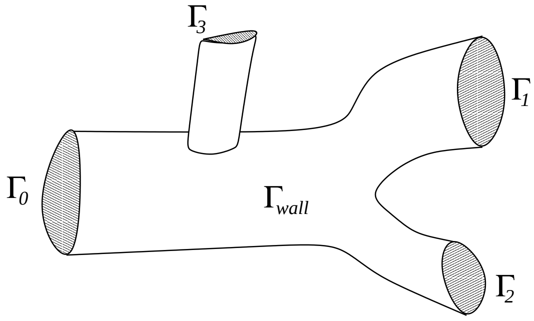

Figure 2.23: The partition of the boundary of the domain Ω.

We are interested in solving the Navier-Stokes equations in Ω:

$$\left\{ \begin{array}{rcll} \dfrac{\partial}{\partial t}\mathbf{u} + \mathbf{u} \cdot \boldsymbol{\nabla}\mathbf{u} + \boldsymbol{\nabla} p - \nu \triangle \mathbf{u} & = & \mathbf{f}, & t > 0 \\ \mathrm{div}(\mathbf{u}) & = & 0, & t > 0 \\ \mathbf{u} & = & \mathbf{u}_0, & t = 0, \end{array} \right. \tag{2.20}$$

supplemented by homogeneous boundary conditions on Γ_{wall} (assuming for the sake of simplicity that the walls are rigid):

$$\mathbf{u}|_{\Gamma} = 0, \tag{2.21}$$

while two different kinds of boundary conditions are of some interest in the multiscale coupling and will be considered on the sections $\Gamma_i,\ i = 0, \ldots, n$.

The first condition refers to the *mean pressure problem,* already introduced in the Example above, which requires that

$$\frac{1}{\text{meas}(\Gamma_i)} \int_{\Gamma_i} p\, ds = P_i, \quad i = 0, \ldots, n, \tag{2.22}$$

where each P_i is a prescribed function of the time t, constant on Γ_i.

The second condition we address is the *flow rate problem*

$$\int_{\Gamma_i} \mathbf{u} \cdot \mathbf{n}\, ds = Q_i, \text{ for } i = 0, \ldots, n, \tag{2.23}$$

where the (volumetric) flow rates Q_i's are assigned functions of time. Observe that, due to the fluid incompressibility and the rigidity of the wall, a compatibility relation must exist among the fluxes Q_i, namely:

$$Q_0 + Q_1 + \ldots + Q_n = 0. \tag{2.24}$$

As we have previously pointed out, the initial-boundary value problem (2.20)-(2.21) with either (2.22) or (2.23) is not well-posed from a physical point of view. In the do-nothing approach, a particular weak or variational formulation of the boundary problem is devised which allows to fulfill conditions (2.22) (resp. (2.23)) at some extent, giving rise to a well-posed problem. In fact, this formulation forces in an implicit way some natural (Neumann-like) boundary conditions which selects one particular solution among all the possible physical solutions of the original differential problem. The completition of the defective boundary data set is essentially an implicit by-product of the choice of the suitable variational formulation[6], which is based on a natural set of boundary conditions, by far less perturbative than essential (Dirichlet) ones. We will here give a brief presentation of this approach. Let us introduce the functional spaces

$$V = \left\{ \mathbf{v} \in \left[H^1(\Omega)\right]^d, \mathbf{v}|_{\Gamma} = 0 \right\} \qquad \text{and} \qquad M = L^2(\Omega).$$

where $L^2(\Omega)$ is the space of functions q such that[7] $\int_\Omega q^2 d\omega < \infty$, and $H^1(\Omega)$ is the Sobolev space of functions belonging to $L^2(\Omega)$ together with their first derivatives. Morevoer, denote by V' the dual space of V, i.e. the space of linear and continuous functionals acting on elements of V. We suppose that $\mathbf{f} \in V'$ and we introduce the functional $\phi_i \in V'$, $i = 0, \ldots, n$ which measures the flux of a vector function through the surface Γ_i. Precisely

$$< \phi_i, \mathbf{v} >= \int_{\Gamma_i} \mathbf{v} \cdot \mathbf{n}\, ds, \quad \forall \mathbf{v} \in V,$$

where $\mathbf{n}$ is the outward unit normal vector on $\partial\Omega$. For this reason ϕ_i is called the *flux functional* on Γ_i.

---

[6] "when you know nothing, do nothing", J. Heywood.

[7] Integration is always intended in the Lebesgue sense.

The mean pressure drop problem

The "do-nothing" formulation for the *mean pressure problem* reads : find $\mathbf{u} \in V$ and $p \in M$ such that, for all $\mathbf{v} \in V$ and $q \in M$,

$$\left\{ \begin{array}{rcl} \left(\dfrac{\partial}{\partial t}\mathbf{u} + \mathbf{u} \cdot \boldsymbol{\nabla}\mathbf{u}, \mathbf{v}\right) + \nu(\boldsymbol{\nabla}\mathbf{u}, \boldsymbol{\nabla}\mathbf{v}) - (p, \mathrm{div}(\mathbf{v})) & = & < \mathbf{f}, \mathbf{v} > - \sum_{i=0}^{n} P_i < \phi_i, \mathbf{v} >, \\ (q, \mathrm{div}(\mathbf{u})) & = & 0, \end{array} \right. \tag{2.25}$$

for all $t > 0$, with $\mathbf{u} = \mathbf{u}_0$ for $t = 0$.

It follows easily, by using the Green formula, that the solution of (2.25) satisfies

$$\left(p - \nu\frac{\partial u_n}{\partial \mathbf{n}}\right)\Big|_{\Gamma_i} = P_i, \qquad \frac{\partial \mathbf{u}_\tau}{\partial \mathbf{n}}\Big|_{\Gamma_i} = 0, \quad \text{for } i = 0, \dots, n, \tag{2.26}$$

where we have set $u_n = \mathbf{u} \cdot \mathbf{n}$ and $\mathbf{u}_\tau = \mathbf{u} - u_n\mathbf{n}$.

Thus

$$\frac{1}{\mathrm{meas}(\Gamma_i)} \int_{\Gamma_i} p\, ds = P_i + \frac{\nu}{\mathrm{meas}(\Gamma_i)} \int_{\Gamma_i} \frac{\partial u_n}{\partial \mathbf{n}}\, ds. \tag{2.27}$$

We conclude that the desired condition (2.22) is recovered exactly only in those cases where the last integral in (2.27) vanishes. This occurs, for instance, when Γ_i is a plane section perpendicular to a cylindrical pipe. Otherwise, P_i will be, in fact, the mean value of the normal component of the normal stresses on Γ_i. In other words, the defective boundary data set is implicitly completed in this variational formulation by assuming that the viscous stress components vanish (i.e. can be neglected) on the boundary at hand.

For well posedness results of this problem see [14] and also [41] (in the specific context of blood flow problems).

The mean flow rate problem

For the *prescribed flow rate problem*, the "do-nothing" approach can be formulated as follows. Let us introduce the space

$$V^\star = \{\mathbf{v} \in V, < \phi_i, \mathbf{v} >= 0, i = 0, \dots, n\},$$

and the vector functions $\mathbf{b}_i \in V, \quad i = 1, \dots, n$ (called *flux-carriers*) that satisfy:

$$\mathrm{div}(\mathbf{b}_i) = 0, \quad \int_{\Gamma_0} \mathbf{b}_i \cdot \mathbf{n}\, ds = -1, \quad \int_{\Gamma_j} \mathbf{b}_i \cdot \mathbf{n}\, ds = \delta_{ij}, \quad \text{for } i, j = 1, \dots, n.$$

The weak formulation of problem (2.20), (2.21), (2.23) proposed in [14] reads:

find $\mathbf{u} = \mathbf{W} + \sum_{i=1}^{n} Q_i\mathbf{b}_i$, with $\mathbf{W} \in V^\star$ and $p \in M \setminus \mathbb{R}$ such that for all $\mathbf{v} \in V^\star$ and $q \in M$

$$\left\{ \begin{array}{rcl} (\dfrac{\partial}{\partial t}\mathbf{u} + \mathbf{u} \cdot \boldsymbol{\nabla}\mathbf{u}, \mathbf{v}) + \nu(\boldsymbol{\nabla}\mathbf{u}, \boldsymbol{\nabla}\mathbf{v}) - (p, \mathrm{div}(\mathbf{v})) & = & 0, \\ (q, \mathrm{div}(\mathbf{u})) & = & 0, \end{array} \right. \tag{2.28}$$

for all $t > 0$, with $\mathbf{u} = \mathbf{u}_0$ for $t = 0$.

In this case, it is less clear which kind of "do-nothing" boundary conditions are implicitly forced by selecting this variational formulation. It is possible to prove (see [14] and [42]) that the corresponding solution satisfies:

$$\left(p - \nu \frac{\partial \mathbf{u}}{\partial \mathbf{n}} \right) \mathbf{n}|_{\Gamma_i} = C_i \mathbf{n}, \tag{2.29}$$

where the C_i's are *a priori* unknown functions of time (independent of space variables). In other words, besides the mean flow rates, variational formulation (2.28) prescribes that the tangential component of the stress tensor vanishes and the normal one is a (unknown) constant on each boundary where the flux is assigned. For a well posedness analysis of this problem, see [14].

The formulation of the *mean pressure problem* may be easily discretized as it can be regarded as a classical Navier-Stokes problem with Neumann boundary conditions. On the other hand, the definition of the functional space $V^\star$ makes the numerical implementation of the *prescribed flow rate problem* less straightforward, since it is not so easy to find suitable finite dimensional subspaces. This motivates investigations of an alternative formulation of the problem (see [8]).

A Lagrange multiplier approach for flow rate boundary conditions Consider the initial-boundary values problem given by (2.20) and (2.21) and the net flux conditions:

$$< \phi_i, \mathbf{u} >= \int_{\Gamma_i} \mathbf{u} \cdot \mathbf{n} \, ds = Q_i, \qquad \text{for } i = 1, \ldots, n. \tag{2.30}$$

We assume that the compatibility condition (2.24) is fulfilled.

Rather than (defective) boundary conditions, (2.30) can be regarded as a set of *constraints* for the solution of the problem at hand. Starting from this viewpoint, a possible way for forcing such constraints resorts to the Lagrange multiplier approach. According to this strategy, the equations to be solved are *penalized* by the presence of the constraint, weighted by suitable (unknown) coefficients, the Lagrange multipliers[8]. The original problem is therefore reformulated in an *augmented* fashion, due to the presence of the multipliers (see e.g. [12]).

In the present case, this approach leads to the following variational problem: look for $\mathbf{u} \in V$, $p \in M$ and $\lambda_1, \ldots, \lambda_n \in \mathbb{R}$ such that, for all $\mathbf{v} \in V$ and $q \in M$,

$$\begin{cases} (\frac{\partial}{\partial t}\mathbf{u} + \mathbf{u} \cdot \boldsymbol{\nabla}\mathbf{u}, \mathbf{v}) + \nu(\boldsymbol{\nabla}\mathbf{u}, \boldsymbol{\nabla}\mathbf{v}) + \displaystyle\sum_{i=1}^{n} \lambda_i < \phi_i, \mathbf{v} > - (p, \text{div}(\mathbf{v})) =< \mathbf{f}, \mathbf{v} >, \\ (q, \text{div}(\mathbf{u})) = 0, \\ < \phi_i, \mathbf{u} >= Q_i, \qquad i = 0, .., n, \end{cases} \tag{2.31}$$

for all $t > 0$, with $\mathbf{u} = \mathbf{u}_0$ for $t = 0$.

It is possible to prove the following Proposition (for the proof, see [8]):

Proposition 2.1. *Any smooth solution of (2.33) satisfies the additional boundary conditions*

$$\left(p - \nu \frac{\partial u_n}{\partial \mathbf{n}} \right) |_{\Gamma_i} = \lambda_i, \quad \textit{and} \quad \frac{\partial \mathbf{u}_\tau}{\partial \mathbf{n}}|_{\Gamma_i} = 0, \quad 0 = 1, \cdots n. \tag{2.32}$$

Furthermore, $(\mathbf{u}, p)$ *satisfies (2.20), (2.21), (2.30).*

---

[8] We remind that in the same perspective, the pressure of the incompressible Navier-Stokes equations can be regarded as the Lagrange multiplier of the incompressibility constraint - see e.g. [29].

Remark 2.5. *By virtue of the compatibility condition $\sum_i Q_i = 0$, it is possible to prove that one of the Lagrange multiplier can be arbitrarily chosen (see [8]). A possible reformulation of the problem is therefore: look for $\mathbf{u} \in V$, $p \in M$ and $\lambda_1, \ldots, \lambda_n \in \mathbb{R}$ such that, for all $\mathbf{v} \in V$ and $q \in M$, for all $t > 0$, with $\mathbf{u} = \mathbf{u}_0$ for $t = 0$.*

$$\begin{cases} (\dfrac{\partial}{\partial t}\mathbf{u} + \mathbf{u} \cdot \boldsymbol{\nabla}\mathbf{u}, \mathbf{v}) + \nu(\boldsymbol{\nabla}\mathbf{u}, \boldsymbol{\nabla}\mathbf{v}) + \displaystyle\sum_{i=1}^{n} \lambda_i < \phi_i, \mathbf{v} > - (p, div(\mathbf{v})) =< \mathbf{f}, \mathbf{v} >, \\ (q, div(\mathbf{u})) = 0, \\ < \phi_i, \mathbf{u} >= Q_i, \qquad \mathbf{i = 0, .., n} \end{cases} \tag{2.33}$$

where i now starts from 1, and λ_0 has been set $= 0$, so that we actually impose on Γ_0:

$$\left(-p\mathbf{n} + \frac{\partial \mathbf{u}}{\partial \mathbf{n}}\right)\Big|_{\Gamma_0} = 0. \tag{2.34}$$

In the sequel, in the rigid wall case, we will refer to this formulation of the problem.

In the perspective of defective boundary data problems, we could say that among all possible solutions of (2.20), (2.21), (2.30), (2.34), problem (2.33) selects the one that satisfies the additional boundary condition (2.32). From a theoretical viewpoint, the Lagrange multiplier approach is very close to the do-nothing formulation. Comparing (2.29) and (2.32), we may note, in fact, that the Lagrange multipliers corresponding to the constraints on the flux are in fact equal to the "*a priori* unknown" constants of the do-nothing formulation (2.29). On the other hand, this approach uses a standard functional space V which can be more straightforwardly discretized than the space V^*.

In the remainder of the present Section, we will refer in particular to the Lagrange multiplier approach for the steady Stokes problem, which embodies however all the relevant difficulties of the Lagrange multiplier approach:
find $(\mathbf{u}, p, \lambda_1, \ldots, \lambda_n) \in V \times M \times \mathbb{R}^n$, such that, $\forall(\mathbf{v}, q) \in V \times M$

$$\begin{cases} \nu(\boldsymbol{\nabla}\mathbf{u}, \boldsymbol{\nabla}\mathbf{v}) + \sum_{i=1}^{n} \lambda_i < \phi_i, \mathbf{v} > - (p, \mathrm{div}(\mathbf{v})) &= < \mathbf{f}, \mathbf{v} >, \\ (q, \mathrm{div}(\mathbf{u})) &= 0, \\ < \phi_i, \mathbf{u} > &= Q_i, \ i = 1, .., n. \end{cases} \tag{2.35}$$

A well posedness analysis for (2.35) can be found in [8]. The extension of the analysis to the complete time-dependent, nonlinear problem (2.33) can then be carried out by usual techniques for nonlinear problem (see [43]).

The numerical solution of the Lagrange multipliers problem In order to discretize formulation (2.35), we introduce a Galerkin approximation based on the finite dimensional spaces $V_h \subset V$ and $M_h \subset M$, which we assume to satisfy the well-known LBB condition[9]

$$\forall q_h \in M_h \quad \exists \mathbf{v}_h \in V_h, \, \mathbf{v}_h \neq 0 \, : \quad (q_h, \mathrm{div}(\mathbf{v})_h) \geq \beta_h |q_h|_{L^2} |\mathbf{v}_h|_{H^1}. \tag{2.36}$$

Let $(\mathbf{u}_h, p_h, \lambda_{1h}, \ldots, \lambda_{nh})$ be the solution of the discrete problem. We denote by $(u_i)_{i=1..dN}$ (resp. $(p_i)_{i=1..M}$) the components of $\mathbf{u}_h$ (resp. p_h) with respect to a basis $\{\mathbf{v}_i\}$ of V_h (resp. $\{q_i\}$

---

[9] For the numerical discretization of the stationary Stokes problem, see e.g. [29], Chap. 9.

of M_h). Finally, we introduce the vectors $U = (u_1, .., u_{dN}) \in \mathbb{R}^{dN}$, $P = (p_1, .., p_M) \in \mathbb{R}^M$ and $\Lambda = (\lambda_{1h}, \dots, \lambda_{nh}) \in \mathbb{R}^n$.

Then the discrete counterpart of (2.35) gives rise to the following algebraic system of equations

$$\left\{ \begin{array}{rcl} AU + D^T P + \Phi^T \Lambda & = & F, \\ D\,U & = & 0, \\ \Phi\,U & = & Q, \end{array} \right. \tag{2.37}$$

where $A \in \mathbb{R}^{dN \times dN}$ is the stiffness matrix, $D \in \mathbb{R}^{M \times dN}$ is the matrix associated to the divergence operator and Φ is the $n \times dN$ matrix whose lines are given by the vectors $\phi_i = (\int_{\Gamma_i} \mathbf{v}_1 \cdot \mathbf{n}\, ds, \dots, \int_{\Gamma_i} \mathbf{v}_{dN} \cdot \mathbf{n}\, ds),\ i = 1, \dots, n$.

It is possible to prove that this system is non singular ([8]). However, this system is not a classical Stokes problem, so its numerical solution should require the set up of an “ad hoc” solver. On the other hand, there is no numerical convenience in setting up a solver computing simultaneously U, P and Λ, since the matrix associated to system (2.37) is very ill conditioned in real applications[10]. Therefore, as for the standard Stokes problem (see [29]), it is worthwhile to resort to splitting methods which reduce the problem to a series of smaller and easier to solve steps. Among the different methods for achieving this goal, in particular we illustrate a strategy that has the advantage of separating the fluid (velocity and pressure) from the multipliers computation. In this way, if a (Navier-)Stokes solver is available[11], it can be actually adopted for solving the augmented problem.

A solution algorithm We rewrite (2.37) in the form

$$\begin{bmatrix} S & \tilde{\Phi}^T \\ \tilde{\Phi} & 0 \end{bmatrix}, \begin{bmatrix} X \\ \Lambda \end{bmatrix} = \begin{bmatrix} G \\ Q \end{bmatrix} \tag{2.38}$$

where $\tilde{\Phi} = [\Phi, 0] \in \mathbb{R}^{n \times (dN+M)}$, $X = [U, P]^T$, $G = [F, 0]^T$. The matrix

$$S = \begin{bmatrix} A & D^T \\ D & 0 \end{bmatrix}$$

has a standard Stokes form, corresponding to the discretization of a Neumann problem on the boundaries where the net fluxes are prescribed. If the two discrete spaces V_h and M_h satisfy the LBB condition (2.36), S is non singular (see, e.g. [29], [3]). We can then eliminate the unknown X from (2.38), obtaining a system for the Lagrange multiplier:

$$\tilde{\Phi} S^{-1} \tilde{\Phi}^T \Lambda = \tilde{\Phi} S^{-1} G - Q. \tag{2.39}$$

This system can be solved by an appropriate iterative method. For instance, if we denote $R := \tilde{\Phi} S^{-1} \tilde{\Phi}^T$ and $\mathbf{b} := \tilde{\Phi} S^{-1} G - Q$, we could resort to the classical Richardson scheme (see e.g. [36]), that reads:
given an initial guess $\Lambda^{(0)}$, for $k = 0, 1, 2, \dots$, solve:

$$\Lambda^{(k+1)} - \Lambda^{(k)} = \mathbf{b} - R\Lambda^{(k)}$$

---

[10] this is true, in general, for the fluid problem alone, so the same is expected for the augmented one.

[11] for instance, a commercial package

until convergence.

The computation of the residual $\mathbf{r}^{(k)} := \mathbf{b} - R\Lambda^{(k)}$ is carried out by the following steps:

$$\begin{cases} \mathbf{y}^{(k)} = \tilde{\Phi}^T \Lambda^{(k)} \\ \mathbf{z}^{(k)} = S^{-1}\mathbf{y}^{(k)} \Rightarrow S\mathbf{z}^{(k)} = \mathbf{y}^{(k)} \\ \mathbf{r}^{(k)} = \mathbf{b} - \tilde{\Phi}\mathbf{z}^{(k)}. \end{cases}$$

The second step of the residual computation corresponds to a usual Stokes problem and can be carried out by means of a standard solver. This means that each iteration of the Richardson algorithm will require the computation of the fluid. Two further solution of problem in S are required for the computation of $\mathbf{b}$ (before the application of the Richardson scheme) and for the computation of X (after the Richardson scheme)

$$SX = G - \tilde{\Phi}^T \Lambda.$$

This seems quite expensive. However, the matrix R is usually quite small, being $(n+1) \times (n+1)$ where $n+1$ is the number of sections where the net fluxes are prescribed, or $n \times n$ in the case of a rigid pipe (when one of the Lagrange mulitplier can be arbitrarily chosen), so the number of iterations required will be accordingly small. Moreover, the computational efficiency can be dramatically improved, in terms of number of iterations, if other iterative schemes are adopted. For instance, if A is symmetric, as in the case of the Stokes problem, then $R = \tilde{\Phi}S^{-1}\tilde{\Phi}^T$ is symmetric and positive definite (see [8]). Consequently, the Conjugate Gradient (CG) algorithm may be used, which is proved to converge to the solution in a number of iterations equal to the dimension of the matrix R ($n+1$ or n). For instance, in the case of a rigid cylindrical pipe we have just one Lagrange multiplier, and (2.39) reduces to just one scalar equation. In this case, one iteration of the CG algorithm suffices (in exact arithmetic) to obtain the solution. The algorithm reads as follows:

given $\lambda^{(0)} \in \mathbb{R}$,

$$\begin{array}{ll} (i) & SX_1 = G - \tilde{\Phi}^T \lambda^{(0)} \\ (ii) & r_0 = \tilde{\Phi}X_1 - Q \\ (iii) & SX_2 = \tilde{\Phi}^T r_0 \\ (iv) & \lambda = \lambda^{(0)} + \dfrac{r_0^2}{r_0\tilde{\Phi}X_2} r_0 = \lambda^{(0)} + \dfrac{r_0^2}{\tilde{\Phi}X_2} \\ (v) & SX = G - \tilde{\Phi}^T \lambda \end{array}$$

Since in this case it is to be expected that the CG method converges in one iteration, λ and X are the solutions of (2.38). This algorithm requires the solution of 3 Stokes problems at steps (i), (iii) and (v).

Remark 2.6. *If we discretize in time the unsteady Navier-Stokes system (2.33) by, for instance, a semi-implicit Euler scheme, and in space by the finite element method, we will produce an algebraic system analogous to (2.37), where the matrix* A *is now given by*

$$A = \frac{1}{\Delta t}M + B + K$$

Δt being the time-step, M and B the mass and advection matrices and K the stiffness matrix. The method based on the solution of a system in R can be still adopted. However, in this case, the CG method is not applicable, since S is no longer symmetric. On the other hand, suitable extension of the CG method to the non symmetric case, such as the GMRes algorithm (see [36]) can be prusued, still ensuring a low number of iterations, that means a low number of fluid problems to be solved (see [43]).

Numerical results

In order to assess the proposed methodologies, we consider a case where the analytical solution of the Stokes (and the Navier-Stokes) equations is known. More precisely, we consider the *Womersley* solution, which describes the transient flow in a cylindrical pipe associated to a time-periodic pressure gradient (see e.g. [22]). As such, it is a transient counterpart of the well known Poiseuille solution.

Precisely, if the pressure gradient is given by

$$\nabla p = \frac{dp}{dz}(t)\mathbf{e}_z = -\rho \sin(\omega t)\mathbf{e}_z,$$

z being the pipe axial coordinate and ρ the fluid density, the velocity $\mathbf{u}$ reduces only to its axial component, i.e. $\mathbf{u} = u_z\mathbf{e}_z$, and the analytical expression for u_z is

- *2D case* (flow between two infinite planes - see [42]):

  $$u_z(r,t) = \sum_0^\infty \gamma_{2k+1} \sin\left(\frac{(2k+1)\pi}{2r_0} r\right)$$

  where

  $$\gamma_l = \frac{4a}{\pi l(l^4\sigma^2 + \omega^2)} \left(l^2\sigma \sin(\omega t) + \omega e^{-l^2\sigma t} - \omega \cos(\omega t)\right).$$

  Here $\sigma = \frac{\mu\pi^2}{4\rho r_0^2}$, r is the transverse coordinate, $2r_0$ the distance between the two planes and μ the dynamic fluid viscosity.

- *3D case* (flow in a cylindrical pipe - see [46]):

  $$u_z(r,t) = \mathrm{Re}\left\{ -\frac{a}{\omega}\left(1 - \frac{J_0\left(i^{3/2}\sqrt{\frac{\rho\omega}{\mu}} r\right)}{J_0\left(i^{3/2}\sqrt{\frac{\rho\omega}{\mu}} r_0\right)}\right) e^{i\omega t}\right\}$$

  where r is the radial coordinate, r_0 the cylinder radius and J_0 the Bessel function of first kind and of order zero.

We tested the two problems for the cases in which the analytical solution is the Womersley profile.

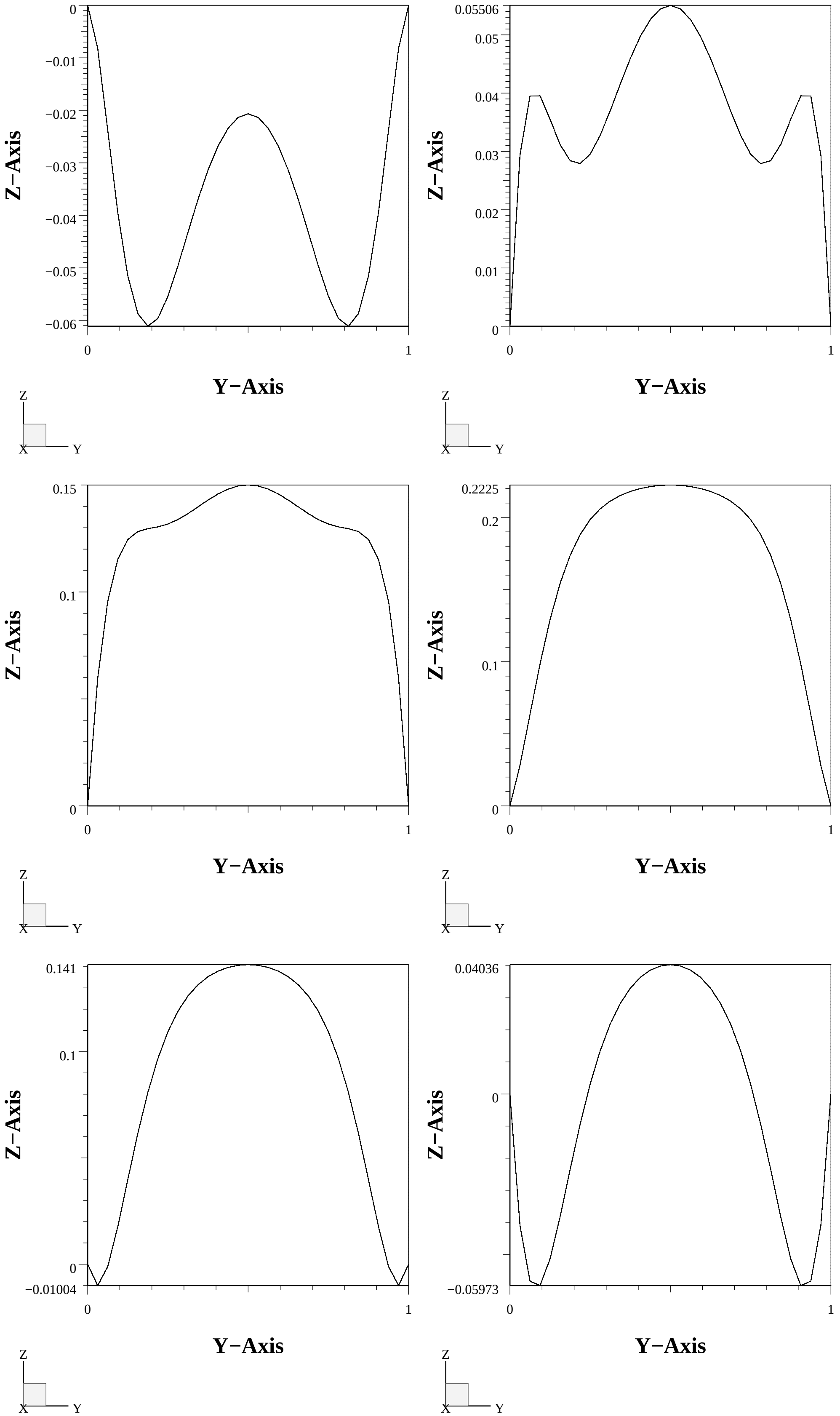

Figure 2.24: Velocity profiles of the numerical solution on a square obtained imposing a perioidic pressure drop.

Womersley flow: mean pressure drop problem In a 2D cylindrical pipe of unit length we prescribe the mean pressures:

$$P_{upstream} = 0, \qquad P_{downstream} = -\rho \sin(\omega t)\mathbf{e}_z.$$

We solved the problem (see [42]) with $\rho = 2$ and $\omega = 2\pi$, following the do-nothing formulation (2.25). In this way, we are forcing the conditions 2.27, which are fulfilled by the Womersley solution. In Fig. 2.24, the axial velocity profiles in different instants are illustrated.

In Tab. 2.2 we report the errors with respect to the Womersley 2D solution. The time discretization scheme is a Backward Euler first order method and the error reduction when the time step Δt decreases actually confirm a first order accuracy for the velocity with respect to the “exact” Womersley solution.

Womersley flow: net flux problem In both the 2D and 3D test cases, we have imposed homogeneous Neumann boundary conditions at the inflow, while at the outflow we prescribe the flow rate associated to the Womersley solution. In Figure 2.25 we show the axial velocity profile for the 2D case at two different times, together with the velocity profile at the inflow. The solution obtained still agrees very well with the analytical Womersley solution. A single condition on the flow rate at the outflow, imposed through a Lagrange multiplier, is sufficient to recover the Womersley flow. It is worthwhile outlining that *the Womersley profile is an outcome of the computation, it has not been forced anyway.*

The same experiment has been carried out in 3D and the result is shown in Figure 2.26. Here, the computed velocity field at three different times is illustrated, together with the corresponding axial velocity profile on the inflow section. Again, we outline the excellent agreement with the analytical solution.

2.4 Multiscale models

Having developed techniques for managing local 3D problems with mean boundary data in a numerically sound way, we are now in position of describing complete geometrical multiscale models, both from a mathematical and numerical viewpoints. We will start considering a 3D-0D model, discussing its well posedness and numerical methods for the coupling. (Sect. 2.4.1). Then, we will introduce 3D-1D models investigated different possible matching conditions and their implementation (Sect. 2.4.2). Numerical results are presented in Sect. 2.5.

Table 2.2: Error for different time steps, Womersley mean pressure drop 2D problem. Finite element space discretization ($h = 1/64$), backward Euler time discretization.

TIME STEP	VELOCITY ERROR	PRESSURE ERROR
$1/200$	3.6×10^{-2}	1.4×10^{-1}
$1/500$	1.0×10^{-2}	1.4×10^{-2}
$1/1000$	5.0×10^{-3}	2.3×10^{-3}
$1/2000$	2.6×10^{-3}	4.0×10^{-4}

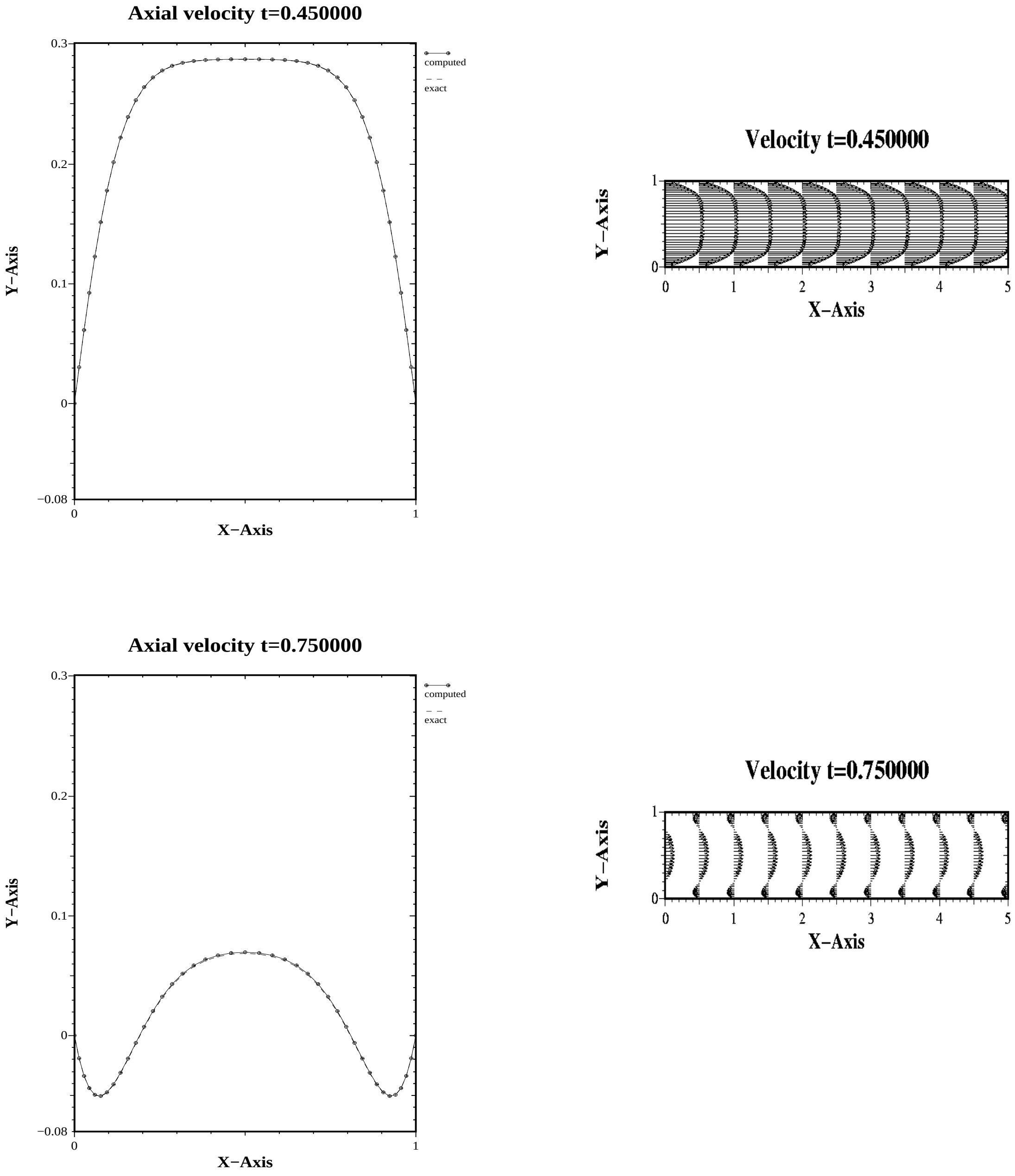

Figure 2.25: 2D numerical solution obtained imposing the flux of the Womersley solution at the outflow section.

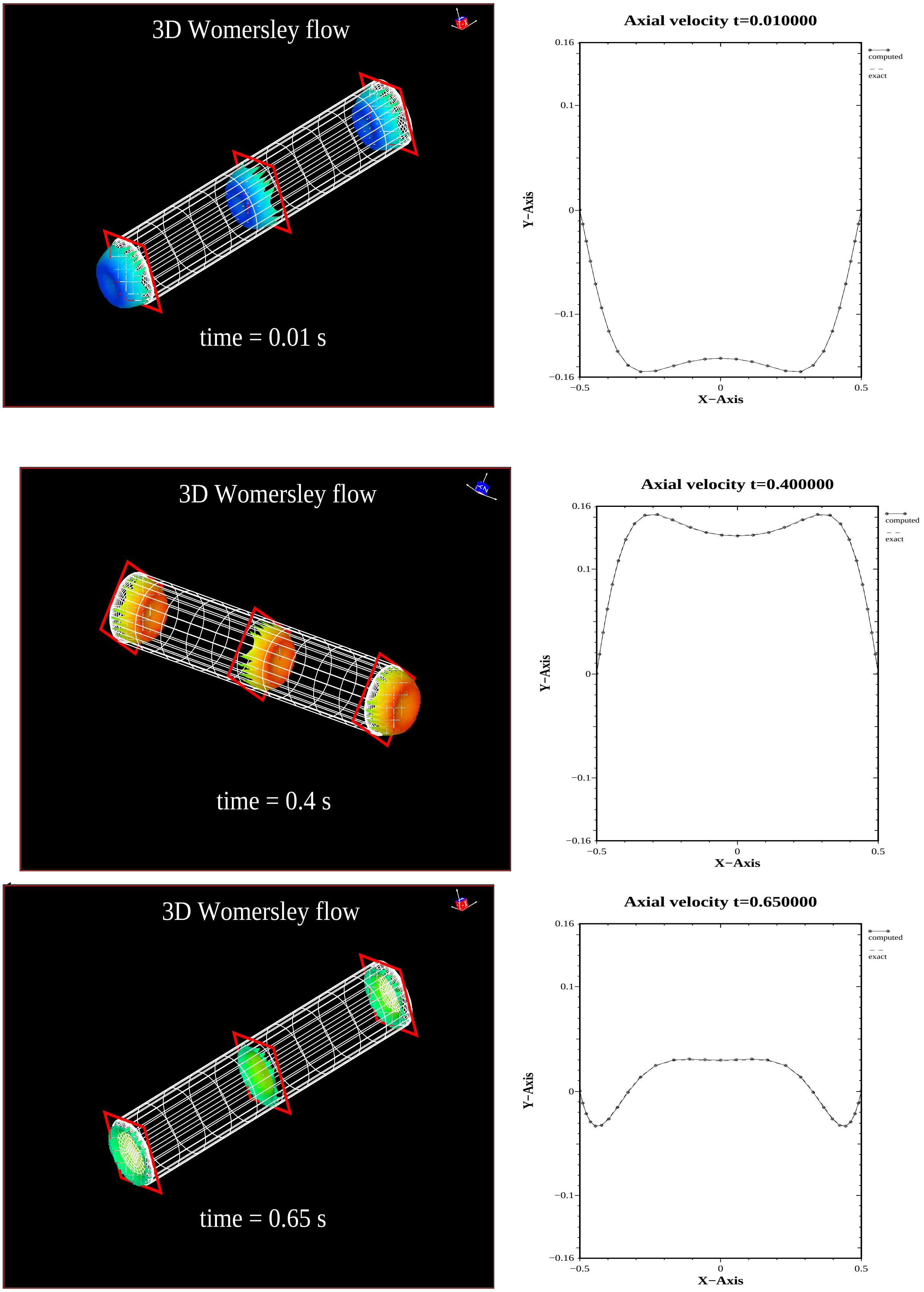

Figure 2.26: 3D numerical solution obtained imposing the flux of the Womersley solution at the outflow section.

2.4.1 Coupling 3D and 0D models

We wish to represent the whole circulatory system by an electric circuit except on a specific region Ω, where blood flow is modelled by the Navier-Stokes equations, as illustrated in Sect. 2.3.1.

Here, the compliance of the local vascular district is neglected for the sake of simplicity, hence Ω is constant in time. Let us assume that the network faces the district Ω by capacitors C_i ($i = 1, \dots, \overline{n}$) as shown in Figure 2.27. In particular, we put in evidence the representation in terms of a network of the vascular regions in the immediate neighborhood of the 3D model. In [31] these parts of the lumped network have been called the *bridging regions*. In this picture, we have three bridging regions corresponding to the three inflow/outflow of Ω. The mean pressure and the flow rate through each artificial section Γ_i of Ω ($i = 1, 2, 3$) are denoted by P_i and Q_i. We will set $\mathbf{Q} = (Q_i)_{i=1,2,3}$, where $Q_i(t) = \int_{\Gamma_i} \mathbf{u} \cdot \mathbf{n} d\boldsymbol{\gamma}$.

The Navier-Stokes equations and the lumped network are actually coupled by means of interface conditions involving, in general, the flow rates and the mean pressure values in the bridging regions. More precisely, we denote by $\mathbf{y} \in \mathbb{R}^m$ the state vector of the circuit at hand, and, for the sake of notation, we will suppose that the first $\overline{n} = 3$ state variables y_i ($i = 1, 2, \overline{n} = 3, \overline{n} < m$) correspond to the interface pressures $p_i(t)$. Due to the specific lumped representation of the bridging regions, the mean pressures on the Navier-Stokes interfaces are given[12] by $p_i(t)$, with $i = 1, \dots, \overline{n}$.

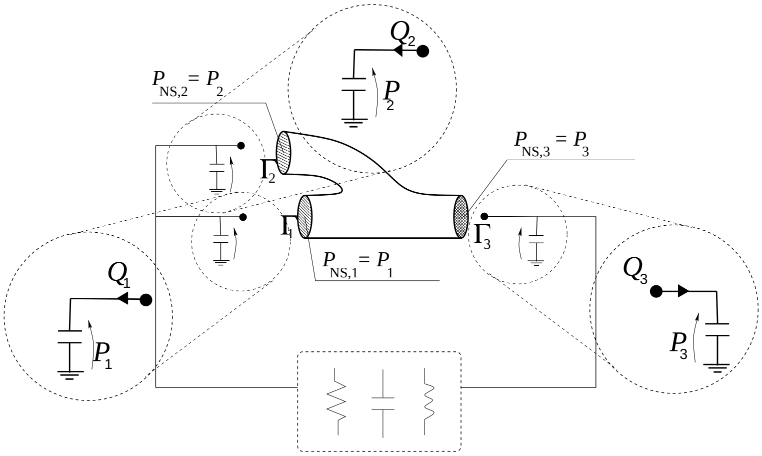

Figure 2.27: Scheme of coupling between the whole system and a local district. The lumped representation of the three bridging regions at the interfaces with the Navier-Stokes model is highlighted in the dashed circles. This representation is related to the interface conditions (2.42).

We will assume that the network is modelled by the differential system (2.15). In particular we set

$$\mathbf{r}(t) = \mathbf{r}_H(t) + \mathbf{b}(\mathbf{Q}(t)),$$

where, $\mathbf{r}_H$ accounts for the heart action, $\mathbf{b}$ involves the variables at the external terminals in

---

[12] In [31] it is considered a slighlty more general case, involving also a viscous resistance term at each interface.

such a way that

$$\begin{cases} b_i = \mathcal{C}_i Q_i & \text{for } i = 1, \dots, \overline{n} \\ b_k = 0 & \text{otherwise} \end{cases} \tag{2.40}$$

and $\mathcal{C}_i$ are suitable constants depending on the capacitors at the interfaces.

The coupled problem reads therefore:

Problem 2.1. *Given* $\mathbf{u_0} \in \mathbf{V}$ *(with* $div(\mathbf{u}_0) = 0$ *and* $\mathbf{y}_0 \in \mathbb{R}^m$*, find* $\mathbf{u} \in L^2(0, T; \mathbf{V})$ *and* $\mathbf{y} \in \mathbf{L}^\infty(0, T)$ *such that for every* $0 < t \leq T0, \forall \mathbf{v} \in V$ *and* $q \in M$*:*

$$\begin{cases} \dfrac{d\mathbf{y}}{dt} = A(\mathbf{y}, t)\mathbf{y} + \mathbf{r}_H(\mathbf{y}, t) + \mathbf{b}(\mathbf{F}(t)) \\ \left(\dfrac{\partial}{\partial t}\mathbf{u} + \mathbf{u} \cdot \boldsymbol{\nabla}\mathbf{u}, \mathbf{v}\right) + \nu(\boldsymbol{\nabla}\mathbf{u}, \boldsymbol{\nabla}\mathbf{v}) - (p, div(\mathbf{v})) + \sum_{i=0}^{n} P_i < \phi_i, \mathbf{v} > = < \mathbf{f}, \mathbf{v} >, \\ (q, div(\mathbf{u})) = 0, \end{cases} \tag{2.41}$$

with $\mathbf{y}(0) = \mathbf{y}_0$*,* $\mathbf{u}|_{t=0} = \mathbf{u}_0$*, where, as stated above, the first* $\overline{n} = 3$ *entries of the state vector* $\mathbf{y}$ *correspond to the interface pressures, in such a way that the mean pressures at the interface boundaries* Γ_i *are given by:*

$$P_{NS,i}(t) = P_i(t) = y_i(t) \quad i = 1, \dots, \overline{n} \tag{2.42}$$

and, by definition, the entries of the vector $\mathbf{F}$ *are given by:*

$$Q_i(t) = \int_{\Gamma_i} \mathbf{u} \cdot \mathbf{n} d\gamma \quad i = 1, \dots, \overline{n}. \tag{2.43}$$

In particular, prescription of (2.42) and (2.43) amounts to prescribe the continuity of (mean) pressures and fluxes at the interfaces. We are essentially coupling a lumped representation of the circulation (apart the local district) with the do-nothing formulation of the mean pressure drop problem (2.25). In the present case, the boundary mean pressure are not given, but are state variables of the lumped model to be computed. However, from the previous Section we know that if we suppose that the state variables of the 0D system are known, correspondingly the Navier-Stokes subproblem is well-posed. Similarly, if we suppose that the velocity is known in the local domain Ω, so that, in particular, the flow rates Q_i are known, also the 0D model can be solved. The heterogeneous multiscale problem is therefore given by coupling subproblems which are separately well posed. It is reasonable to expect that the global multiscale model is well posed. This well posedness has been proved in [31] starting from classical fixed point techniques:

Proposition 2.2. *If the initial data* $\mathbf{y}_0$ *and* $\nabla \mathbf{u}_0$ *are smooth and small enough, then , there exists a time interval* $0, \widetilde{T}$ *in which there exists at least a solution of problem (2.41).*

Numerical coupling For the numerical treatment of the coupled model described in the previous Section, we propose an iterative approach based on the splitting of the whole Problem 2.1

into its basic components, the ODE system from one hand and the Navier-Stokes equations (in the do-nothing formulation suited for the mean pressure drop problem) form the other one.

Let us introduce a partition $0 = t^0 < t^1 < \cdots < t^N = T$ of the time interval $(0, T)$ into N subintervals (t^n, t^{n+1}) with length $\Delta t = t^{n+1} - t^n$ for $n = 0, \ldots, N-1$ and a finite decomposition of the local domain Ω. We discretize the Navier-Stokes system by the finite element method for space variables and by a semi-implicit fractional step scheme for time advancement (see [29]). Let us denote with $N_{\mathbf{V}}$ and N_P the number of velocity and pressure nodes. In particular, we denote by x_j the nodal values of velocity ($j = 1, \ldots, N_{\mathbf{V}}$) and pressure ($j = N_{\mathbf{V}} + 1, \ldots, N_{\mathbf{V}} + N_P$), then set $\mathbf{x} = [x_j]_{j=1,\ldots,N_{\mathbf{V}}+N_P}$. The ordinary differential system associated to the systemic network is solved by a finite difference scheme. Denoting again with $\mathbf{y}$ the state vector of the lumped system, the fully discrete (algebraic) unsplit problem obtained after space and time discretizations reads:

$$\begin{bmatrix} \mathcal{N}_1 & \mathcal{F}_{NET,1} \\ \\ \mathcal{F}_{NS,1} & \mathcal{M}_1 \end{bmatrix} \begin{bmatrix} \mathbf{y}^{n+1} \\ \\ \mathbf{x}^{n+1} \end{bmatrix} = \begin{bmatrix} \mathcal{N}_2 & \mathcal{F}_{NET,2} \\ \\ \mathcal{F}_{NS,2} & \mathcal{M}_2 \end{bmatrix} \begin{bmatrix} \mathbf{y}^{n} \\ \\ \mathbf{x}^{n} \end{bmatrix} + \begin{bmatrix} \mathbf{g} \\ \\ \mathbf{0} \end{bmatrix} \tag{2.44}$$

where $\mathbf{y}^{n+1} = \mathbf{y}(t^{n+1})$, $\mathbf{x}^{n+1} = \mathbf{x}(t^{n+1})$, $\mathbf{y}^n = \mathbf{y}(t^n)$, $\mathbf{x}^n = \mathbf{x}(t^n)$. Moreover:

1. $\mathcal{N}_1 = \mathcal{N}_1(\mathbf{y}^{n+1}, t^{n+1})$, $\mathcal{N}_2 = \mathcal{N}_2(\mathbf{y}^n, t^n) \in \mathbb{R}^{m \times m}$ arise from the discretization of the terms $\dfrac{d\mathbf{y}}{dt}$ and $A(\mathbf{y}, t)\mathbf{y}$, respectively, in the lumped model,
2. $\mathbf{g} = \mathbf{g}(t^n, t^{n+1}) \in \mathbb{R}^m$ corresponds to the approximation of vector $\mathbf{r}_H(t)$ in equation (2.41),
3. $\mathcal{F}_{NET,1}, \mathcal{F}_{NET,2} \in \mathbb{R}^{m \times (N_{\mathbf{V}}+N_P)}$ are due to the discretization of $\mathbf{b}(Q_{up,i}(t), Q_{dw,j}(t))$, accounting for the interface conditions for the systemic submodel,
4. $\mathcal{M}_1 = \mathcal{M}_1(\mathbf{x}^{n+1}, t^{n+1})$, and $\mathcal{M}_2 = \mathcal{M}_2(\mathbf{x}^n, t^n) \in \mathbb{R}^{(N_{\mathbf{V}}+N_P)\times(N_{\mathbf{V}}+N_P)}$ follow from the approximation of the Navier-Stokes submodel,
5. $\mathcal{F}_{NS,1}, \mathcal{F}_{NS,2} \in \mathbb{R}^{(N_{\mathbf{V}}+N_P)\times m}$ are related to the treatment of the pressure interface conditions according to the do-nothing approach.

Since we are coupling a heterogeneous problem, it is to be expected that matrix of system (2.44) is ill conditioned. Therefore, there is no numerical convenience in adopting a monolithic approach for the solution. We adopt an iterative approach by splitting the solution of the global problem into the separate solving of the systemic and the local subproblems. More precisely, denote by k the index of iterations, and by $\mathbf{y}^{n+1}_{(k)}$ and $\mathbf{x}^{(n+1)}_{(k)}$ the approximate solutions at t^{n+1} at the k^{th} iteration. Then, let $\mathbf{y}_{(0)} = \mathbf{y}^n$, $\mathbf{x}_{(0)} = \mathbf{x}^n$ be the starting values, and set $\widetilde{\mathcal{N}}_{(k)} = \mathcal{N}_1(\mathbf{y}^{n+1}_{(k)}, t^{n+1})$, $\widetilde{\mathcal{M}}_{(k)} = \mathcal{M}_1(\mathbf{x}^{n+1}_{(k)}, t^{n+1})$, $\widetilde{\mathbf{b}}_{1,(k)} = \mathcal{N}_2(\mathbf{y}^n, t^n)\, \mathbf{y}^n +$ $\mathcal{F}_{NET,2}\mathbf{x}^n + \mathbf{g}(\mathbf{y}^n, \mathbf{y}^{n+1}_{(k)})$, $\widetilde{\mathbf{b}}_2 = \mathcal{F}_{NS,2}\mathbf{y}^n + \mathcal{M}_2(\mathbf{x}^n, t^n)\mathbf{x}^n$. Then, system (2.44) can be solved by the following block Gauss-Seidel scheme (we drop the index $n+1$ for sake of simplicity)

$$\left\{ \begin{array}{lcl} \widetilde{\mathcal{N}}_{(k)}\mathbf{y}_{(k+1)} & = & \widetilde{\mathbf{b}}_{1,(k)} - \mathcal{F}_{NET,1}\mathbf{x}_{(k)} \\ \\ \widetilde{\mathcal{M}}_{(k)}\mathbf{x}_{(k+1)} & = & \widetilde{\mathbf{b}}_2 - \mathcal{F}_{NS,1}\mathbf{y}_{(k+1)} \end{array} \right. \qquad k = 0, 1, 2, \ldots \tag{2.45}$$

Observe that in the iterative approach, we are actually solving alternatively the lumped parameters model, having assigned $Q_{up,i}^{(k)}$ and $Q_{dw,i}^{(k)}$ and the Navier-Stokes mean pressure problem, where the interface pressures $P_{up,i}^{(k+1)}$ and $P_{dw,i}^{(k+1)}$ are prescribed by the previous network computation. The (possible) converged solution will be obviously the solution of (2.44). As it is well known, the convergence property of this iterative procedure depends on the spectral radius of the iteration matrix $\widetilde{\mathcal{M}}_{(k)}^{-1}\mathcal{F}_{NS,1}\widetilde{\mathcal{N}}_{(k)}^{-1}\mathcal{F}_{NET,1}$.

In particular, if we solve the lumped parameters model by the forward Euler method

$$\mathbf{y}^{n+1} = (I + \Delta t\, A(\mathbf{y}^n, t^n))\,\mathbf{y}^n + \Delta t\,\mathbf{r}(\mathbf{y}^n, t^n) + \Delta t\,\mathbf{b}(\mathbf{x}^n)$$

then, $\widetilde{\mathcal{N}}$ is independent of k and it is given by the identity matrix I, $\mathcal{N}_2(\mathbf{y}^n, t^n) = I + \Delta t\, A(\mathbf{y}^n, t^n)$ and $\mathcal{F}_{NET,1} = 0$. In that case, the left hand side matrix in (2.44) is lower triangular and just one iteration in (2.45) is enough for the convergence, i.e. $\mathbf{y}^{n+1} = \mathbf{y}_{(1)}$, $\mathbf{x}^{n+1} = \mathbf{x}_{(1)}$. Thus $\mathbf{y}^{n+1}$ and $\mathbf{x}^{n+1}$ satisfy:

$$\left\{\begin{array}{rcl} \mathbf{y}^{n+1} & = & \widetilde{\mathbf{b}}_1 \\ \\ \widetilde{\mathcal{M}}\mathbf{x}^{n+1} & = & \widetilde{\mathbf{b}}_2 - \mathcal{F}_{NS,1}\mathbf{y}^n. \end{array}\right.$$

This scheme is illustrated in Figure 2.28.

The choice of an explicit method for the solution of the lumped submodel is justified by the experimental evidence that the consequent stability bound is less restrictive than the one arising from the semi-implicit treatment of the Navier-Stokes problem. In the numerical results of Sect. 2.5, for the time steps required by the Navier-Stokes solver, the forward Euler method turned out to be actually stable and computationally efficient. However, for more complex problems related to biomedical applications this method could result unstable unless for time step sizes unacettably too small. In these cases, the use of an implicit method in an iterative framework should be considered.

Remark 2.7. *Different splittings: The role of the interface conditions in the splitting procedure is naturally driven by the specific topology of the network at the interfaces. In our case, the interface flow rates are not state variables of the lumped system, and, therefore, they are well suited to play the role of a forcing term for the ordinary differential system. However, depending on the choice of the bridging regions, the matching between the network and the Navier Stokes system could be pursued, for instance, by interchanging the role of flux and pressure at the interfaces. When splitting the coupled problem, we should suppose that the flow rates are provided to the Navier-Stokes system by the network, which in turn receives pressure data. For instance, in the network configuration of Fig. 2.29, the interface pressure is not a state variable of the lumped system, so it is a good candidate for being a forcing term of the ordinary differential system, provided by the Navier-Stokes solution. On the other hand, the interface flow rates, which in the electric analogy correspond to the current at the interfaces and are state variables for the system, become boundary data for the Navier-Stokes problem. In this case, we formulate a net flux problem for the Navier-Stokes model, to be faced according to the Lagrange multiplier approach. The coupled problem can be recasted in the form (2.44) and the iterative procedure (2.45) can be applied as well.*

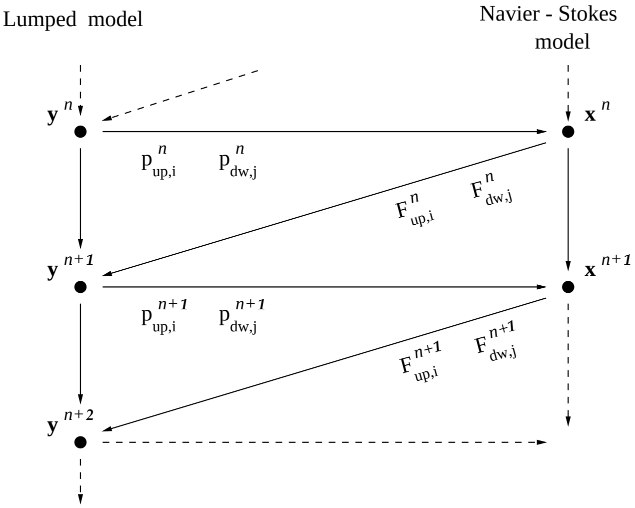

Figure 2.28: Numerical scheme adopted to solve the coupled problem (Forward Euler).

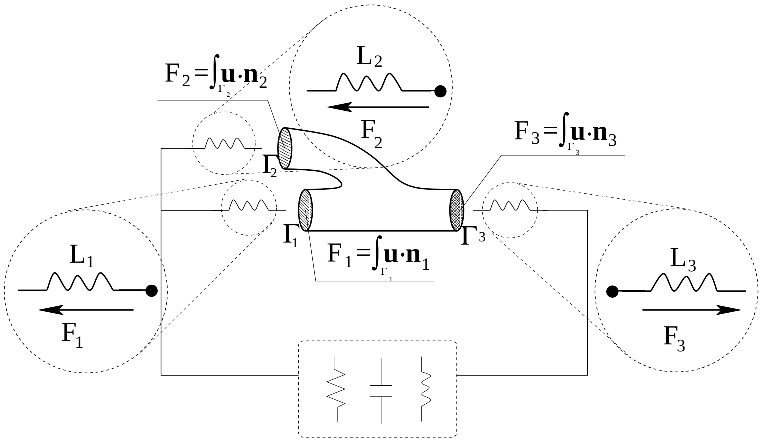

Figure 2.29: Scheme of coupling between the whole system and a local district where the bridging regions are given by inductors.

Remark 2.8. *Multiscale and Domain Decomposition Methods (DDM): In the last years, numerical methods for solving complex real problems in scientific computing by means of* domain decomposition techniques *have received great attention: as a recent reference, we quote [30]. On the hardware side, this is motivated by the fact that parallel architectures are now available that make it really effective the numerical solution of complex problems exploting parallel computing. Numerical techniques for the solution of problems by subdomain to be associated to a single processor or a cluster of processors are therefore of increasing interest. On the modeling side, the numerical approach to problems of increasing complexity quite naturally compell the identification of simpler "subproblems" that can be solved separately from the others, in order to setting up more effective numerical algorithms. Among the others possible examples, we quote fluid-structure interaction problems in hemodynamics, both at the mechanical and biochemical level (see [23], [49], [33], [32]).*

In our framework, it is reasonable to assimilate the flux data to (mean) Dirichlet *data, since they refer to the velocity field, while (mean) pressure data can be assimilate to* Neumann *condition, since they refer to the pressure, i.e. to the normal stress tensor which is a natural condition for the classical variational formulation of the Navier-Stokes equations. In this respect, the iterative algorithms presented above (and the ones that will be introduced for the 3D-1D coupling) can be considered an extension of the* Dirichlet-Neumann substructuring iterative method, *widely adopted in the context of DDM. This link can provide suggestions for setting up some improvements in the algorithms, exploting the theoretical framework of DD.*

2.4.2 Coupling 1D and 3D models

In this Section we illustrate how to carry out a multiscale coupling between 3D models still based on the Navier-Stokes equations and the 1D models introduced in [10]: for more details, see [7]. Since we are still dealing with a reduced model, involving mean quantities and the pointwise Navier-Stokes model, we will have still to handle "defective" data problems, according to the strategies illustrated in Sect. 2.3. In particular, here we will consider a compliant 3D domain, so that specific interface conditions will be needed by the differential problem associated to the vessel wall description. Moreover, the mathematical hyperbolic nature of 1D models will require a careful treatment of the interface conditions, based on a characteristics analysis (see [10], Sect. 3.2.1).

Let us focus this problem on an example. Consider two domains Ω_{3D} and Ω_{1D} as in Fig. 2.30. In the first, we solve the 3D fluid-structure model while in the second we consider a simplified 1D model.

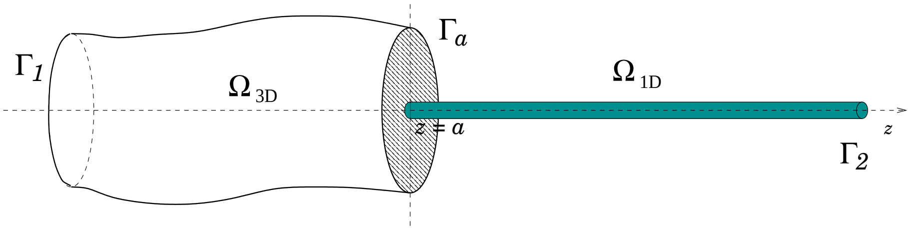

Figure 2.30: Coupling a 3D model with a 1D model

More precisley, in Ω_{1D} we assume equations (2.2), while in Ω_{3D} we consider the equations:

$$\begin{cases} \dfrac{\partial}{\partial t}\mathbf{u} + \mathbf{u}\cdot\boldsymbol{\nabla}\mathbf{u} - \dfrac{1}{\rho}\mathrm{div}(\mathbf{T}(\mathbf{u},p)) = 0 \\ \mathrm{div}(\mathbf{u}) = 0 \end{cases} \quad \text{in } \Omega, \tag{2.46}$$

where $\mathbf{T}(\mathbf{u},p) = -p\mathbf{I} + \mu\boldsymbol{\nabla}\mathbf{u}$ is the stress tensor.

For the sake of simplicity, a simplified structure model used in the case of 2D fluid simulations (see Fig. 2.31), which is derived for a cylindrical configuration (*generalised string* model) is considered[13]; see [28].). Let

$$\Gamma_w^0 = \{(r,\theta,z): \quad r = R_0,\, 0 \le z \le L,\, 0 \le \theta < 2\pi\}$$

be a cylindrical reference surface of radius R_0; we neglect the longitudinal and angular displacement while the radial displacement $\eta_r = \eta_r(t,\theta,z)$ is given by

$$\rho_w h \frac{\partial^2 \eta_r}{\partial t^2} - kGh\frac{\partial^2 \eta_r}{\partial z^2} + \frac{Eh}{1-\xi^2}\frac{\eta_r}{R_0^2} - \gamma\frac{\partial^3 \eta_r}{\partial z^2 \partial t} = f(t,\theta,z) \tag{2.47}$$

Here, h is the wall thickness, R_0 is the arterial reference radius at rest; k is the so called *Timoshenko shear correction factor*; G the *shear modulus*; E the Young modulus, ξ the Poisson ratio; ρ_w the wall volumetric mass, γ is a viscoelastic parameter and, finally f is an external forcing term.

Model (2.47) is basically derived from the equations of linear elasticity for a cylindrical tube with small thickness, under the hypotheses of plane stresses and membrane deformations (i.e negligible elastic bending terms). The term $kGh\dfrac{\partial^2 \eta_r}{\partial z^2}$ accounts for shear deformations ([34]) while the term $\gamma\dfrac{\partial^3 \eta_r}{\partial z^2 \partial t}$ introduces a viscoelastic behaviour.

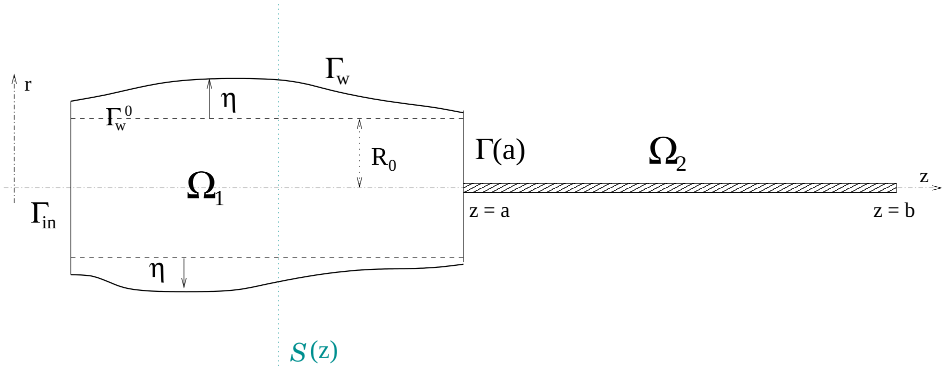

Figure 2.31: Coupled 2D/1D problem. On the left, the 2D model (Ω_1), where Γ_w represents the arterial wall and η the wall displacement with respect to the reference configuration Γ_w^0. On the right, the 1D model (Ω_2) defined on the interval $a \le z \le b$.

Then, matching conditions at Γ_w may be provided as follows:

$$\begin{cases} \mathbf{u} = \dot{\boldsymbol{\eta}} \\ -\mathbf{T}\cdot\mathbf{n} - p_{ext}\mathbf{n} = \boldsymbol{\Phi} \end{cases} \quad \text{on } \Gamma_w, \tag{2.48}$$

---

[13] More accurate models for 3D fluid simulations will be considered in Sect. 2.5

where p_{ext} is a given external pressure, $\mathbf{\Phi} = f\mathbf{e}_r$ is the forcing term acting on the wall and $\mathbf{n}$ is the outward unit vector to Γ_w.
The first of (2.48) guarantees the perfect adherence of the fluid to the structure while the second one states the continuity of the stresses at the interface (according to the action and reaction principle).

Both fluid and structure equations must be supplied with initial conditions (resp. on Ω_{3D} and Γ_w^0) and boundary conditions (resp. on γ_1 and $\partial\Gamma_1$).

Moreover, we assume that on the right side of Γ_a the 1D model supplies the quantities $A(a^+)$, $Q(a^+)$, $P(a^+)$ and $\overline{u}(a^+) = Q/A$. In particular, we consider that the pressure $P(a^+)$ is a function of the area $\psi(A)$, accounting for a (simplified) structure model (see [10], Sect. 3). We define, then, the same quantities also on the left side of Γ_a as

$$A(a^-) = |\Gamma_a|; \qquad \overline{u}(a^-) = \frac{1}{|\Gamma_a|}\int_{\Gamma_a} \mathbf{u}\cdot\mathbf{n}\, d\sigma$$
$$\overline{p}(a^-) = \frac{1}{|\Gamma_a|}\int_{\Gamma_a} p\, d\sigma; \qquad Q(a^-) = |\Gamma_a|\,\overline{u}(a^-).$$

Moreover, we assume that at Γ_a the wall displacement is a function of the section area,

$$\boldsymbol{\eta}|_{\Gamma_a} = \mathbf{g}(A(a^-)), \tag{2.49}$$

being $\mathbf{g}$ a given function. For instance, we assume that Γ_a is a circle in which case $\boldsymbol{\eta}|_{\Gamma_a} = \left(\sqrt{A(a^-)/\pi} - R_0\right)\mathbf{e}_r$.

Similarly to the 3D-0D coupling, where we have forced the continuity of the interface pressures and fluxes, we have to specify which kind of interface conditions will be associated the heterogeneous model.

A priori, it is reasonable to look for the continuity of the following quantities at the interface Γ_a:

[A] area : $A(a^-) = A(a^+)$

[B] mean pressure : $\bar{p}(a^-) = \bar{p}(a^+)$

[C] flux : $Q(a^-) = Q(a^+)$

[D] entering characteristic : $\overline{u}(a^-) + 2\sqrt{\frac{2}{\rho}}\left(\sqrt{\overline{p}(a^-) - p_{ext} + p^*} - \sqrt{p^*}\right) = W_1(a^+)$

In the 1D model viscous terms have been (partially) neglected, so that, similarly to what done for the 0D-3D coupling, the variable P can be either interpreted as a mean pressure or as a mean normal stress. The condition [B] may therefore be replaced with the continuity of the averaged normal stress, i.e. $\bar{\sigma} = \overline{\mathbf{T}\cdot\mathbf{n}\cdot\mathbf{n}}$. Analogously, the characteristic variable on the left hand side can be calculated using the averaged normal stress in place of the mean pressure. We have therefore two conditions alternative to B and D, respectively. Namely,

[B1] averaged normal stress : $\bar{\sigma}(a^-) = \bar{p}(a^+)$

[D1] char. entering variable : $\overline{u}(a^-) + 2\sqrt{\frac{2}{\rho}}\left(\sqrt{\bar{\sigma}(a^-) - p_{ext} + p^*)} - \sqrt{p^*}\right) = W_1(a^+)$

The coupled 3D-1D model will be stated by coupling the fluid-structure (2.46), (2.47) and the 1D equations (2.2) with the interface conditions that will generate well posed individual subproblems in Ω_{3D} (in the sense specified in Sect. 2.3), and Ω_{1D}. To this aim, four different set of coupling conditions can be considered:

- **Interaction Model 1**: conditions A, B, D
  Note that B and D imply the continuity of $\overline{u}$. With the further continuity of A we obtain that of Q, thus also C is satisfied.
- **Interaction Model 2**: conditions A, C, D
  Note that A and C imply the continuity of $\overline{u}$. If we further add D we have the continuity of $\bar{p}$. Thus also B is satisfied.
- **Interaction Model 3**: conditions A, B1, D1
  Note that B1 and D1 imply the continuity of $\overline{u}$ and , with the continuity of A we obtain that of Q. Thus also C is satisfied.
- **Interaction Model 4**: conditions A, C, D1
  Note that A and C imply the continuity of $\overline{u}$. If we further add D we have the continuity of $\bar{\sigma}$. Thus also B1 is satisfied.

Sub-domain iterations between 1D and 3D models

As already pointed out for the 3D-0D coupling, the coupled problem (with one of the interface conditions specified above) is expected to be ill conditioned. We will consider, therefore, iterative splitting methods based on the separate solution of the two subproblems:

The 1D problem with condition D (or D1) as boundary condition at the interface and an absorbing condition on the right end (i.e. zero entering characteristic variable). With this choice, the hyperbolic system (2.2) is well posed (see [7]).

The 3D fluid-structure problem with condition A as boundary condition for the structure equation and condition B (B1) or C, depending on which interaction model we consider, as boundary condition for the Navier-Stokes equations.

With these choices the structure problem turns out to be well posed, while conditions B or C lead respectively to a mean pressure or to a net flux problem, to be solved as illustrated in Sect. 2.3.

We can then iterate between the two sub-domains to get the global solution at each time step.

Here, we illustrate an example, referring to the interaction Model 3. The iterative algorithm reads as follows: given the solution of the coupled problem (let's say $\mathbf{u}^n$, p^n, $\boldsymbol{\eta}^n$ for the 3D model and Q^n, A^n for the 1D one) and setting $\mathbf{u}_0^{n+1} = \mathbf{u}^n$, $p_0^{n+1} = p^n$, and $\boldsymbol{\eta}_0^{n+1} = \boldsymbol{\eta}^n$

1. solve the 1D model (2.2) with condition D1 at the interface, evaluating the characteristic variable $W_1(a^+)$ as a function of $\mathbf{u}_0^{n+1}$, p_0^{n+1}, $\boldsymbol{\eta}_0^{n+1}$; we then obtain a solution Q_1^{n+1} and A_1^{n+1} and at $z = b$ absorbing boundary conditions based on characteristic analysis;
2. solve the 3D problem with boundary conditions A and B1 at the interface, evaluating $A(a^-)$ and $\bar{\sigma}(a^-)$ as functions of A_1^{n+1} and Q_1^{n+1}. We obtain a solution $\mathbf{u}_1^{n+1}$, p_1^{n+1}, $\boldsymbol{\eta}_1^{n+1}$.

We iterate until the coupling conditions are satisfied within a fixed tolerance. In this case, the second step requires the solution of a mean pressure drop problem.

Another possibility, devising to a net flux problem for the Navier-Stokes equations is the following: set $\mathbf{u}_{(0)} = \mathbf{u}^n$, $p_{(0)} = p^n$, and $\eta_{(0)} = \eta^n$ and for $k = 0, 1, \ldots$

1. solve the 1D model (2.2) imposing at $z = a$ $A_{(k+1)}(a)$ as a function of the pressure $p_{(k)}$ and at $z = b$ absorbing boundary conditions based on characteristic analysis. We obtain $Q_{(k+1)}$ in Ω_2;

2. we solve then the fluid-structure 2D problem imposing on $\Gamma(a)$ for the Navier-Stokes equations the defective condition

$$\int_{\Gamma(a)} \mathbf{u}_{(k+1)} \cdot \mathbf{e}_z = Q_{(k+1)}(a)$$

   and for the structure at $z = a$

$$\eta_{(k+1)}(a) = \frac{1}{2} A_{(k+1)}(a) - R_0.$$

   We obtain $\mathbf{u}_{(k+1)}$, $p_{(k+1)}$, $\eta_{(k+1)}$ in Ω_1.

We iterate until the coupling conditions are satisfied within a fixed tolerance and we finally set the solution at time t^{n+1} equal to the converged value. For more details about these algorithms, see [7] and [8].

Numerical results both for 2D and 3D simulations based on these methods are presented in the next Section.

2.5 Numerical results

In this final Section we will show some applications of the methods presented. More details and results can be found in [27], [7], [8], [31], [19].

2.5.1 An analytical test case

Assume the circuit shown in Figure 2.21 as a completely lumped parameter decsription of the circulation, providing a reference solution at the systemic level. The network is modelled by a nonlinear system in the form (2.15). Coronary arterial pressure and flow rate (i.e. the pressure applied to C_{CA} and the flux flowing through R_Ω and L_Ω), obtained for the global network by means of the forward Euler discretization, are plotted in Figure 2.32. Let us denote with Ω the simple bipole consisting of L_Ω and R_Ω and representing a specific cylindrical district in the coronary arterial branch. Our aim is to model blood flow behaviour in Ω by the Navier-Stokes equations coupled with the lumped description of the remaining network. In particular, a pressure drop is prescribed between the artificial sections of the district at hand by the state of the systemic lumped submodel, while the flow rates at the interfaces represent the forcing terms for the whole circulatory system (see Fig. 2.34).

The coupled model has been solved by the explicit numerical method described in Sect. 2.4.1. The time step is set to $\Delta t = 10^{-4}$ s and it is dictated by the stability constraints of

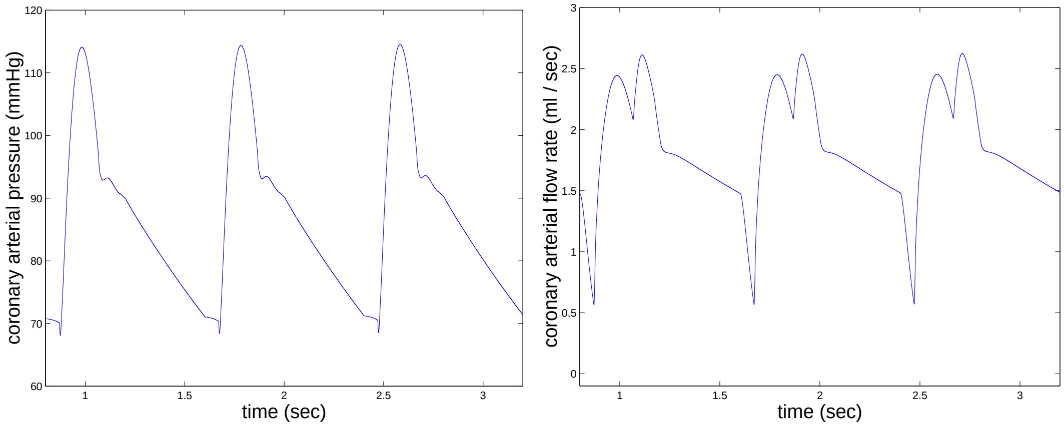

Figure 2.32: Numerical simulation of the global network, representing the whole vascular system, by means of the forward Euler method (time step $\Delta t = 10^{-4}$s). On the left, the coronary pressure. On the right, the coronary flow rate.

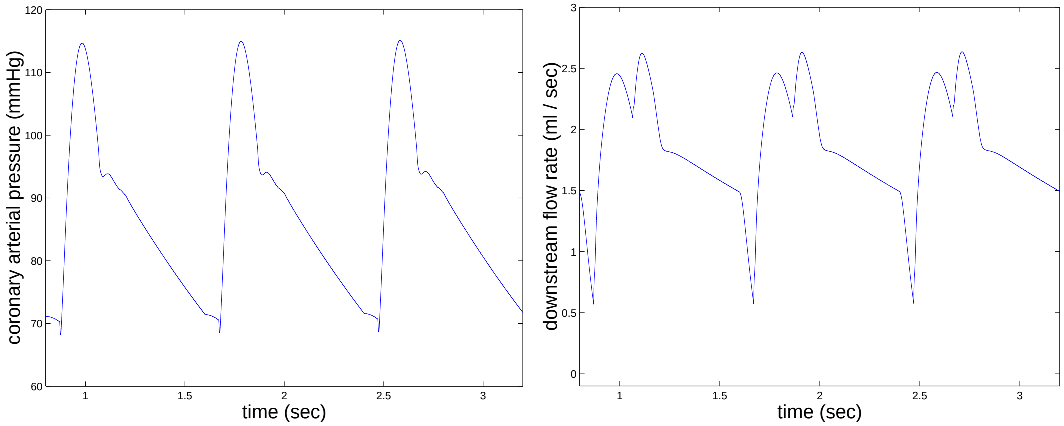

Figure 2.33: Coronary arterial pressure and of flow rate through the downstream of Ω, obtained by means of the coupled scheme.

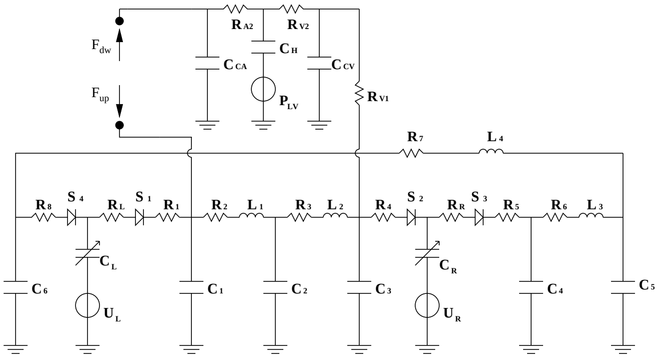

Figure 2.34: Representation of the particular electric network used as a systemic model to be coupled to the Navier-Stokes equations in the cylindrical domain Ω.

the local Navier-Stokes solver, which is based on a semi-implicit treatment of the nonlinear convective term. Larger time steps would be allowed by a fully implicit treatment of this terms. The coronary arterial pressure and the flow rate through the downstream section of Ω, evaluated by means of the coupled scheme, are shown in Figure 2.33. Since we have substituted a part of a network with the corrispondent description in term of Navier-Stokes equations, for consistency of the heterogeneous model with a pure lumped parameters description of the circulation, the presence of a local accurate submodel does not have to modify significantly the results at the systemic level. This is exactly what we obtain numerically by comparing Figure 2.32 and Figure 2.33. However, the heterogeneous model is able to compute accurately the velocity and pressure fields in the district of interest. Notice that in this preliminar test case, when solving the local subproblem, we are actually considering a mean pressure drop problem on a 2D pipe, having a periodic pressure drop. In this case, the analytical velocity solution of the Navier-Stokes problem is given by the Womersley profiles[14] (see [42]). Therefore, we can verify the correctness of the detailed results, by a comparison with the analytical solution. Table 2.3 in different instants of the heart beat illustrates the results of the comparison, with a satisfactory agreement.

A similar test case has been carried out also in a 3D case with a simplified network model. Also in this case, the results are in good agreement with the expected Womersley profiles (see Fig. 2.35) (3D computations have been carried out with FIDAP(TM)).

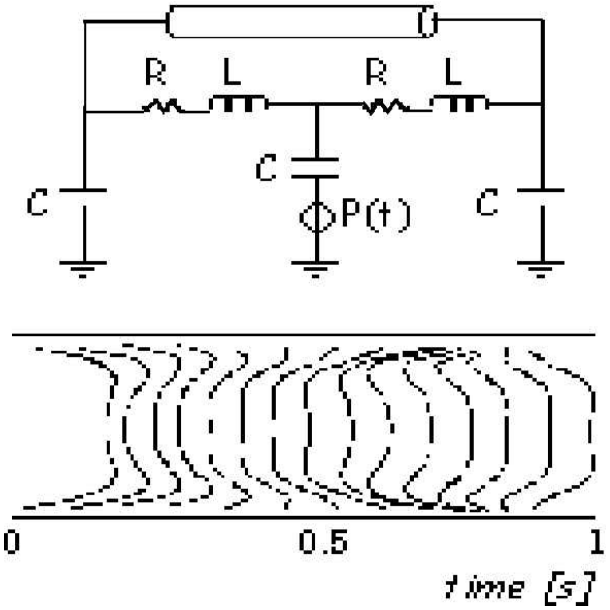

Figure 2.35: Simplified multiscale 3D-0D test case, leading to Womersley profiles.

Table 2.3: Relative errors in the Womersley test case during a heart beat. The heart beat period is fixed to 0.8 s.

$\dfrac{t}{T_{beat}}$	$\dfrac{\lvert\lvert \mathbf{u}_{Womersley} - \mathbf{u}_{computed} \rvert\rvert}{\lvert\lvert \mathbf{u}_{Womersley} \rvert\rvert}$
0.125	6.0 $\times 10^{-4}$
0.250	2.9 $\times 10^{-6}$
0.375	2.4 $\times 10^{-5}$
0.500	1.4 $\times 10^{-4}$
0.625	1.1 $\times 10^{-6}$
0.750	1.7 $\times 10^{-6}$
0.875	1.8 $\times 10^{-6}$
1.000	2.5 $\times 10^{-6}$

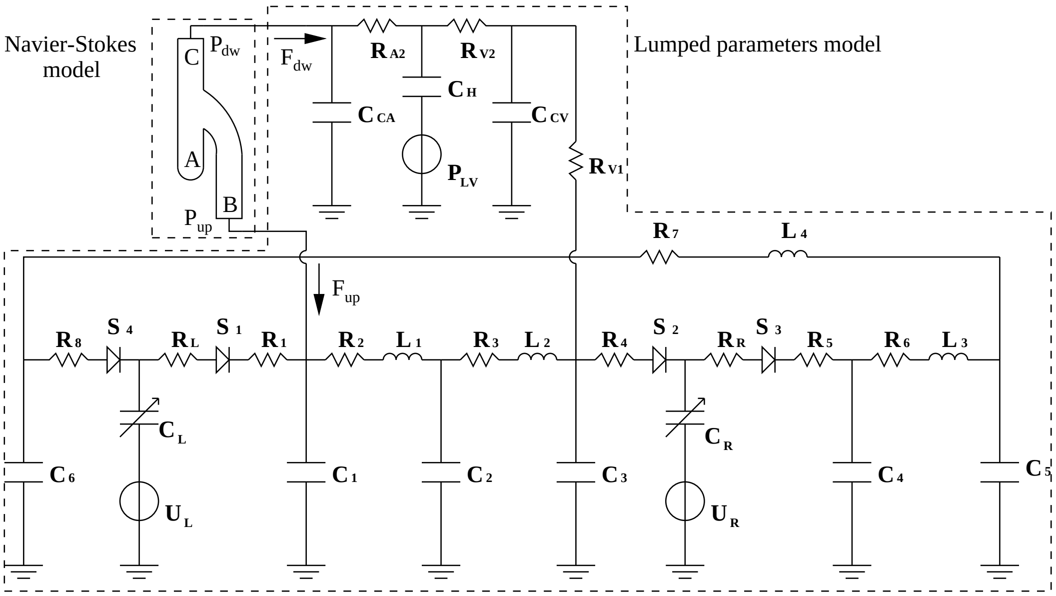

Figure 2.36: Representation of the particular electric network used as a systemic model to be coupled to the Navier-Stokes equations in a completely occluded coronary by-pass.

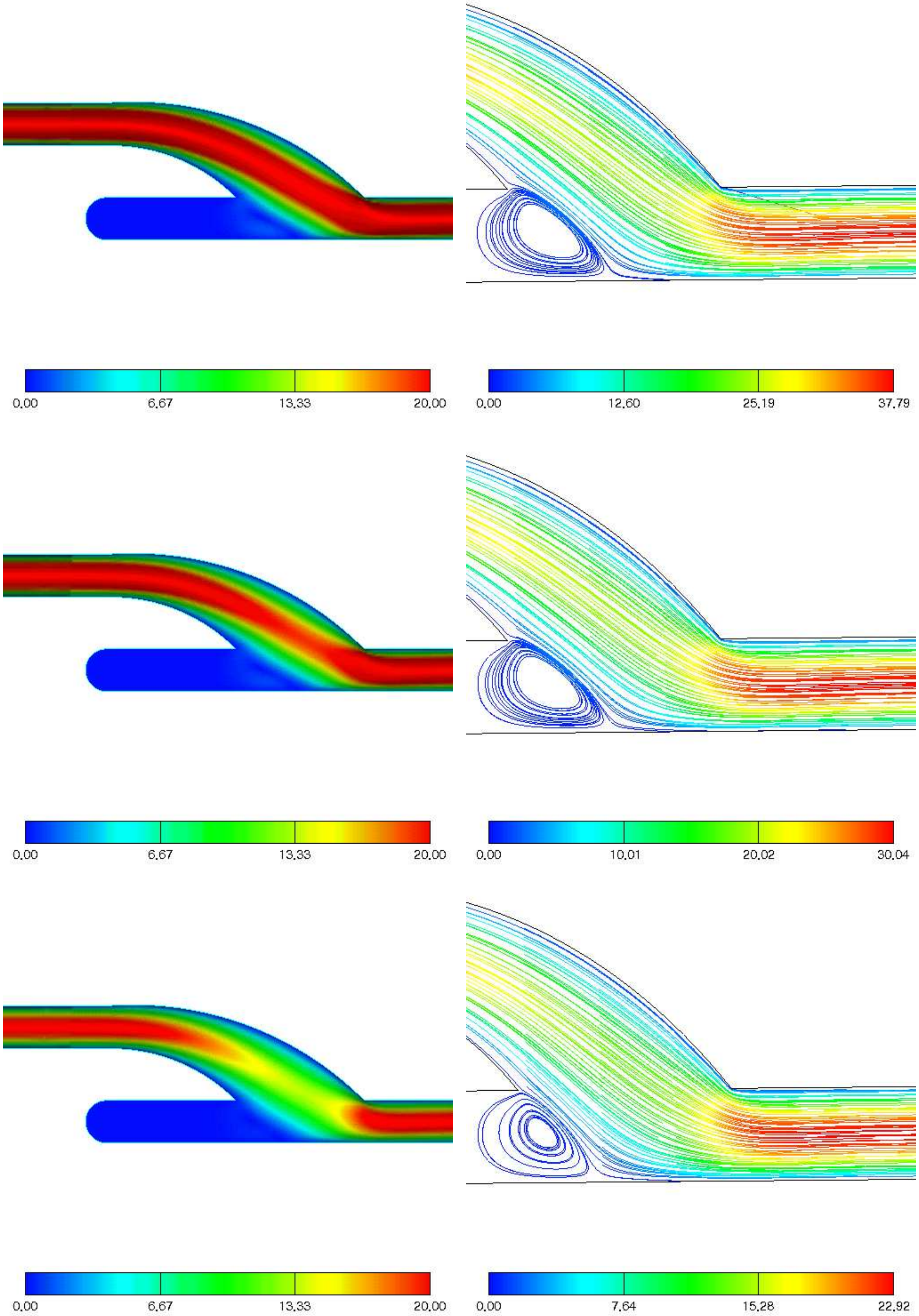

Figure 2.37: Velocity and contour and streamlines plots in the totally occluded vessel for different times: a quarter of a beat (top), half a beat (middle) and end of a beat (bottom).

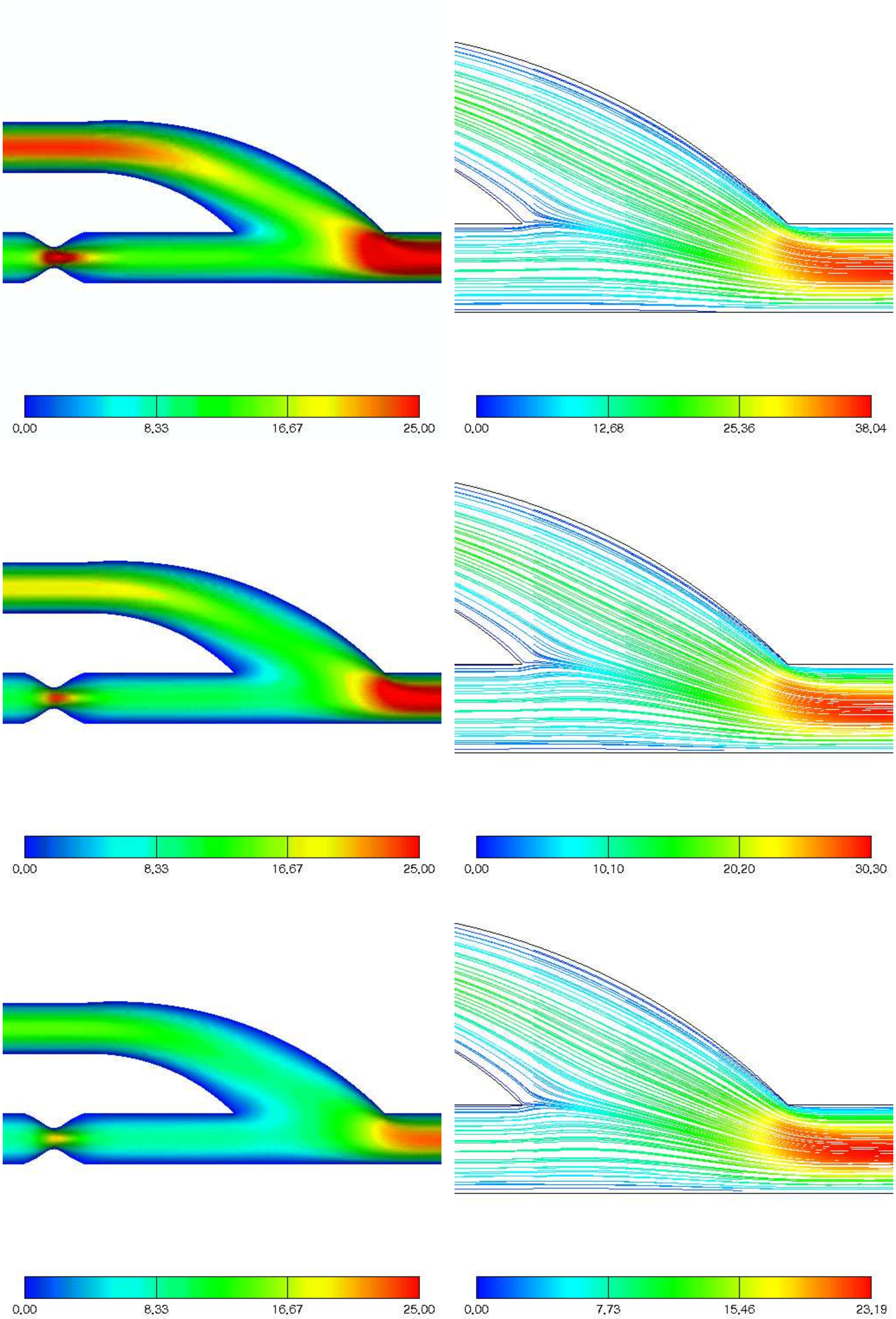

Figure 2.38: Velocity contour plots and streamlines in the partially occluded vessel for different times: a quarter (top) of a beat, half a beat (middle) and end of a beat (bottom).

2.5.2 A simplified by-pass anastomosis

Pressure drop problem for Navier-Stokes equations

Let Ω be a coronary by-pass of a completely occluded vessel (Figure 2.36). A Dirichlet condition is prescribed at the lower upstream branch A of Ω; more precisely, a null velocity condition is assigned on this section, simulating the complete occlusion. The coupling between the local accurate submodel and the systemic one is based on the formulation given in Problem 2.1 (where the interfaces between lumped and Navier-Stokes model are denoted by B and C). Velocity contour plots and streamlines for different times in a beat are shown in Figures 2.5.2, respectively. More precisely, the illustrated sequences refer to a quarter of a beat, half a beat and the end of a beat.

A coupled local-systemic investigation of blood flow dynamics has been carried out also in a partially occluded coronary by-pass (see Fig. 2.39). In this case, we consider also upstream section A as an interface between local and systemic model. Velocity contour plots and streamlines are illustrated in Figures 2.38 as in the previous case. The downstream flow rates computed by the coupled solver are shown in Figure 2.40 (top) for both cases of complete and partial occlusion. By comparing them with the one shown in Figure 2.33, observe that the downstream flow rates are obviously the same in both cases. The relevance of these results is not related to the specific test case (which is indeed a 2D simplification of a real morphology) and to the quantitative determination of the variable involved here. However, the heterogeneous numerical coupling allows a correct determination of the fluid dynamical conditions of a district of interest accounting for the systemic circulation. Specifically, the quantitative determination of a district of interest is obtained *without* the prescription of any presumed boundary conditions. The interface data for the district of interest are computed by the solver on the basis of the lumped model. For instance, in the numerical results illustrated here, it is possible to compute the distribution of the upstream fluxes between the two branches of the anastomosis as a function of the relevance of the stenosis and of the radius of the by-pass. In particular, the flux computed by the Navier-Stokes system is obviously totally carried by the by-pass in the completely occluded case, while in the partially occluded one (with a 60% reduction of the section) about 30% of the flow rate is carried by the stenosed vessel (see Fig. 2.40).

Net flux problem for the Navier-Stokes equations

This time, the by-pass anastomosis is associated to a network with a downstream inductance (see Fig. 2.41). The downstream flow rate is therefore a state variable of the lumped model and is prescribed, in the iterative splitting, as a boundary datum to the Navier-Stokes solver, following the Lagrange multiplier approach.

At the top of Figure 2.42 we show the flow rate and the pressure drop in the by-pass computed by the coupled system. The marks indicate the values at the times corresponding to the four snapshots of the fluid speed found in the lower part of the same figure.

Alltogether, these results illustrate that multiscale 2D(3D)-0D models with different network topologies (involving both pressure drop or net flux problems) can provide effective tools for the contemporary simulation of systemic and local hemodynamics.

---

[14] More precisely, since in this case the nonlinear term of the Navier Stokes problem vanishes, the analytical solution is the weighted superimposition of the Womersley profiles corresponding to the different frequencies of the Fourier development of the (periodic) pressure drop applied to the local subdomain by the network.

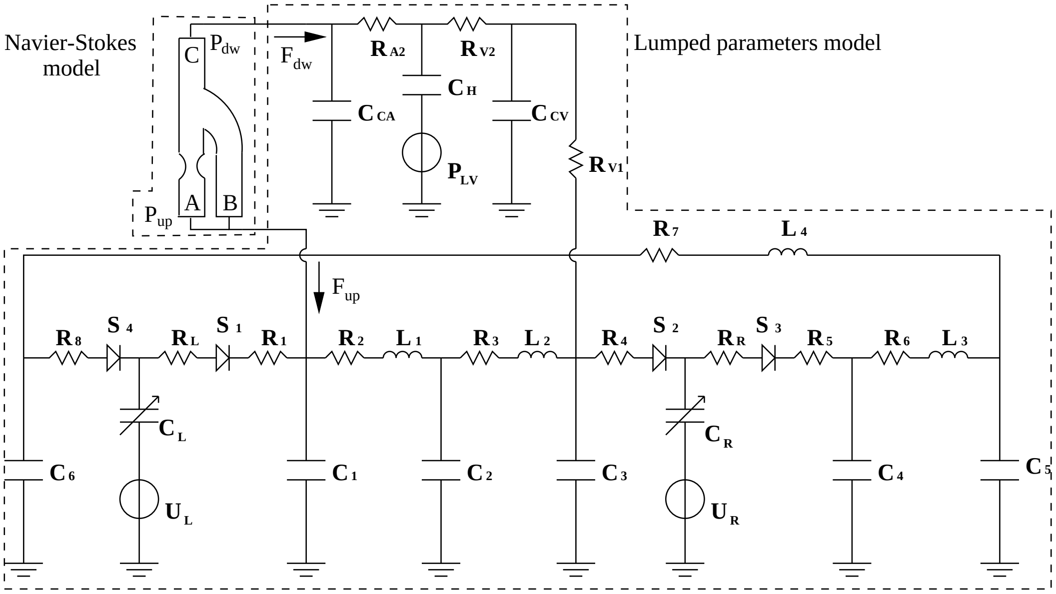

Figure 2.39: Representation of the specific electric network used as a systemic model to be coupled to the Navier-Stokes equations in the partially occluded coronary.

2.5.3 A 2D-1D coupling

Let us consider the domain illustrated in Fig. 2.31. In Ω_1 we solve (2.46), (2.47), (2.48) with boundary conditions on the interface Γ_a on the pressure or on the flow rates, according to the iterative subdomain algorithm selected. In Ω_2 we consider the one dimensional equation for the velocity flux Q and the vessel section area A (2.2) supplied with the algebraic relation $\bar{p} = \beta(A - A_0)$, A_0 being the reference area $A_0 = 2R_0$. The system is supplemented by initial conditions for $\mathbf{u}$ in Ω_1, A and Q in Ω_2 at $t = 0$.

The fluid-structure interaction problem has been discretized in space using $\mathbb{P}^1$-iso$\mathbb{P}^2$ finite elements for the fluid and P^1 elements for the structure. For time discretization, we have adopted an ALE formulation to account for the domain movement with an implicit Euler discretization for the fluid equations (faced with a Chorin-Temam like splitting scheme) and a Newmark scheme for the structure. System (2.2) has been discretized using a second-order Taylor-Galerkin scheme (Lax-Wendroff: see [10]) with a characteristic treatment of the boundary.

We have considered a rectangular domain of height $1cm$ and length $L = 6cm$. The fluid is initially at rest and an over pressure of 15mmHg ($2 \cdot 10^4\, dynes/cm^2$) has been imposed at the inlet for 0.005 seconds. The viscosity of the fluid is equal to $0.035\, poise$, its density is $1\, g/cm^3$, the Young modulus of the structure is equal to $0.75 \cdot 10^6\, dynes/cm^2$, its Poisson coefficient is 0.5, its density is $1.1\, g/cm^3$ and its thickness is $0.1\, cm$.

We have first simulated the fluid-structure interaction model without any coupling with the 1D reduced model. In this case, natural boundary conditions for the fluid (i.e. null normal stress) have been imposed on the outlet. Figures 2.43 show the fluid pressure and the domain deformation.

Observe that a pressure wave is generated (together with a deformation wave at the same velocity), which is reflected at the outflow section. Such a reflection is clearly a numerical side-effect due to the boundary conditions imposed at the outflow.

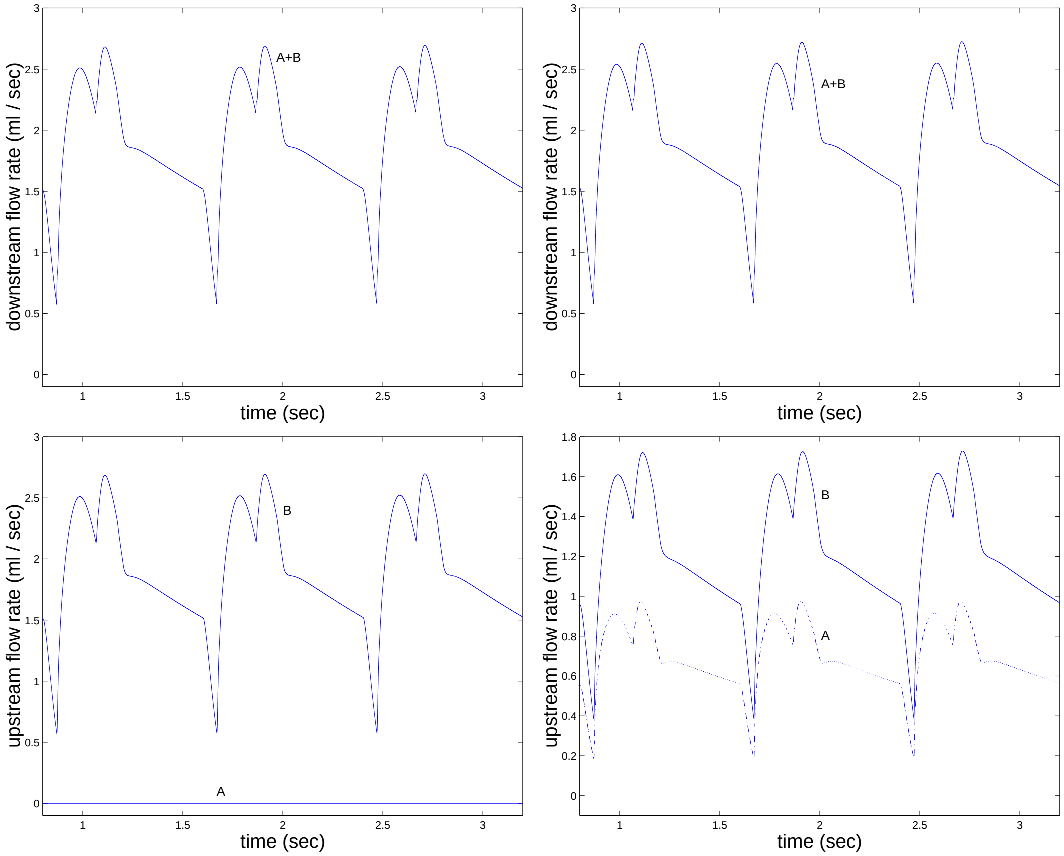

Figure 2.40: Top: downstream flow rates computed by the distributed solver in the case of completely (left) and partially (right) occluded vessel. Bottom: division of the upstream flow rates between the lower A and the upper B proximal sections in the case of complete (left) and partial (right) occlusion.

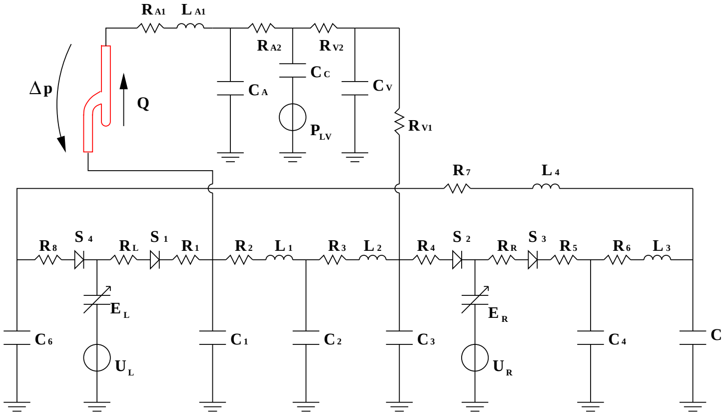

Figure 2.41: Lumped parameter model of the circulatory system coupled with a 2D description of a coronary by-pass with a

In Figures 2.44 we have in particular considered the coupling with the 1D reduced model at the outflow section. Concerning the coupling with the reduced 1D model, we have considered Model 3 described in section 2.4.2. We have made just one sub-iteration between 1D and 3D (2D) model at each time step. Here, the reflections are greatly reduced because the pressure wave is quite well absorbed by the 1D model.

A 3D-1D coupling

In the case of 3D fluid simulation a shell model, i.e. a 3D structure in which one dimension, the thickness, is much lower than the other ones has been considered. In particular we have considered the so-called *geometrically exact shell model* developed in [38, 39, 40]. The main unknowns are the mid-surface position of the shell and its normal vector at each point. Deformations are described without approximation on the geometry, even when large displacements are considered. This case has been simulated using the code SPECTRUM(TM).

Computations has been made on a cylindrical domain of radius $R_0 = 0.5cm$ and length $L = 5cm$, with the following physical parameters: fluid viscosity: $0.03\,poise$, fluid density: $1\,g/cm^3$, Young modulus of the structure: $3 \cdot 10^6\,dynes/cm^2$, Poisson coefficient: 0.3 and structure density: $1.2\,g/cm^3$. Again, an over-pressure of 10mmHg ($1.3332 \cdot 10^4\,dynes/cm^2$) is imposed at the inlet for 0.005 seconds.

As for the 2D model, the moving fluid domain is handled with an ALE formulation. In Fig. 2.46 and 2.46 the results of the simulations without and with the multiscale coupling are compared. As for the 2D case, spurious reflections on the downstream artificial boundary are strongly reduced in the multiscale framework.

In the case of fluid-structure interaction problems, the boundary conditions prescription at artificial boundaries is a crucial issue for the correctness of numerical simulation. These results show that the coupling between a 3D fluid-structure model and a 1D reduced model is an effective way to greatly reduce numerical reflections of the pressure waves.

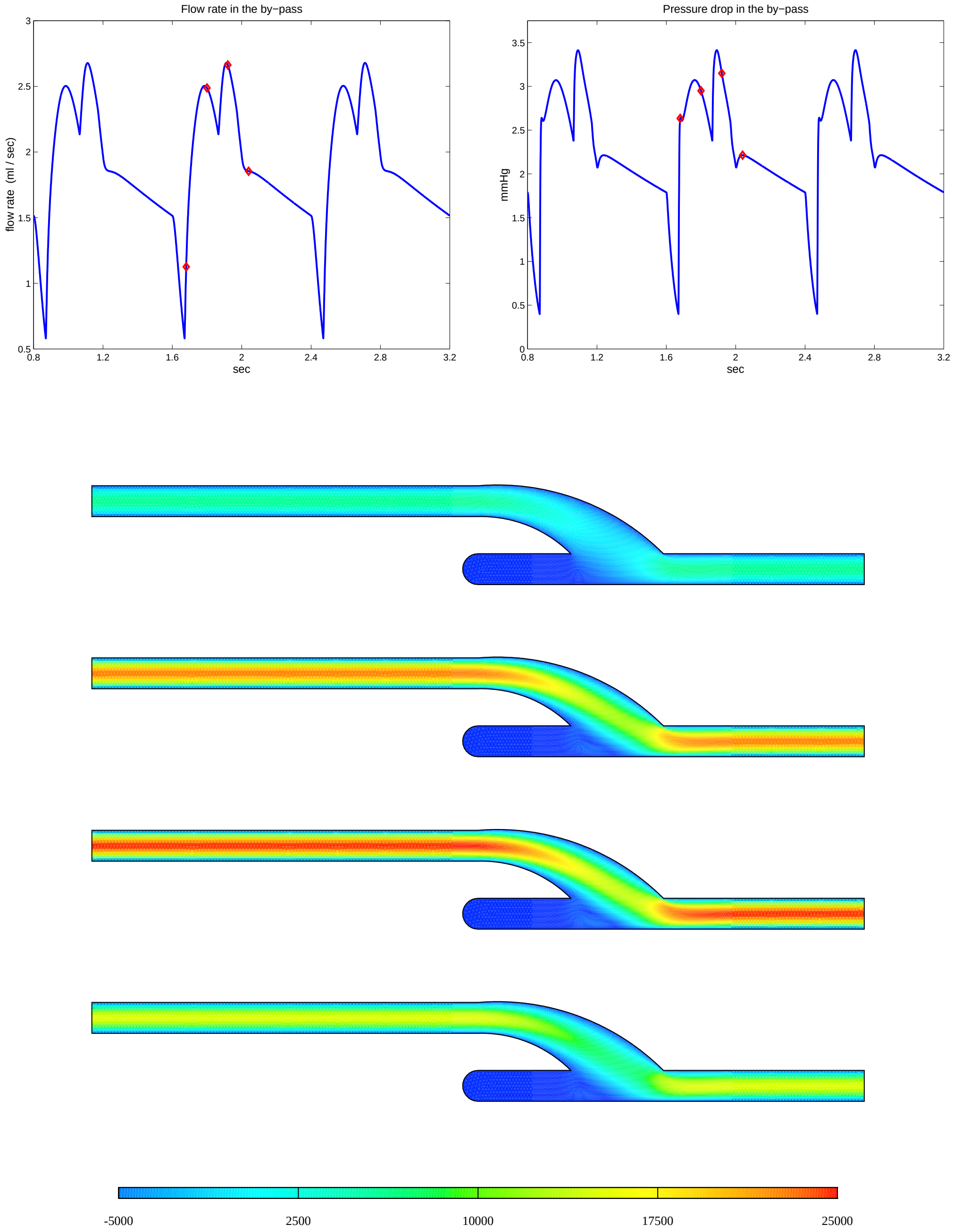

Figure 2.42: On the top: flow rate and pressure drop in the by-pass. On the bottom: fluid speed at $t = 1.68\,s, 1.8\,s, 1.92\,s, 2.04\,s$

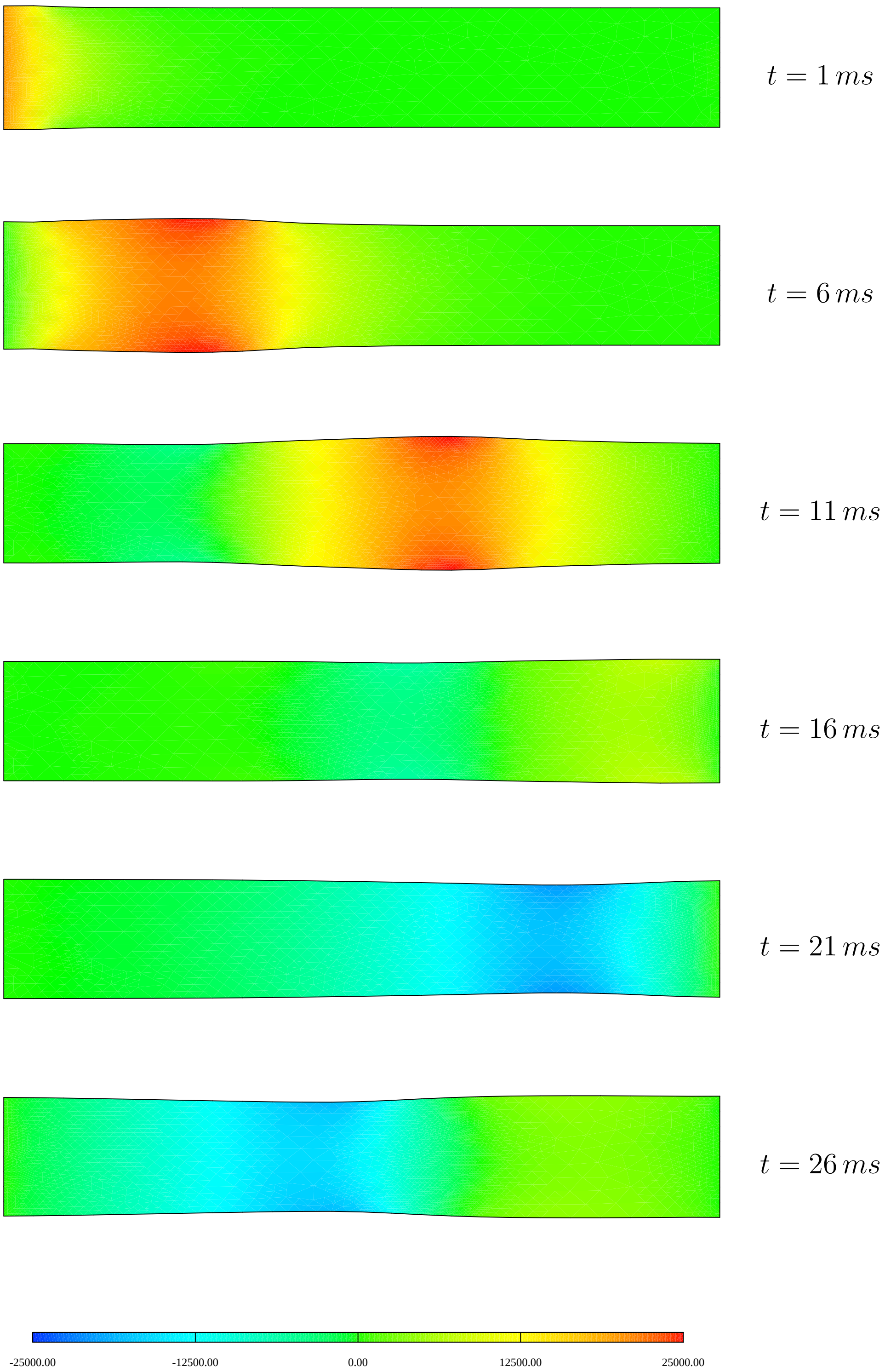

Figure 2.43: Pressure pulse entering at the *inflow* and homogeneous Neumann conditions at the *outflow*; 2D simulation. Solutions every $5\,ms$. Note how the pressure is reflected at the outflow boundary, giving rise to a backward travelling wave with negative amplitude.

2.5.4 A test case of clinical interest

Beyond the previous academic test cases, numerical results obtained in more realistic contexts, still based on the approach of the present work, can be found in [26] and in [19]. In these references the adoption of geometrical multiscale models has revealed very promising for analysing, by means of numerical simulations, the dynamics of flow patterns in morphologically complex vascular districts in the context of paediatric surgery. The proposed methodology was in particular applied to a reconstructive procedure, the systemic-to-pulmonary shunt, used in cardiovascular paediatric surgery to treat a group of complex congenital malformations. The 3-D model includes the shunt, the innominate artery (through which blood flows in) and the pulmonary, carotid and subclavian arteries (through which blood flows out), see Fig. 2.48. The lumped model is composed by different blocks describing the rest of the pulmonary circulation, the upper and lower body, the aorta, the coronary system and the heart (see Fig. 2.47 up).

The application to the systemic-to-pulmonary shunt, currently in progress, gives a clear idea of what can be obtained using the multiscale methodology. Figure 5 shows some preliminary results on local haemodynamics in a simplified model of the shunt. Velocity vector maps are reported at three different time steps of the pulsatile cycle. Blood flow in the innominate artery switches from forward to backward and forward again. In spite of such changes, the shunt flow remains directed towards the pulmonary arteries, which agrees with clinical data [20], [21]. The common approach in a stand-alone FEM model of the shunt would require to impose inlet velocity profiles and outlet total stress distributions, which could be time-dependent, but with a 'frozen' temporal history of the inlet velocity profile. With the adopted multiscale approach, i.e. using boundary conditions that account for the circulatory system, this was avoided and the inlet velocity profile reversal was correctly reproduced (see Fig. 2.47 and Fig. 2.48 for the complete computation of the shunt).

The prediction of both the local and the global haemodynamics after a surgical correction, leads to the quantification of pressure drops across the repaired region as well as to that of flow distribution into the major cardiovascular districts. The latter is an extremal important issue. Indeed, the insertion of a systemic-to-pulmonary shunt creates a pulmonary circulation in parallel to the systemic one. Survival after such an operation crucially depends on the balance between systemic and pulmonary blood flows which, in turn, are highly dependent on the fluid dynamics through the shunt. Numerical modeling can help the surgeon in the optimal choice of shunt placement and size.

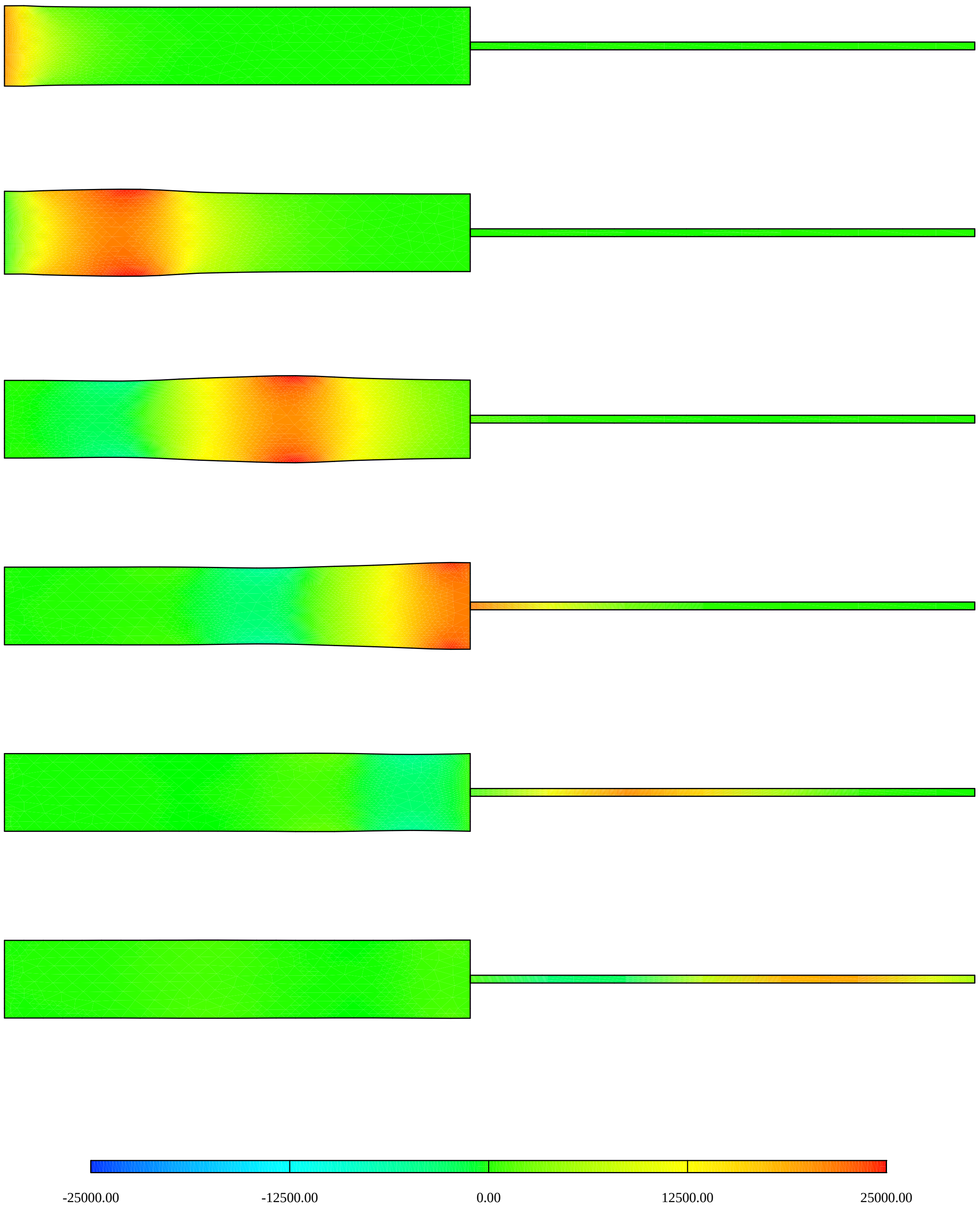

Figure 2.44: coupling 2D simulation with the 1D reduced model; solution every $5\,ms$. Note how the pressure wave exits the domain with almost no spurious reflections.

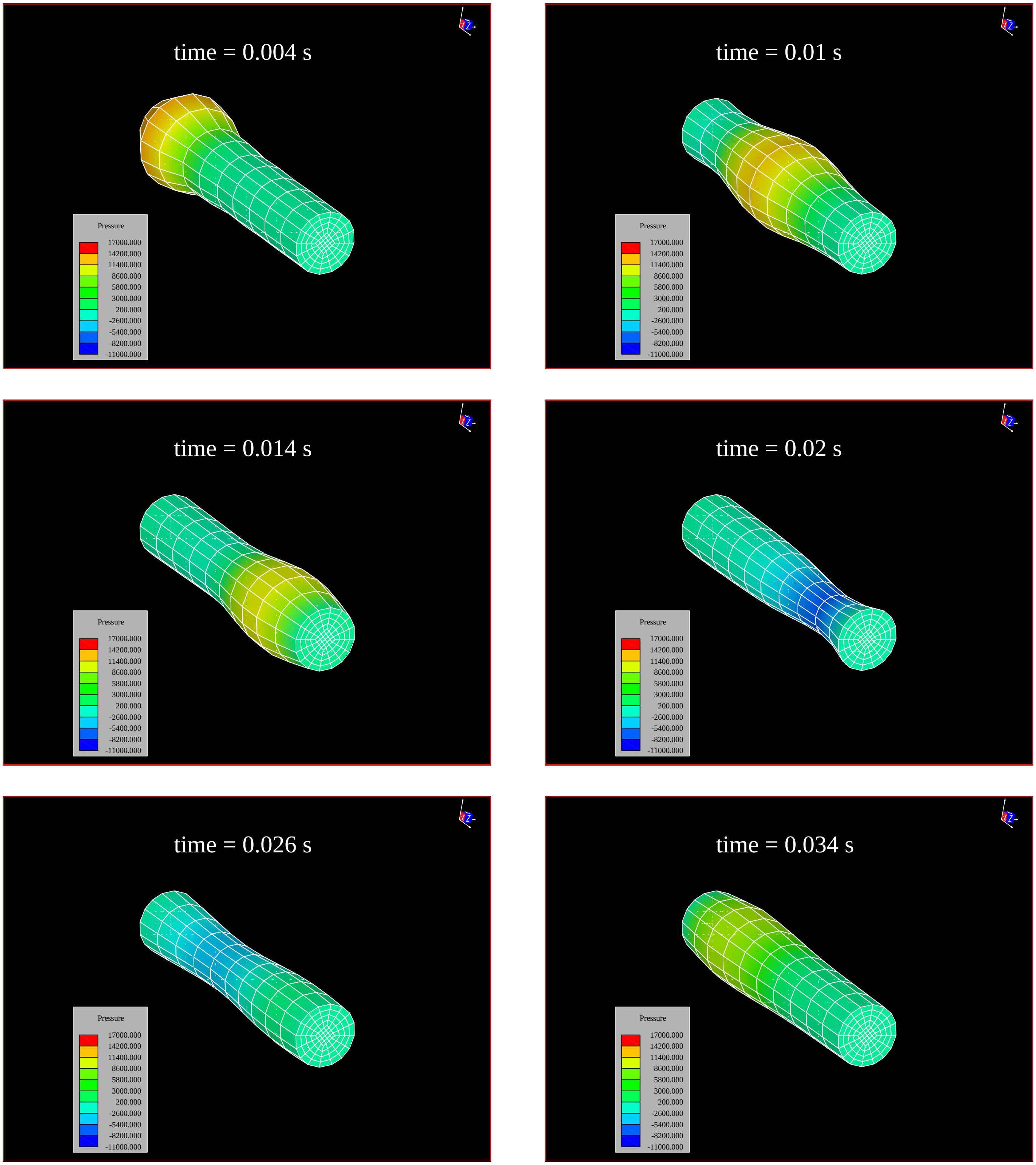

Figure 2.45: Pressure pulse entering at the *inflow* and homogeneous Neumann conditions at the *outflow*: 3D simulation with SPECTRUM(TM). The displacement of the structure has been magnified by a factor 10

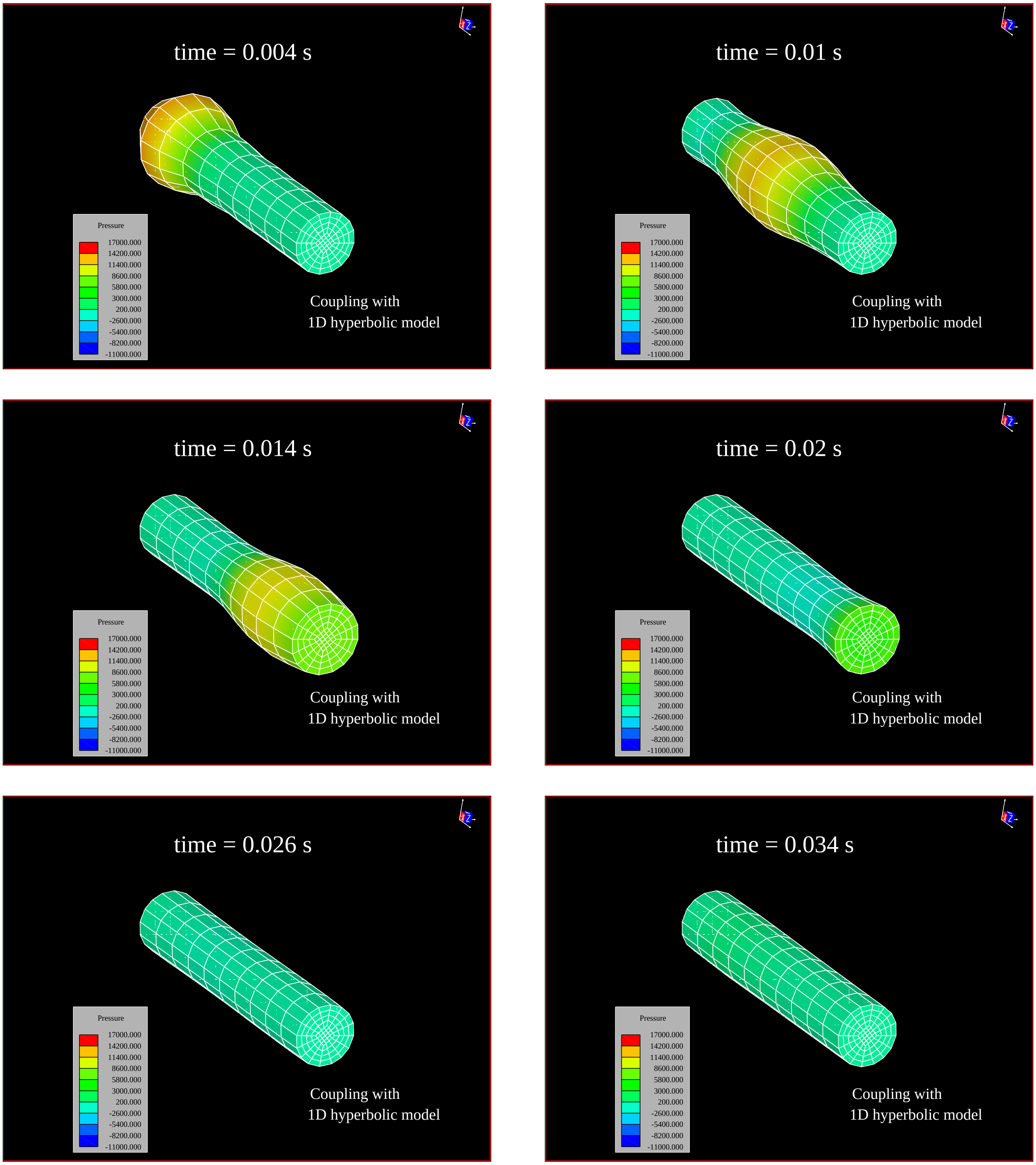

Figure 2.46: Coupling 3D SPECTRUM(TM) simulation with the 1D reduced model

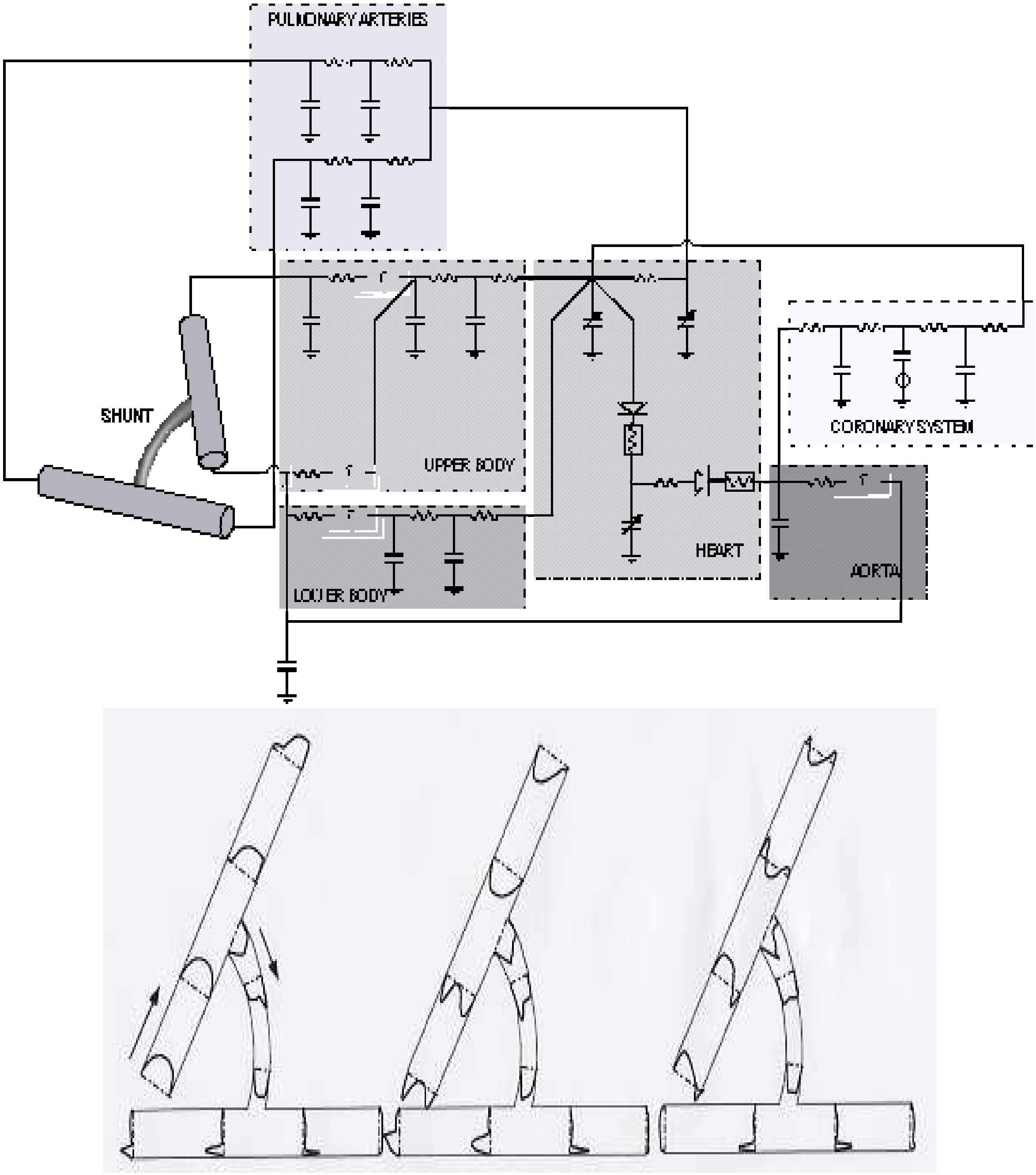

Figure 2.47: Simulation of the Norwood operation: velocity fields at different instants of the heart beat. Multiscale model and velocity profile in a simplified model of the shunt.

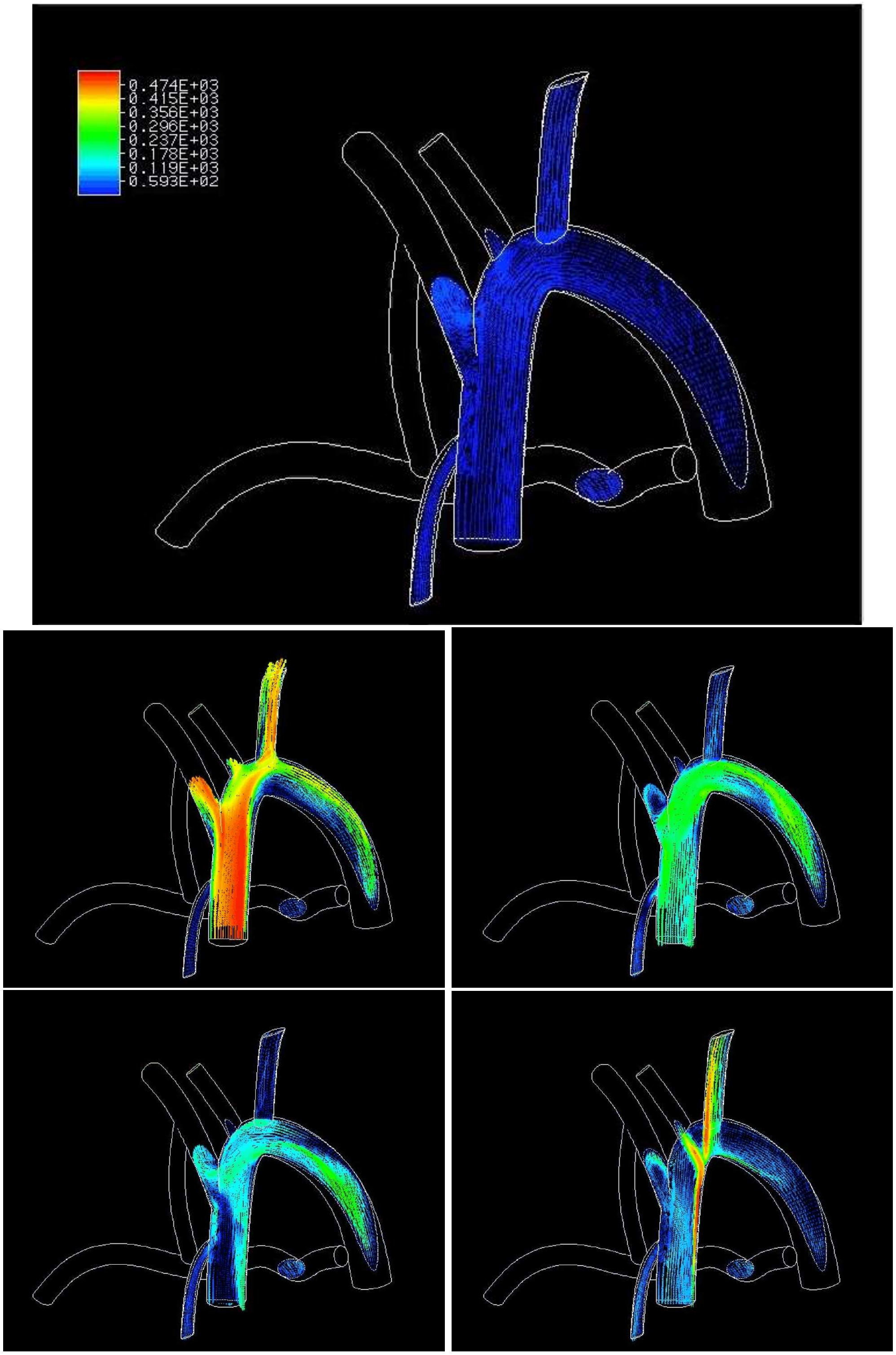

Figure 2.48: Simulation of the Norwood operation: velocity fields at different instants of the heart beat. These are the 3D results in the complete shunt. Thanks to the multiscale approach, it has been possible to compute physiological velocity profiles and secondary flow patterns which were not captured in previous simulations, based on the prescription of incorrect (even if realistic) essential boundary velocity data.

Bibliography

[1] G. Alì A. Bartel, and M. Gunther. Electrical RLC networks and diodes. Technical Report RT237/01, Istituto per le Applicazioni del Calcolo ”M. Picone”, Italian National Research Council, http://www.na.iac.cnr.it, 2001.

[2] J. P. Archie and R. P. Feldtman. Critical stenosis of the internal carotid artery. *Surgery*, 89:67–70, 1981.

[3] F. Brezzi and M. Fortin. *Mixed and Hybrid Finite Elements*. SSCM n. 5, Springer–Verlag, 1991.

[4] J. Bronzino, editor. *The Biomedical Engineering Handbook*, chapter 157: Compartmental Models of Physiologic Systems, by C. Cobelli and M.P. Saccomani, pages 2375–2385. CRC Press, 1999.

[5] J. Bronzino, editor. *The Biomedical Engineering Handbook*, chapter 158: Cardiovascular Models and Control, by W.D. Timmons, pages 2386–2403. CRC Press, 1999.

[6] G. D'Errico, A. Onorati, and G. Ferrari. An integrated 1d-2d fluid dynamic model for the predictions of unsteady flows in i.c. engine duct system. In *IMECH In. Conf. ”Computational and Experimental Methods in Reciprocating Engines*, 2000.

[7] L. Formaggia, J. F. Gerbeau, F. Nobile, and A. Quarteroni. On the coupling of 3d and 1d navier-stokes equations for flow problems in compliant vessels. *Comp.Math. Appl. Mech. Eng.*, 191:561–582, 2001.

[8] L. Formaggia, J. F. Gerbeau, F. Nobile, and A. Quarteroni. Numerical treatment of defective boundary conditions for the navier-stokes equation. *SIAM J Num Anal*, 40(1):376–401, 2002.

[9] L. Formaggia and A. Quarteroni. Mathematical modeling and numerical simulation of the cardiovascular system. MOX Rep. n. 1, http://mox.polimi.it, 2002. to appear in N. Ayache (ed.), ”Modeling of Living Systems”, Handbook of Numerical Analysis Series, Elsevier.

[10] L. Formaggia and A. Veneziani. One dimensional models for blood flow in the human vascular system. VKI Lecture Notes ”Biologic Fluid Dynamics”, 07-2003, 2003.

[11] Y.C. Fung. Mechanics of Soft Tissues. In R.Skalak and S. Chen, editors, *Handbook of Bioengineering*. McGraw-Hill, 1987.

[12] R. Glowinski and P. Le Tallec. *Augmented Lagrangian and Operator Splitting Methods in Nonlinear Mechanics*. Studies in Applied Mathematics. SIAM, Philadelphia, 1989.

[13] M.A. Helal. Derivation of closed-form expression for the cerebral circulation models. *J. Biomech.*, pages 103–118, 1994.

[14] J.G. Heywood, R. Rannacher, and S. Turek. Artificial Boundaries and Flux and Pressure Conditions for the Incompressible Navier–Stokes Equations. *International Journal for Numerical Methods in Fluids*, 22:325–352, 1996.

[15] F. Hoppensteadt and C. Peskin. *Mathematics in Life Sciences and Medicine*. Springer-Verlag New York, 1992.

[16] G.N. Jager, N. Westerhof, and A. Noordergraf. Oscillatory flow impedance in electrical analog of the arterial system. *Circ. Res.*, 16:121–133, 1965.

[17] J. Keener and J. Sneyd. *Mathematical Physiology*. Springer-Verlag New York, 1998.

[18] E. Krause. Modeling of the circulatory system. Lecture Notes of the VKI Course on Fluid Dynamics and Biological Flow, Course 04-1998, 1998.

[19] K. Laganà, G. Dubini, F. Migliavacca, R. Pietrabissa, G. Pennati, A. Veneziani, and A. Quarteroni. Multiscale modelling as a tool to prescribe realistic boundary conditions for the study of surgical procedures. *Biorheology*, 39:259–364, 2002.

[20] F. Migliavacca, G. Pennati, G. Dubini, R. Fumero, R. Poetrabissa, G. Urcelay, E.L. Bove, T. Y. Hsia, and M.R. de Leval. Modeling of the norwood circulation: efects of shunt size, vascular resistances, and heart rate. *Am. J. Physiology*, 280:H2076–H2086, 2001.

[21] F. Migliavacca, R. Yates, G. Pennati, G. Dubini, R. Fumero, and M.R: de Leval. Calculating blood flow from doppler measurements in the systemic-to-pulmonary artery shunt after the norwood operation: a method on computational fluid dynamics. *Ultrasound Med. Biol.*, 26:209–219, 2000.

[22] W.W. Nichols and M.F. O'Rourke. *Mc Donald's Blood Flow in Arteries*. Edward Arnold Ltd. - London, 1990. Third edition.

[23] F. Nobile. *Numerical approximation of fluid-structure interaction problems with applications to hemodynamics*. PhD thesis, Ecole Polytechnique Federeale Lausanne, 2001.

[24] A. Noordergraaf, H.B.K. Boom, and P.D. Verdouw. A human systemic analog computer. In A. Noordergraaf, editor, *1st Congr. Soc. for Ballistocardiographic Res.*, page 23, 1960.

[25] G. Pennati, F. Migliavacca, G. Dubini, R. Pietrabissa, and M.R. de Leval. A mathematical model of circulation in the presence of the bidirectional cavopulmonary anastomosis in children with a univentricular heart. *Med. Eng. Phys.*, 19(3):223–234, 1997.

[26] R. Pietrabissa, A. Quarteroni, G. Dubini, F. Migliavacca, A. Veneziani, and S. Ragni. From the global cardiovascular system down to the local blood motion: preliminary applications of a multiscale approach. In *Proceedings of ECCOMAS2000 Conference, Barcelona, (CDRom)*, 2000.

[27] A. Quarteroni, S. Ragni, and A. Veneziani. Coupling between lumped and distributed models for blood flow problems. *Comp. Vis. Science*, 4:111–124, 2001.

[28] A. Quarteroni, M. Tuveri, and A. Veneziani. Computational vascular fluid dynamics: problems, models and methods. *Comp. Vis. Science*, 2(4):163–197, 2000.

[29] A. Quarteroni and A. Valli. *Numerical Approximation of Partial Differential Equations*. Springer Verlag Series in Computational Mathematics n.23, 1994.

[30] A. Quarteroni and A. Valli. *Domain Decomposition Methods for Partial Differential Equations*. Oxford University Press, Oxford, 1999.

[31] A. Quarteroni and A. Veneziani. Analysis of a geometrical multiscale model based on the coupling of ode's and pde's for blood flow simulations. To appear in SIAM J Mult Mod Sim, 2003.

[32] A. Quarteroni, A. Veneziani, and P. Zunino. A domain decomposition method for advection-diffusion processes with application to blood solutes. *SIAM J Sci Comp*, 23(6):1959–1980, 2002.

[33] A. Quarteroni, A. Veneziani, and P. Zunino. Mathematical and numerical modeling of solutes dynamics in blood flow and arterial wall. *SIAM J Num An*, 39(5):1488–1511, 2002.

[34] H. Reismann. *Elastic plates: theory and application*. Wiley, New York, 1988.

[35] V.C. Rideout and D.E. Dick. Difference-differential equations for fluid flow in distensible tubes. *IEEE Trans. Biomed. Eng.*, BME-14(3):171–177, 1967.

[36] Y. Saad. *Iterative Methods for Sparse Linear Systems*. PWS Publishing Company, Boston, 1996.

[37] K. Sagawa, H. Suga, and K. Nakayama. Instantaneous pressure-volume ratio of the left ventricle versus instantaneous force-length relation of papillary muscle. In J. Baan, A. Noordergraaf, and J. Raines, editors, *Cardiovascular System Dynamics*, pages 99–105, 1978.

[38] J.C. Simo and D.D. Fox. On a stress resultant geometrically exact shell model, Part I: formulation and optimal parametrization. *Comput. Meths. Appl. Mech. Engrg.*, 72:267–304, 1989.

[39] J.C. Simo, D.D. Fox, and M.S. Rifai. On a stress resultant geometrically exact shell model, Part II: the linear theory; computational aspects. *Comput. Meths. Appl. Mech. Engrg.*, 73:53–92, 1989.

[40] J.C. Simo, D.D. Fox, and M.S. Rifai. On a stress resultant geometrically exact shell model, Part III: computational aspects of the nonlinear theory. *Comput. Meths. Appl. Mech. Engrg.*, 79:21–70, 1989.

[41] A. Veneziani. Boundary conditions for blood flow problems. In R. Rannacher, editor, *Proc. ENUMATH97, Heidelberg*, pages 596–607, 1998.

[42] A. Veneziani. *Mathematical and Numerical Modelling of Blood Flow Problems*. PhD thesis, University of Milan, 1998.

[43] A. Veneziani and C. Vergara. Defective flux boundary conditions for the Navier-Stokes problem. in preparation, 2003.

[44] A. Viedma, C. Jimenez-Ortiz, and V. Marco. Extended willis circle model to explain clinical observations in periorbital arterial flow. *J. Biomech.*, 30(3):265–272, 1997.

[45] N. Westerhof, F. Bosman, C.D. Vries, and A. Noordergraaf. Analog studies of the human systemic arterial tree. *J. of Biomech.*, 2:121–143, 1969.

[46] J.R. Womersley. Method for the calculation of velocity, rate of flow and viscous drag in arteries when the pressure gradient is known. *J. of Physiol.*, 127:553–563, 1955.

[47] M. Zacek and E. Krause. Numerical simulation of rhe blood flow in the human cardiovascular system. *J. Biomech.*, 29(1):13–20, 1996.

[48] C.K. Zarins. Hemodynamics in atherogenesis. In W.S. Moore, editor, *Vascular Surgery. A Comprehensive Review*, pages 86–96. W.B. Saunders, Philadelphia, PA., 1991.

[49] P. Zunino. *Mathematical and numerical modeling of mass tranfer in the Vascular System*. PhD thesis, Ecole Polytechnique Federeale Lausanne, 2002.